UNIVERSIDADE D
COIMBRA

António Francisco Brigas Caramelo

HIGH-GRANULARITY TIMING DETECTOR'S PATCH PANEL FILTER TESTING

Dissertação no âmbito do Mestrado em Engenharia Física orientada pelo Professor Doutor Ricardo Gonçalo e pelo Professor Doutor Pedro Assis e apresentada ao Departamento de Física da Faculdade de Ciências e Tecnologia da Universidade de Coimbra.

Setembro de 2023

UNIVERSIDADE D
COIMBRA

High-Granularity Timing Detector's Patch Panel Filter Testing

Supervisor:

Prof. Doutor Ricardo Gonçalo

Prof. Doutor Pedro Assis

Jury:

Prof. Doutor António Castanhola

Prof. Doutor Francisco Neves

Prof. Doutor João Guimarães da Costa

Prof. Doutor Pedro Assis

Doutor Stefan Guindon

Dissertation submitted in partial fulfillment for the degree of Master of Science in Engineering Physics.

Coimbra, October 2023

Agradecimentos

Este trabalho não seria possível sem os meus orientadores, Prof. Doutor Ricardo Gonçalo e Prof. Doutor Pedro Assis que me deram sempre autonomia e liberdade ao longo da tese garantindo sempre que todas as condições necessárias à sua conclusão estavam reunidas.

Agradeço à equipa do HGTD e à equipa do LIP por me terem acolhido e ajudado no que precisava, ao Eng. Orlando Cunha que durante um tempo sabia que sempre que ouvisse bater à porta eu estaria do outro lado, e à Elisabete Neves que ainda hoje me pergunta se tenho de ir ao CERN outra vez.

Se a Elisabete não teve de me marcar mais uma viagem foi graças ao Eng. Filipe Martins que sem qualquer obrigação me explicou como funcionava a fonte de alta tensão, e claro graças ao Eng. Afonso Soares Ferreira que garantiu sempre que não me faltava nada, que tinha o que precisava para fazer os testes e que ainda discutia ideias comigo, apoiando e interessando-se no meu trabalho. Agradeço-lhes também o facto de não ter tido de almoçar sempre sozinho, a cantina no CERN não era má mas uma refeição sabe sempre melhor quando é partilhada.

E se a cantina em Portugal não era pior seria porque tinha sempre companhia. Um obrigado ao grupo usual do polo 1, em especial ao Jorge Silva, meu amigo e colega de gabinete, que para além de me ouvir queixar durante o almoço ainda me ouvia durante o dia. A verdade é que estas queixas eram partilhadas, a ajuda mútua mas desigual, tenho a certeza que nunca te resolvi um problema. Devíamos ter comprado a X-Box.

Tenho a sorte de ter imensos amigos e eles o azar de terem um amigo sem a paciência de os mencionar um a um. Mas vocês sabem quem são. Aos amigos que fiz na universidade e aos que ficaram do secundário, obrigado. Uma personagem de uma grande obra literária disse "I wish there was a way to know you're in the good old days before you've actually left them.", não me relaciono, com vocês sempre soube que estava a fazer memórias.

Se tenho a sorte de estar aqui sentado a escrever e a agradecer às pessoas a que estou a agradecer no contexto em que estou, é graças às pessoas que, ao contrário do meus amigos, não tiveram escolha em terem de me aturar: o meu pai e a minha mãe. Obrigado por tudo, o que sou o devo a vocês.

Resumo

O HGTD é um novo detetor que faz parte do plano de modernização do LHC. O HGTD inclui sensores baseados na tecnologia LGAD, que requerem polarização de alta tensão e filtragem da tensão contínua através de unidades de filtro passa-baixo. O principal objetivo deste trabalho é testar e caraterizar estas unidades de filtragem e estabelecer um plano de testes.

Foram realizados vários testes, envolvendo eletrónica de suporte, injeção de sinal e medições com osciloscópio. Os testes abrangeram parâmetros como a função de transferência, a frequência de corte, a blindagem, os efeitos da componente DC, o ripple, o cross-talk, o ruído de modo comum e as correntes de fuga. Inesperadamente, foi observada uma fraca atenuação a frequências mais elevadas.

Para investigar estas anomalias, foi desenvolvido um esquema de teste mais pormenorizado. A causa foi atribuída ao equipamento de medição utilizado. A análise de cross-talk revelou a propagação do sinal para além dos canais designados, mas as simulações sugeriram que isto poderia não constituir um problema final. A corrente de fuga, um parâmetro crítico, atingiu valores aceitáveis (30 nA) após a limpeza e o revestimento da placa.

Em conclusão, a placa de filtragem tem um desempenho adequado, embora não impecável como inicialmente esperado. No entanto, também não é tão mau como os resultados dos testes iniciais poderiam ter sugerido.

Abstract

The HGTD, is a new detector part of the LHC upgrade plan. The HGTD comprises sensors based on LGAD technology, requiring high-voltage polarization and DC voltage filtering through low-pass filter units. The primary objective of this work is to test and characterize these filter units and establish a testing framework.

Several tests were conducted, involving support electronics, signal injection, and oscilloscope measurements. The testing pipeline covered parameters like transfer function, cutoff frequency, shielding, DC component effects, ripple, cross-talk, common mode noise, and leakage currents. Unexpectedly, poor attenuation at higher frequencies were observed.

To investigate these anomalies, a more detailed testing schematic was developed. The cause was traced back to the measuring equipment used. Cross-talk analysis revealed signal propagation beyond designated channels, but simulations suggested this might not pose a final issue. Leakage current, a critical parameter, reached acceptable values (30 nA) after board cleaning and coating.

In conclusion, the filter board performs adequately, though not flawlessly as initially expected. However, it is also not as poor as initial test results might have initially suggested

"Remember that all models are wrong; the practical question is how wrong do they have to be to not be useful."

George Box

Contents

Agradecimentos **v**

Resumo **vii**

Abstract **ix**

List of Acronyms **xv**

List of Figures **xvii**

List of Tables **xxiii**

1 Introduction **1**

1.1 Motivation 1

1.2 Large Hadron Collider (LHC) 2

1.3 HL-LHC 3

1.4 ATLAS 4

1.4.1 ATLAS coordinate system 5

1.4.2 Inner Detector 5

1.4.3 Calorimeters 6

1.4.4 Muon Spectrometer 9

1.4.5 Magnets 10

1.5 ATLAS upgrades for HL-LHC | ITk 12

1.6 ITk limitations and HGTD motivations 13

1.7 HGTD 15

1.8 LGAD Sensor 18

1.9 High Voltage (HV) System 19

2 Patch Panel Filters **21**

2.1 Design . . . 23

2.2 Grounding . . . 23

2.3 Requirements . . . 25

2.4 Filter Board Background . . . 26

3 Experimental Work **29**

3.1 Component Values . . . 29

3.2 Tranfer Curve . . . 31

3.2.1 Experimental Setup . . . 32

3.2.2 Deviation from theory . . . 33

3.3 Cutoff Frequency . . . 40

3.4 Shielding effect . . . 42

3.5 High Voltage Transfer Curve . . . 44

3.6 Ripple attenuation measurement . . . 50

3.7 Cross Talk and higher frequency transfer curves . . . 54

3.8 Common mode (CM) noise . . . 56

3.9 Leakage Current . . . 57

3.10 Explanatory Model . . . 58

3.11 Established model aplied to final environment . . . 69

4 Discussion and Conclusions **75**

4.1 Discussion . . . 75

4.2 Limitations . . . 76

4.3 Implications . . . 77

4.4 Future Work . . . 77

Bibliography **79**

A Appendix **83**

A.1 Transfer Curve 1 . . . 83

A.2 Transfer Curve 2 . . . 85

A.3 Low Voltage Transfer Curve for All Channels . . . 86

A.4 Ripple Attenuation . . . 86

B Appendix **89**

List of Acronyms

LHC	Large Hadron Collider
CERN	Conseil Européen pour la Recherche Nucléaire
ATLAS	A Toroidal LHC ApparatuS
CMS	Compact Muon Solenoid
ALICE	A Large Ion Collider Experiment
LHCb	Large Hadron Collider beauty
HL-LHC	High Luminosity LHC
IP	Interaction Point
ID	Inner Detector
IBL	Insertable B-Layer
SCT	SemiConductor Tracker
TRT	Transition Radiation Tracker
LAr	Liquid Argon
ECAL	Electromagnetic Calorimeter
HCAL	Hadronic Calorimeter
TileCal	Tile Calorimeter
HEC	Liquid Argon End-Cap
FCAL	Forward Calorimeter
MS	Muon Spectrometer

MDT	Monitored Drift Tubes
CSC	Cathode Strip Chambers
RPC	Resistive Plate Chambers
TGC	Thin Gap Chambers
ITk	Inner Tracker
HGTD	High-Granularity Timing Detector
ASIC	Application-Specific Integrated Circuit
ALTIROC	ATLAS LGAD Time Read Out Chip
LGAD	Low Gain Avalanche Detector
PEB	Peripheral Electronics Board
HV	High Voltage
CM	Common Mode
AWG	Arbitrary Waveform Generator
DC	Direct Current

List of Figures

1.1 Schematic of the Large Hadron Collider (LHC) complex [1] 3

1.2 Cut-away view of the A Toroidal LHC ApparatuS (ATLAS) detector [2] 5

1.3 Cut-away view of the ATLAS inner detector.[2] 7

1.4 Cut-away view of the ATLAS calorimeter system[2] 7

1.5 TileCal schematic [2] 9

1.6 The three Forward Calorimeter (FCAL) modules sit within the support tube, a structural member of the cryostat [3] 10

1.7 Cut-away drawing of one EndCap Cryostat with the interaction point off to the lower left. The calorimeters in this cryostat are the endcap calorimeters (the Electromagnetic Calorimeter (ECAL) end-cap and Liquid Argon End-Cap (HEC)), and the FCAL. [3] 10

1.8 Cut-away view of the ATLAS muon system[2] 11

1.9 Schematic of the ATLAS magnet system. The eight barrel toroid coils, with the end-cap coils interleaved are visible. The solenoid winding lies inside the calorimeter volume.[2] 11

1.10 The barrel and end-cap Strip Detector elements are represented in blue, while the Pixel Detector sensors are depicted in red for the barrel layers and dark red for the end-cap rings. For clarity, only one quadrant and active detector elements are illustrated in the diagram. The horizontal axis corresponds to the beam line axis, with the interaction point marked as zero. The vertical axis indicates the radius measured from the interaction region. The outer radius is determined by the inner radius of the barrel cryostat, which houses the solenoid and the electromagnetic calorimeter[4] 13

1.11 Local pileup vertex densities at generator level for $\langle\mu\rangle = 30$ (blue dashed line) and $\langle\mu\rangle = 200$ (red line). [5] 14

1.12 Resolution of the longitudinal track impact parameter, z0, as a function of η for muons of pT = 1 GeV and pT = 10 GeV using Inner Tracker (ITk) alone.[5] . . . 14

1.13 Visualisation of the truth interactions in a single bunch crossing in the z–t plane, showing the simulated Hard Scatter (HS) $t\bar{t}$ event interaction (red) with pileup interactions superimposed (black) for $\langle\mu\rangle = 200$.[5] 15

1.14 Position of the two High-Granularity Timing Detector (HGTD) disks within the ATLAS Detector [5] 16

1.15 An overview of the High Granularity Timing Detector (HGTD) to be installed on each of the two end-cap calorimeters. Various components of the HGTD are depicted: the hermetic vessel (consisting of front and rear covers, as well as an outer ring), the two double-sided layers that are instrumented and mounted on two cooling disks with sensors on the front and back of each cooling disk, and the two neutron moderator pieces that are positioned inside and outside the hermetic vessel. [5] 17

1.16 Overlap between the modules on the front and back of the cooling disk. There is a sensor overlap of 20% for r > 470 mm, 54% for 230 mm < r < 470 mm and 70% for r < 230 mm.[5] 17

1.17 Cross section schematic of an Low Gain Avalanche Detector (LGAD) sensor[5] . 19

2.1 The preliminary design of the HGTD patch panels (PP-EC) located on the end-cap calorimeter surface. The PP-EC components have been placed in various locations around the end-cap surface of the calorimeter, as indicated by arrows.[5] 22

2.2 The HGTD HV layout. The High Voltage (HV) units are in the service cavern (USA15) protected from radiation while de HV-PP are in the PP-EC area closer to the detector with a shorter connection to the PEB's via 15 m shielded Type II cables.[6] 22

2.3 Total area of a ground loop greatly reduced by a grounded cable shield[7] 24

2.4 Schematic of the current Grounding and Shielding Solution of the HV supply system [8] 24

2.5 Grounding schematic of the HGTD modules[9] 25

2.6 Filter module containing two filter boards and connectors. [9] 26

2.7 Individual filter board with 14 2nd order low-pass filters [9] 26

2.8 The diagram illustrates the components comprising the 2nd-order filter, including resistances R1 and R2, capacitors C1 and C2. Additionally, decoupling capacitors C3 and C4 are included to serve as effective noise filters for Common Mode (CM) noise 27

3.1 Schematic for simulating common mode noise, depicting only the filter without any decoupling capacitors for common mode noise attenuation 30

3.2 Schematic for simulating common mode noise, depicting only the filter and decoupling capacitors for common mode noise attenuation 30

3.3 Bode plot of the filter's frequency response to common mode noise 31

3.4 Transfer curve measuring setup using PicoScope. 32

3.5 Schematic depicting program's pseudocode, illustrating its fundamental operational principles. 33

3.6 Transfer function of the filter board's first channel as determined through measurements employing a PicoScope. 34

3.7 Transfer function of the filter board's first channel as determined through measurements employing a PicoScope compared to initial theory 35

3.8 Circuit schematic simulation utilized to discern whether the reduction in amplitude observed across varying frequencies is attributable to a malfunction in the Arbitrary Waveform Generator (AWG)) or is influenced by the component values associated with the measuring instruments. 36

3.9 Experimental outcomes obtained from the aforementioned schematic juxtaposed with the simulation results of the same schematic, considering two distinct output resistances 37

3.10 Schematic for measuring the transfer curve with integrated models for probes and PicoScope. 37

3.11 Transfer function of the filter board's first channel as determined through measurements employing a PicoScope compared with the initial theoretical prediction and the simulated schematic illustrated in Figure 3.10 38

3.12 Filter schematic representation that incorporates the output resistance of the AWG (R3) and the decoupling capacitor (C3) for the filter. 39

3.13 Transfer function of the filter board's first channel as determined through measurements employing a PicoScope compared with the initial theoretical prediction and the simulated schematic illustrated in Figure 3.12 39

3.14 Schematic depicting program's pseudocode, illustrating its fundamental operational principles. 41
3.15 Histogram of the results of measuring 100 cutoff frequencies for channel 1 41
3.16 Histograms of the measurements obtained for 100 cutoff frequencies are depicted for channel 1, channel 2, and channel 3, presented in a stacked format. 42
3.17 Shielded filter board 43
3.18 Transfer characteristics of filters 3, 5, and 7 compared between configurations with the filter board unshielded and with the filter board shielded 43
3.19 Schematic of the experimental setup used to investigate and obtain the transfer function of the filter under high Direct Current (DC) voltage conditions 45
3.20 Setup used to make the high voltage measurements 46
3.21 Results of transfer curve measurements conducted using the schematic depicted in Figure 3.19, with comparisons made between plots for various voltage levels and the simulation results obtained from the previously mentioned schematic. . . 46
3.22 Outcomes of the transfer curve measurements carried out at different voltage levels utilizing the schematic illustrated in Figure 3.19, employing the Keythley 2410 High Voltage Power Supply for the experiments. 47
3.23 Transfer curves obtained with different Power Supplies compared at different voltage levels 48
3.24 Transfer curves obtained at different voltage levels using the Keythley 2410 High Voltage Power Supply grounded 48
3.25 Transfer Function at different voltage levels using a different channel 49
3.26 Transfer Function at different voltage levels using an older board with no decoupling capacitors 49
3.27 Transfer curves obtained at different voltage levels using the High Voltage Power Supply, osciloscope and function generator 49
3.28 Transfer curves obtained through simulation using the schematic depicted in Figure 3.19 with the original capacitor values compared to those with the capacitor values reduced by 15%. 50
3.29 Schematics representing the ripple measuring process without filter (a) and with filter (b) 51
3.30 Plots depicting the waveform of the high voltage power supply channel 1, measured both with (a) and without (b) the filter. 52

3.31 FFT depiction of the waveforms from Figure 3.30, centered around the ripple frequency range. Figure (a) illustrates the scenario without the filter, while Figure (b) depicts the situation with the filter. 52

3.32 FFT representation of the waveforms from Figure 3.30, covering the entire measurable frequency range. Figure (a) illustrates the scenario without the filter, while Figure (b) depicts the situation with the filter. 53

3.33 Transfer function determined by introducing a signal into channel 1 and monitoring the output from channel 14. It should be noted that for frequencies below a certain threshold (30 kHz), the signal amplitude was insufficient for reliable detection. 55

3.34 Transfer function of channel 1 in the filter manually measured employing an oscilloscope and function generator for both low voltage (a) and high voltage (b) scenarios. Measurements extended up to higher frequencies, approximately 50 MHz. 56

3.35 Common mode noise transfer function manually measured employing an oscilloscope and function generator for various voltage levels. Measurements extended up to 50 MHz. 57

3.36 Capacitor parasitic model[10] 59

3.37 Results obtained using a setup similar to the one depicted in the schematic from Figure 3.8, utilizing diffent probes, oscilloscope [11], and function generators [12]. 61

3.38 Comparison of transfer curves for a filter channel when probes and ground wires are either looped or straight. 62

3.39 Transfer curve measuring setup used for straight (a) and looped (b) probe results comparison 62

3.40 Full parasitic model of the low voltage transfer curve measuring schematic 63

3.41 Full parasitic model of the common mode noise transfer curve measuring schematic 64

3.42 Full parasitic model of the high voltage transfer curve measuring schematic . . . 65

3.43 Model simulation results for the different scenarios 66

3.44 Model prediction of values presented in figure 3.37 67

3.45 Full parasitic model of the ripple attenuation measuring schematic 68

3.46 Model prediction of ripple attenuation, closely resembles the one measured (20 dB) 69

3.47 Full parasitic model of final envinronment 70

3.48 Simulation of the transfer curve for the model in the final environment compared to the ideal theoretical curve. In this simulation, the values of Lgnd and Rgnd were set at 10 $m\Omega$ and 50 nH, respectively. 71
3.49 Simulation of the transfer curve for the model in the final environment comparing the effect of grounding inductance (a) and grounding resistance (b) 72
3.51 Simulation of the transfer curve of an adjacent channel for the model in the final environment with the PS grounded. In this simulation, the values of Lgnd and Rgnd remain at 10 $m\Omega$ and 50 nH, respectively. 72
3.50 Simulation of the transfer curve for the model in the final environment compared to the ideal theoretical curve with the PS grounded. In this simulation, the values of Lgnd and Rgnd were set at 10 $m\Omega$ and 50 nH, respectively. 73

A.1 Filter schematic 83
A.2 Filter schematic 85
A.3 Transfer function of the filter board's channels as determined through measurements employing a PicoScope 86

List of Tables

3.1 A table providing a summary of the outcomes derived from measuring the HV power supply output waveform both with and without the filter, displaying the attenuation levels. Please note that this table is a partial representation, as a total of two modules, each comprising 14 channels, were subjected to testing. . . 54

3.2 Leakage current measurements conducted for all the channels on the filter board, both at 500V and 900V. 58

3.3 Table providing a summary of the values of parasitic components employed in the model 66

A.1 Full table of the outcomes derived from measuring the HV power supply output waveform both with and without the filter, displaying the attenuation levels. . . 87

1 Introduction

1.1 Motivation

The LHC is scheduled for an upgrade referred to as High Luminosity LHC (HL-LHC). The primary objective of the HL-LHC is to attain an instantaneous luminosity approximately seven times greater than the originally designed luminosity of the LHC. This increase in luminosity at the HL-LHC will lead to a higher number of proton-proton (p-p) collisions occurring simultaneously. Consequently, this will result in a higher density of particle tracks, posing challenges in the reconstruction of significant events.

To address the elevated luminosity requirements of the HL-LHC and the consequent increase in particle collisions, the ATLAS experiment has devised a series of detector upgrades. As a solution to contend with the pileup issue, the HGTD is proposed. The HGTD will serve the purpose of measuring the times of minimum-ionizing particles with a time resolution of approximately 30 ps per track during the initial phase of the HL-LHC operation.

The HGTD is composed of sensors based on LGAD technology, which necessitates polarization through the application of high voltage. This high voltage direct current is filtered using low-pass filter units.

The main goal of this thesis is the testing and characterization of these units, along with the creation of the testing framework.

The structure of this thesis deviates from conventional organization due to the nature of the research. Rather than presenting all test methods, results, and discussion separately, this work presents them cohesively for each individual test.

This document is divided into four chapters. In the first chapter, a comprehensive overview of the ATLAS experiment is provided, alongside the delineation of the LHC upgrade plans and an introduction to the HGTD. The second chapter delves deeper into the patch panel filters, which constitute the focal point of investigation in this thesis. All the details about the experiments, including the methods used and the results obtained, can be found in the "Experimental Work" chapter. Finally, in the "Discussion and Conclusions" chapter, the findings

and overall conclusions are presented.

1.2 Large Hadron Collider (LHC)

The LHC [13] is currently the most powerful particle accelerator in the world, it was designed to investigate the fundamental aspects of particle physics. Located beneath the France-Switzerland border, the LHC is part of the Conseil Européen pour la Recherche Nucléaire (CERN) and operates as a circular collider with two particle beams accelarating in oposite directions. This circular design allows particles to keep accelarating within the bounds of a maximum achievable velocity, gaining energy and increasing the likelihood of collisions.

Before the particles reach the LHC ring they go through the LHC complex (fig.1.1) that consists of a series of machines that progressively boost particles to higher energies. Each machine raises the energy of a particle beam before injecting it into the next. The LHC, which became operational in September 2008, serves as the final element in this chain, guiding the beams in the accelarator ring with a very strong magnetic field maintained by superconducting eletromagnets.

The particles beams are then directed to collide at various locations along the accelarator ring, as depicted in fig. 1.1. These specific collision points correspond to different primary detectors at CERN: ATLAS [2], Compact Muon Solenoid (CMS) [14], A Large Ion Collider Experiment (ALICE) and the Large Hadron Collider beauty (LHCb) experiments [15] . ATLAS and CMS are considered general-purpose experiments that mostly study proton-proton collisions. Regarding the LHCb while it also records data from these type of collisions, its principal objective is to study beauty particles. The ALICE experiment's primary aim is to study heavy ion collisions.

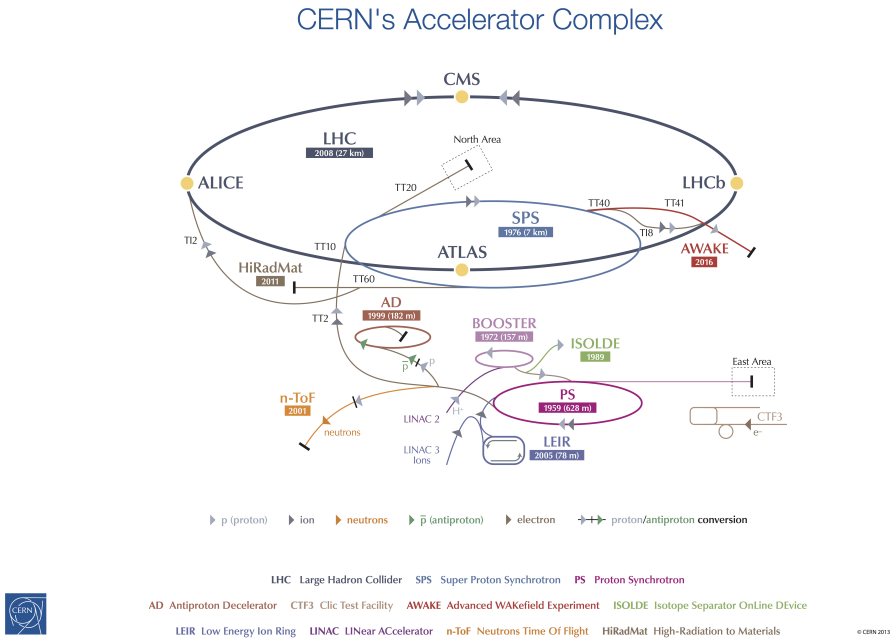

Figure 1.1: Schematic of the LHC complex [1]

1.3 HL-LHC

The particle beam(s) traveling through the LHC is sorted in discrete groups of protons, each having identical energy and referred to as bunches. Within the LHC there are 2808 evenly spaced bunches, with approximately 10^{11} protons in each bunch, all traveling at nearly the speed of light. These bunches are separated from one another by a time interval of 25 ns, resulting in a collision frequency of 40 MHz, also known as the bunch crossing frequency.

The particle interactions within a bunch collision are called events. The rate of an event per collision, dN/dt, is proportional to instantaneous luminosity $\mathcal{L}$ and the cross section of said event, σ_i:

$$\mathcal{L}[cm^{-2}s^{-1}] = \frac{1}{\sigma_i}\frac{dN}{dt} \tag{1.1}$$

To increase the likelihood of observing a rare process or to improve the statistical significance of a measurement for an already discovered process, it is necessary to maximize the number of events. Equation number 1.1 shows that an increase in luminosity would augment the probability of an event, so luminosity can be used as a quantifier of particle accelarator performance. The instantaneous luminosity is given by:

$$\mathcal{L} = f_{coll}\frac{n_1 n_2}{r\pi\sigma_x\sigma_y} \tag{1.2}$$

where f_{coll} is the collision frquency, n_1 and n_2 are the number of particles in each bunch and σ_x and σ_y are parameters that describe the transverse beam size in the horizontal and vertical directions, respectively.

Integrated luminosity, $\mathcal{L}_{int}$, is a term often used to describe the cumulative amount of data that has been delivered or collected during a specific period of operation.

$$\mathcal{L}_{int} = \int \mathcal{L}(t)dt \tag{1.3}$$

Statistically the error for the observation of a specific particle process depends on the number of particles N:

$$\delta \propto \frac{1}{\sqrt{N}} \tag{1.4}$$

This means that the statistical error halves when the sample size quadruples.

In conclusion, the integrated luminosity is one of the main parameters that significantly influence the discovery potential of an accelerator. The two main ways of increasing integrated luminosity are to increase the instantaneous luminosity and to increase the run time.

For this reason, the LHC is planned to undergo an upgrade known as HL-LHC. The HL-LHC aims to achieve an instantaneous luminosity approximately 7 times larger than the original design luminosity of the LHC. The primary objectives of the HL-LHC include reaching a peak luminosity of $7.5 \times 10^{34}\ cm^{-2}s^{-1}$, compared to the $2.1 \times 10^{34}\ cm^{-2}s^{-1}$ achieved during Run 2 of the LHC, and an integrated luminosity of 250 fb^{-1} annually. Over its entire operational lifetime, the HL-LHC is targeting to accumulate up to 4000 fb^{-1} of integrated luminosity. This value is nearly ten times greater than the total luminosity achieved by the LHC during its initial twelve years of operation.

1.4 ATLAS

As previously mentioned the ATLAS experiment is one of the multi-purpose detectors of the LHC. It is positioned around 100 meters underground and it is designed with a cylindrical and multi-layered structure. It has 25 meters in height (diameter) and 44 meters in length, with a total weight of approximately 7000 tonnes. The main objective of the ATLAS experiment is to record and track the decay products of particles resulting from the proton-proton collisions at one of the LHC's Interaction Point (IP). The debris of elementary particles generated during the collisions rapidly decay but can be reconstructed based on their decay products.

Particles can be indentified acording to their energy, momentum and charge. To get this

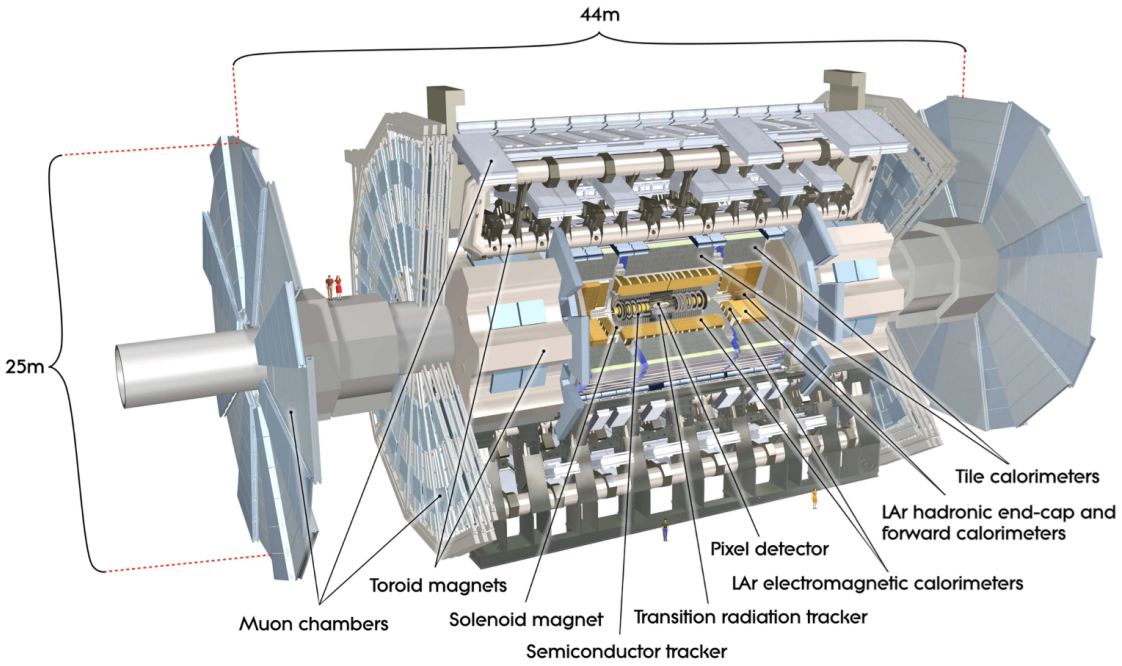

Figure 1.2: Cut-away view of the ATLAS detector [2]

information, a magnetic field is utilized to bend the trajectories of charged particles. The charge is determined from the bending direction, while the momentum is reconstructed from the curvature radius. The energy of the particles is measured as they come to stop within the detector.

1.4.1 ATLAS coordinate system

The detector follows a common right-handed coordinate system, with its origin located at the IP at the center of the detector. The z-axis aligns with the beam line, whereas the x-axis points towards the center of the LHC ring, and the y-axis points upwards. The azimuthal angle, ϕ, is measured around the beam axis, and the polar angle, θ, represents the angle from the beam axis. The pseudorapidity, η, is defined in terms of the polar angle as

$$|\eta| = -ln(tan(\frac{\theta}{2})) \tag{1.5}$$

So the plane at the interaction point perpendicular to the beam has $\eta = 0$ and the beam direction has $\eta = \infty$.

1.4.2 Inner Detector

The ATLAS experiment comprises several subdetector systems, each serving a specific purpose and covering distinct pseudorapidity ranges. Starting from the innermost layer, we have the

Inner Detector (ID).

The ID covers the pseudorapidity range of $|\eta| = 2.5$. As it is the innermost detector of the ATLAS experiment, it is the first subsystem to detect the decay products from the proton-proton collisions. Its main function is to measure the trajectories of charged particles originating from the IP. With the tracking information from these trajectories, the vertex from which each particle originates can be determined.

The detector combines high-resolution detectors at the inner radii with continuous tracking elements at the outer radii, all contained in a solenoidal magnet with a central field of 2T parallel to the beam axis that as mentioned already bends the trajectory of particles giving us information about charge and particle momentum.

The ID is contained within a cylinder with a length of 7 meters and a radius of 1.15 meters. Its layout is shown in Figure 1.3 and consists of three sub-detectors: the Pixel Detector, which includes the Insertable B-Layer (IBL) [16], the SemiConductor Tracker (SCT) [17], and the Transition Radiation Tracker (TRT) [18].

The Pixel and SCT detectors being the innermost part of the ID are, like mentioned above, high-resolution detectors offering precise track measurements at inner radii. The TRT being on the outer radius of the ID provides measurements at larger radii improving the momentum quantification of particles.

As part of the ID, the Pixel and SCT detectors serve as the innermost systems and, as previously mentioned, are the high-resolution detectors that offer precise track measurements at inner radii. On the other hand, the TRT detector is positioned at the outer radius of the ID. It provides measurements at larger radii, enhancing the momentum quantification of particles by offering continuous tracking information.

1.4.3 Calorimeters

The Inner Detector is responsible for measuring the charge and momentum of particles, but to determine their energy, additional detectors called calorimeters are used. Calorimeters are designed to measure the energy lost by a particle as it passes through the detector elements. These calorimeters are designed to absorb most of the energy of particles generated from collisions, stopping them within the volume of the calorimeter. Calorimeters can stop known particles, with the exception of muons and neutrinos.

The ATLAS calorimeter system consists of three calorimeter sub-detectors: the Electromagnetic, the Hadronic, and the Forward Calorimeter. The whole calorimeter system (fig. 1.4) has full ϕ coverage arround the beam axis and covers a pseurapidity region $|\eta| < 4.9$

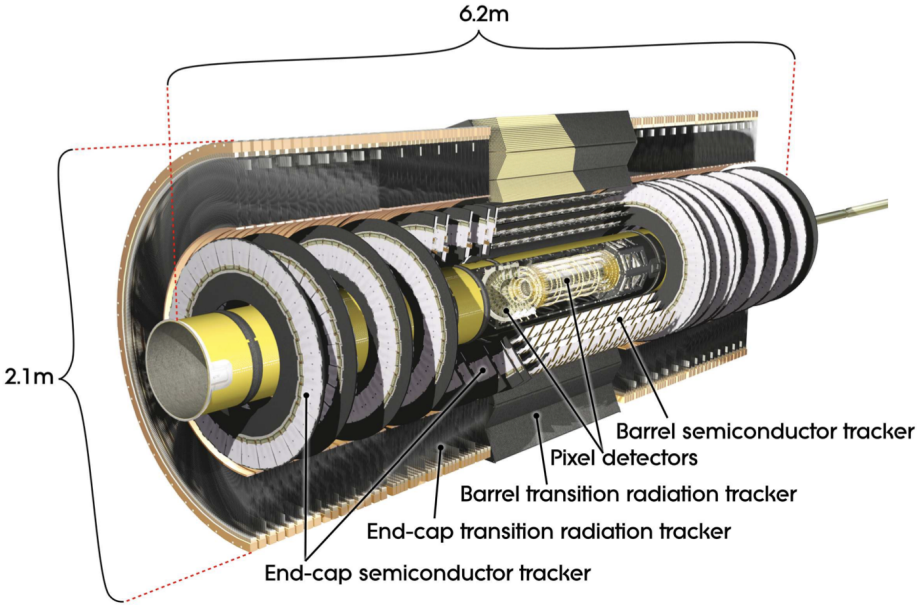

Figure 1.3: Cut-away view of the ATLAS inner detector.[2]

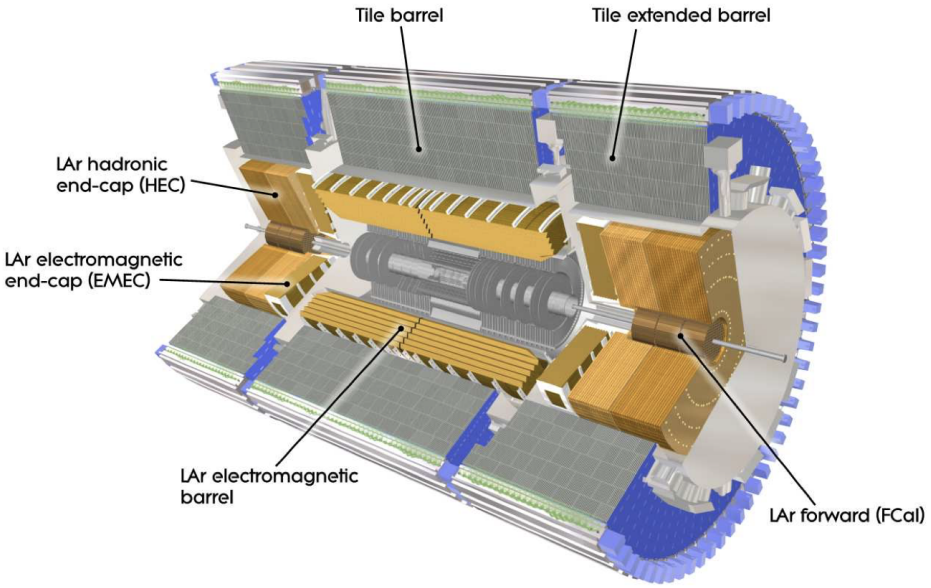

Figure 1.4: Cut-away view of the ATLAS calorimeter system[2]

Electromagnetic Calorimeter

The Liquid Argon (LAr) ECAL [19] is designed to stop particles entirely, ensuring that they deposit all their energy within the detector. It measures the energy of electrons, positrons, and photons.

The ECAL has an accordion-like structure with alternating layers of showering material (passive lead absorvers) and active material. The ECAL utilizes high-Z materials like LAr as active material.

When these particles interact with the lead layers, they induce the production of an electromagnetic shower, and the energy of the shower is measured in the liquid argon layers. When a particle crosses the LAr, ionization electrons create an output signal proportional to its energy.

The ECAL is subdivided into a barrel and two end-caps. The barrel calorimeter is embedded in a barrel cryostat, which surrounds the ID and hosts the solenoid magnet. Two end-caps cryostats house the end-cap electromagnetic calorimeter as well as the end-caps hadronic calorimeter. The barrel covers the pseudorapidity range $|\eta| < 1.475$ and the endcaps calorimeter cover the $1.375 < |\eta| < 3.2$ range.

Hadronic Calorimeter

Surrounding the ECAL, the Hadronic Calorimeter (HCAL) acts as its counterpart, it measures the energy of particles that escape the ECAL, with the exception of muons and neutrinos.

The HCAL is made up of a barrel part and two end-cap calorimeters that cover the $1.5 < |\eta| < 3.2$ range.

The barrel part of the hadronic calorimeter corresponds to the Tile Calorimeter (TileCal) [20] and serves as a sampling calorimeter. It is thicker than the electromagnetic calorimeter to effectively handle longer and wider hadronic showers, as compared to electromagnetic showers. The barrels are constructed with steel absorbers and scintillator tiles made of polystyrene as the active material. When an ionizing particle hits the steel layer it creates a shower that leads to photons being produced in the scintillator. The scintillation light is then converted into an electric current proportional to the original particle's energy.

The endcap calorimeters in the forward region of the HCAL correspond to the HEC calorimeter. LAr is the chosen active material for the detectors in this high radiation region as it possesses radiation-hard properties. The materials chosen for the passive material in this region are copper and tungsten. The HEC calorimeter shares the two end-cap cryostats with the ECAL end-caps and the FCAL.

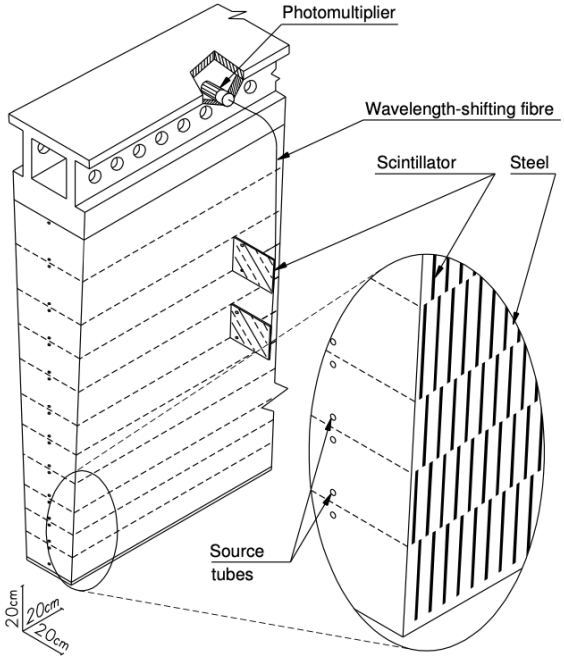

Figure 1.5: TileCal schematic [2]

Forward Calorimeter

The FCAL [3] consists of an electromagnetic calorimeter and two hadronic calorimeters positioned in the pseudorapidity range $3.1 < |\eta| < 4.9$, strategically chosen to maximize detector acceptance at low radii. As they are located at high η, approximately 4.7m from the IP, they are subjected to a high particle flux.

Given their proximity to the Interaction Point and the exposure to a significant particle flux, the forward calorimeters require exceptional radiation hardness to maintain long-term stability and reliable performance.

Figures 1.6 and 1.7 display the FCAL and its division into modules, as well as its integration into the ATLAS experiment, alongside the other end cap calorimeters.

1.4.4 Muon Spectrometer

The Muon Spectrometer (MS) [21] is the outermost layer, surrounding the calorimeters, its function is to the detect muons that are particles that escape from calorimeters without interacting. The MS is a high-resolution spectrometer designed to detect these particles and measure their momentum in a pseudo rapidity range of $|\eta| = 2.7$. The MS system is comprised of four sub-detectors: Monitored Drift Tubes (MDT), Cathode Strip Chambers (CSC),Resistive Plate Chambers (RPC) and Thin Gap Chambers (TGC).

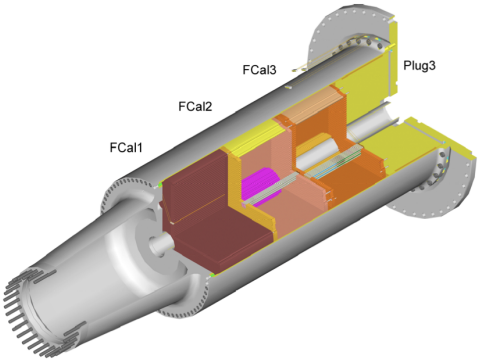

Figure 1.6: The three FCAL modules sit within the support tube, a structural member of the cryostat [3]

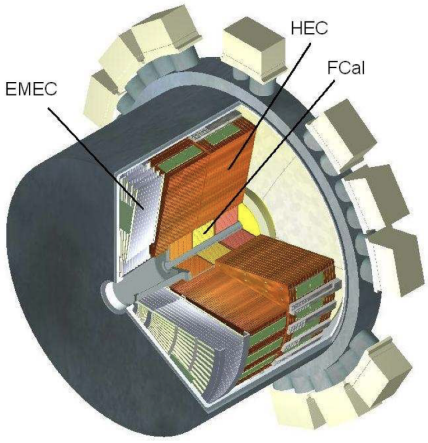

Figure 1.7: Cut-away drawing of one EndCap Cryostat with the interaction point off to the lower left. The calorimeters in this cryostat are the endcap calorimeters (the ECAL endcap and HEC), and the FCAL. [3]

The MDT and CSC are responsible for particle momentum measurements through the curvature of the muons trajectory that is bent due to the very strong toroid magnets. The MDT covers the $\eta < 2.7$ pseudo rapidity range, while at higher pseudo rapidities ranges ($2.0 < \eta < 2.7$) and closer to the IP CSC's are used. RPC's and TGC's are used as detectors capable of triggering on muon tracks to measure muons trajectories, both in the bending (η) and non-bending (θ) plane.

1.4.5 Magnets

As mentioned earlier, the ATLAS experiment utilizes magnetic fields to determine the momenta of particles generated in collisions. These fields are produced by the ATLAS magnet system comprised of four superconducting magnets.

The system consists of a central solenoid aligned with the beam, generating a 2 T magnetic field for the inner detector. Additionally, there are a barrel toroid and two end-cap toroids that create toroidal magnetic fields for the muon detectors in the central and end-cap regions. A schematic representation of the ATLAS magnet system can be found in Figure 1.9.

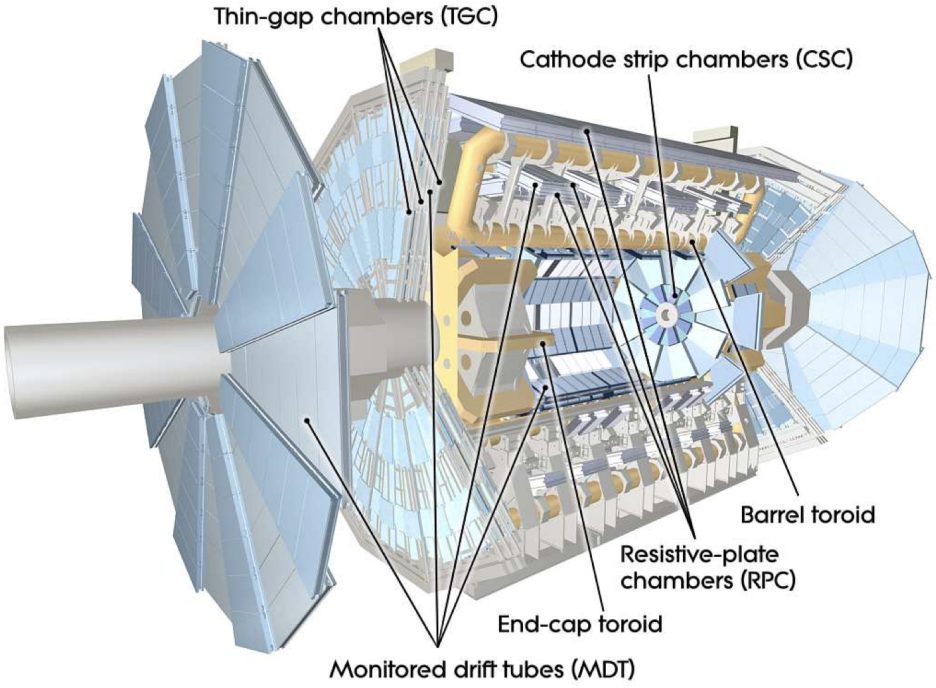

Figure 1.8: Cut-away view of the ATLAS muon system[2]

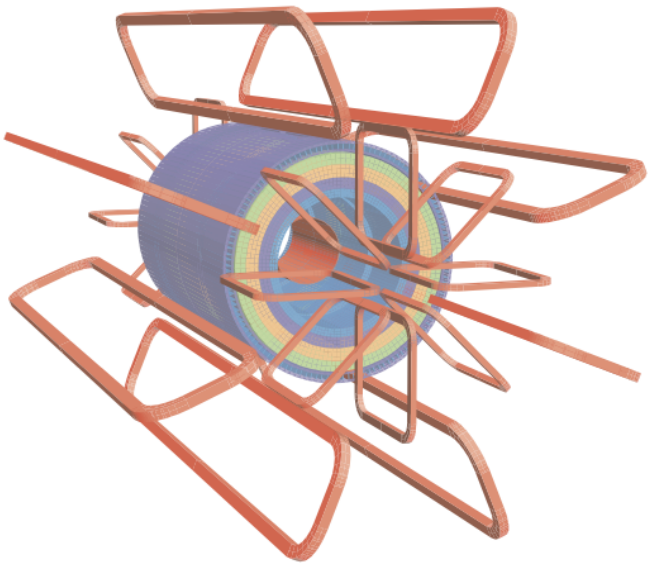

Figure 1.9: Schematic of the ATLAS magnet system. The eight barrel toroid coils, with the end-cap coils interleaved are visible. The solenoid winding lies inside the calorimeter volume.[2]

1.5 ATLAS upgrades for HL-LHC | ITk

The increase in luminosity of the HL-LHC will increase the amount of p-p collisions. These simultaneous collisions result in a higher density of particle tracks making it difficult to reconstruct significant events. The accumulation of simultaneous proton-proton collisions during the crossing of two proton bunches is called pileup. With the HL-LHC there is an expected average of 200 simultaneous pp interactions , $\langle\mu\rangle$.

In order to cope with the higher luminosity demands of the HL-LHC and the correspondingly higher pileup, the ATLAS experiment has a series of detector upgrades planned [22] namely the pixel and strip trackers, LAr and TileCal, the muon system and the data acquisition system.

The LAr calorimeter will have its front-end and back-end electronics replaced, as for the TileCal there will be a complete replacement of on-detector and off-detector electronics, the photomultipliers most exposed to radiation will also be replaced. The goal for the muon system upgrade is to minimize the triggers that arise from particles other than muons and to increase the geometrical coverage in the barrel. To do so new MDT and RPC detectors will be installed in the barrel region and new TGC detectors will be installed at the end-cap region

The ID was initially designed to operate for 10 years, handling an average pileup of 23. However, it is incapable of maintaining the required performance levels during the HL-LHC due to the increased pileup and luminosity demands. To address this issue, the ID will be replaced with a more radiation hard and finer granularity detector system known as the ITk[4]. The primary objective of the ITk is to achieve equal or superior performance compared to the current detector. One of the main goals is to maintain a high track reconstruction efficiency ($> 95\%$) while minimizing the occurrence of fake tracks.

The ITk is an all-silicon detector, comprising a strip system with 4 barrel layers and 6 end-cap disks per side. This strip detector covers the region with a pseudo-rapidity value of $|\eta| < 2.7$. Additionally, there is a pixel system covering the pseudo-rapidity region of $|\eta| < 4$, consisting of 5 barrel layers with inclined modules and rings. The schematic layout of the ITk can be seen in fig. 1.10.

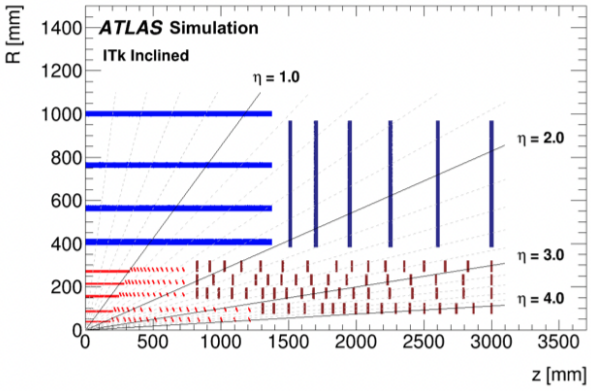

Figure 1.10: The barrel and end-cap Strip Detector elements are represented in blue, while the Pixel Detector sensors are depicted in red for the barrel layers and dark red for the end-cap rings. For clarity, only one quadrant and active detector elements are illustrated in the diagram. The horizontal axis corresponds to the beam line axis, with the interaction point marked as zero. The vertical axis indicates the radius measured from the interaction region. The outer radius is determined by the inner radius of the barrel cryostat, which houses the solenoid and the electromagnetic calorimeter[4]

1.6 ITk limitations and HGTD motivations

As already mentioned with the increase in luminosity of the HL-LHC the average number of interactions per bunch crossing (pileup) will rise significantly, from approximately 30 to around 200. Consequently, managing pileup will become one of the primary challenges to address during the HL-LHC operation.

A higher average number of interactions per bunch crossing leads to an increased spatial pileup line density, representing the number of collisions per length unit along the beam axis during one bunch crossing.

For comparison Figure 1.11 displays the pileup density distributions for $\langle\mu\rangle = 30$ and $\langle\mu\rangle = 200$. For $\langle\mu\rangle = 200$ an average pileup density of 1.8 vertices/mm is expected with the most probable local pileup density being is 1.44 vertices/mm.

To efficiently associate charged particles with their respective production vertices at such densities, the resolution of the longitudinal track impact parameter needs to be less than 600 μm. The ITk detector achieves this resolution in the central pseudorapidity region. However, in the forward region at $|\eta| \sim 4$, the the detector's resolution is insufficient.

The ITk determines the vertex of collisions using a track to vertex aproach where a track is associated to a vertex if the impact parameter z_0 is compatible with the vertex position, in figure 1.12 we can see the resolution track impact parameter, z_0, as a function of η for muons of

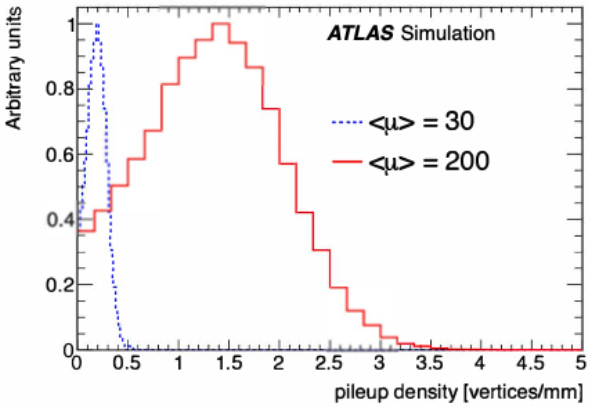

Figure 1.11: Local pileup vertex densities at generator level for $\langle\mu\rangle = 30$ (blue dashed line) and $\langle\mu\rangle = 200$ (red line). [5]

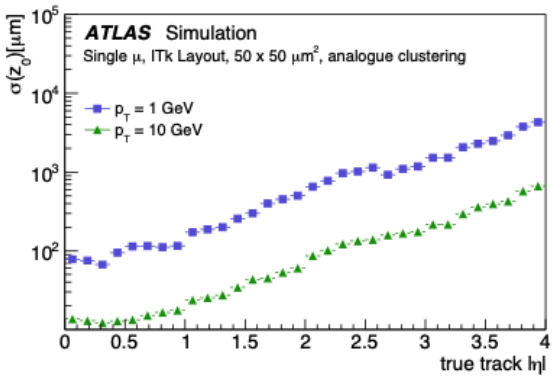

Figure 1.12: Resolution of the longitudinal track impact parameter, z0, as a function of η for muons of pT = 1 GeV and pT = 10 GeV using ITk alone.[5]

pT (Transverse Momentum) = 1 GeV using only the ITk.The results show that at $|\eta| = 3$, the z0 resolution for a 1 GeV track is approximately 1 mm.

However, with a most probable value of vertex density of 1.44 vertices/mm at $\langle\mu\rangle = 200$, a track with such a low pT becomes ambiguous at large pseudorapidity and high luminosity. Under such conditions, the track-to-vertex association using only spatial information will be significantly affected by pileup.

Figure 1.13 presents the time dispersion as a function of the true interaction z position from simulation, in a single bunch crossing. Having this into consideration we can improve the performance of the ITk vertex reconstruction by introducing precise time information. Precise time measurements can help distinguish the correct production vertex by considering only the tracks with a similar time consistent with the time of the hard-scattering vertex and in this way excluding tracks that do not orginate from it and resolving ambiguities for nearby vertices

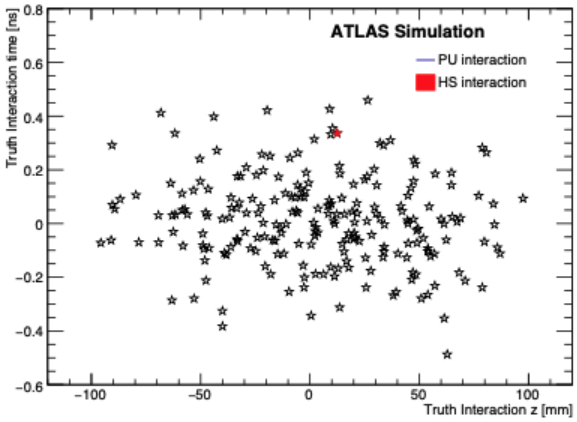

Figure 1.13: Visualisation of the truth interactions in a single bunch crossing in the z–t plane, showing the simulated Hard Scatter (HS) $t\bar{t}$ event interaction (red) with pileup interactions superimposed (black) for $\langle\mu\rangle = 200$.[5]

(provided the time separation is sufficient).

1.7 HGTD

As a solution to the pileup challenge the HGTD [5] is proposed. The HGTD will be used to measure the times of minimum-ionizing particles with a time resolution of approximately 30 ps per track during the initial phase of operation of the HL-LHC. As the operation progresses, the time resolution will increase to 50 ps at the end of the operation

The HGTD will be situated in the the space between the ITk and end-cap calorimeters, approximately 3.5 meters from the IP. The positioning of the HGTD in the ATLAS detector can be seen in figure 1.14.

The detector has a radial extension ranging from 110mm to 1000mm. Its active area will cover the pseudo-rapidity range of $2.4 < |\eta| < 4.0$, corresponding to a radial extension of 120 mm to 640 mm.

The HGTD end-cap consists of a hermetic vessel, two instrumented double-sided layers (mounted on two cooling/support disks), and two moderator pieces placed inside and outside the hermetic vessel. The cooling/support disks are divided into two half circles, and the layers are rotated in opposite directions by 15 to 20° to optimize hit efficiency. The total thickness of the detector along the z direction, including moderators, supports, and vessel covers, is 125 mm.

Due to these spatial constraints a silicon-based timing detector technology was chosen, with sensors required to be thin and configurable in arrays while providing excellent time resolution ($\sim 30\ ps$). LGAD pads of 1.3 $mm \times 1.3\ mm$ with an active thickness of 50 μm were the chosen

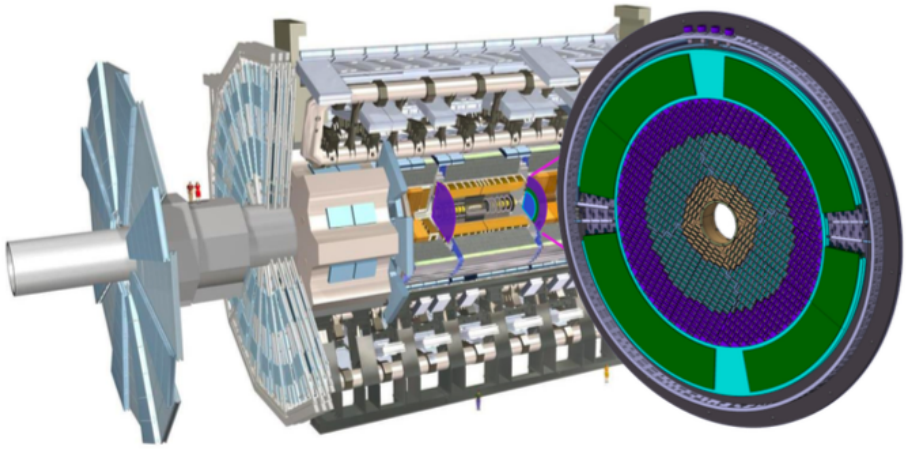

Figure 1.14: Position of the two HGTD disks within the ATLAS Detector [5]

technology for the HGTD. To counter the impact of radiation, the sensors will be operated at low temperatures (-30 °C).

These sensors will be bump bonded to an Application-Specific Integrated Circuit (ASIC) called ATLAS LGAD Time Read Out Chip (ALTIROC). This ASIC will amplify and sample the signals from the sensors, and route them through the data acquisition network. The ASIC will also be able to count the number of hits registered in the sensors and transmit it at 40 MHz, enabling bunch-per-bunch luminosity measurements, and the implementation of a minimum-bias trigger.

The HGTD is based on a three ring layout with three different active regions: $120\ mm < r < 230\ mm$, $230\ mm < r < 470\ mm$, and $470\ mm < r < 640\ mm$. Outside the third ring is where the peripheral electronics will be placed. Figure 1.15 presents the global view of the detector and its main components.

Each HGTD sensor is made up of 450 (15×30) LGAD pads ($1.3mm \times 1.3mm$), with an area of about $2 \times 4\ cm^2$. An HGTD module consists of an LGAD sensor and two ASICs. As mentioned above, these are connected through a bump bonding process. There is a total of 8032 modules in the HGTD detector.

The module size and layout were optimized in order to maximize coverage. Each sensor layer is double sided, modules are mounted on both sides of a cooling disk. The modules on each side are designed to overlap a certain amount depending on the ring they are in (figure 1.16) and thus giving a approximately uniform performance independent of radial position.

The modules are organized in rows and connected to Peripheral Electronics Board (PEB)s located at the outer radius of the active detector area through a flex cable.

This flex cable consists of two parts: a module flex that is permanently glued to the backside

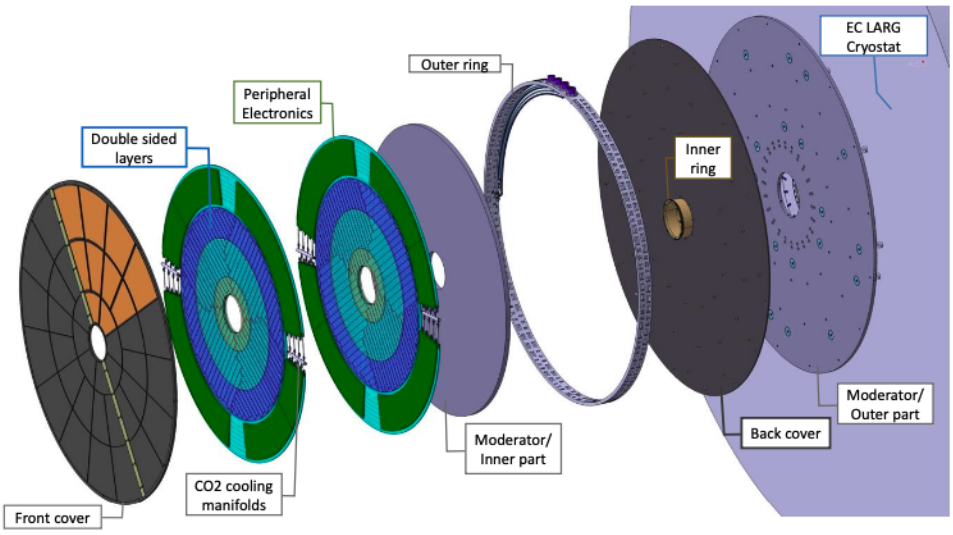

Figure 1.15: An overview of the High Granularity Timing Detector (HGTD) to be installed on each of the two end-cap calorimeters. Various components of the HGTD are depicted: the hermetic vessel (consisting of front and rear covers, as well as an outer ring), the two double-sided layers that are instrumented and mounted on two cooling disks with sensors on the front and back of each cooling disk, and the two neutron moderator pieces that are positioned inside and outside the hermetic vessel. [5]

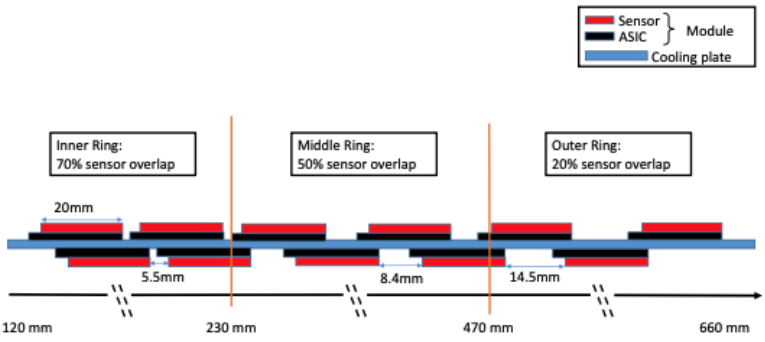

Figure 1.16: Overlap between the modules on the front and back of the cooling disk. There is a sensor overlap of 20% for r $>$ 470 mm, 54% for 230 mm $<$ r $<$ 470 mm and 70% for r $<$ 230 mm.[5]

of the sensor and a long flex tail to connect to the PEBs. The flex cable transmits the signal from the module to the peripheral electronics boards. It also transmits the power, clock and bias voltage from the peripheral electronics to the module.

The signal lines of the ASIC are wire bonded on one side of the module flex, while the sensor is biased through a hole in the module flex. This arrangement reduces the likelihood of interference between the high voltage lines and other signals. The length of the tail varies depending on the module's position within the detector.

1.8 LGAD Sensor

As previously mentioned, the sensors are based on LGAD technology. LGADs are silicon detectors consisting of a reverse-biased p-n junction, featuring heavily doped n and p regions (n^+ and p^+) along with an additional p layer positioned beneath the n^+ region. The schematic of the cross section of one of these sensors can be seen in figure 1.17.

Operating in reverse bias mode, the sensor functions in the following manner: when a charged particle traverses the sensor, it generates electron-hole pairs within the depletion region located between the n^+ and p^+ layers. Due to the reverse bias, these charge carriers experience a strong electric field that pushes them towards the respective terminals – electrons towards the n^+ layer and holes towards the p^+ layer. As the electrons approach the n^+ layer, they encounter another powerful electric field from the p-n^+ junction, accelerating them and triggering an avalanche effect, leading to signal amplification.

It is anticipated that the performance of LGAD sensors will degrade as a result of irradiation. However, this effect can be mitigated by raising the bias voltage. As a consequence, the voltage is gradually increased from the initial stages until the end of the detector's lifetime.

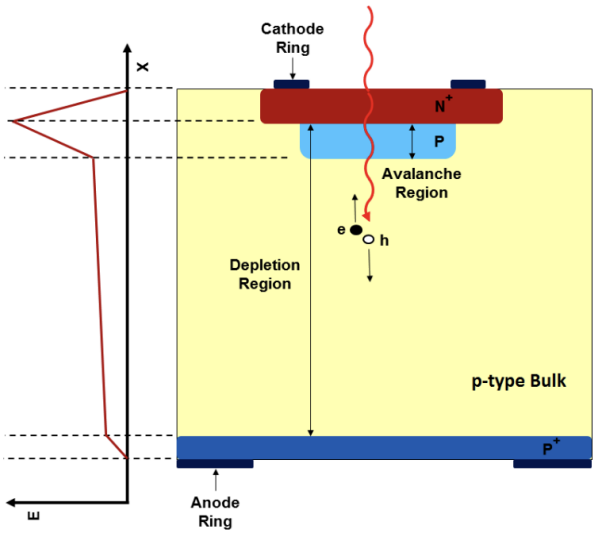

Figure 1.17: Cross section schematic of an LGAD sensor[5]

1.9 High Voltage (HV) System

Each of these 8032 modules requires an individual bias voltage that will range from approximately 300 volts at the beginning of the HL-LHC to 800 volts. Due to exposure to high radiation conditions, the sensors suffer from gain degradation, thus needing a higher voltage to power them. The degradation of a module's performance is significantly influenced by its radial position , as the radiation depends strongly on this distance.

As a result, it is expected that modules located in close proximity to one another will require the same voltage. Taking this into consideration, the proposed solution is for two modules to share a bias supply. This is a cost effective solution which will require 2008 HV channels per end-cap.

The high voltage that is going to be supplied to the 8032 LGAD sensor modules is to be provided by commercial power supplies with multi-channel rack-mounted units located in the service cavern (USA15). The bias HV is brought to low pass filter units. The then filtered HV is transferred to the PEBs, which are located at the outer radius of the active detector area.

The characterization and testing of these filter units is the core of the work presented in this thesis and will be further discussed in chapter 3.

2 Patch Panel Filters

The high voltage that is going to be supplied to the 8032 LGAD sensor modules is to be provided by commercial supplies with multi-channel rack-mounted units located in the service cavern (USA15). These power supplies will have individually floating channels. The bias HV is brought to low pass filter units in the more hostile environment (magnetic field and radiation wise) at the PP-EC area (Fig. 2.1) at the end-cap calorimeters via 100 m shielded Type III cables [23].

The then filtered HV is transferred through 15 m shielded Type II cables [23] from where they pass via HV pigtails to the PEBs, which are located at the outer radius of the active detector area. Additionally an extra low pass filter is placed on the module flex cables near the sensors.

In addition to their primary function as low-pass filters, the filter units located in the PP-EC area will also serve as patch panels, enabling the selection and sharing of power supplies for the individual sensor modules. Figure 2.2 shows the general HGTD HV layout.

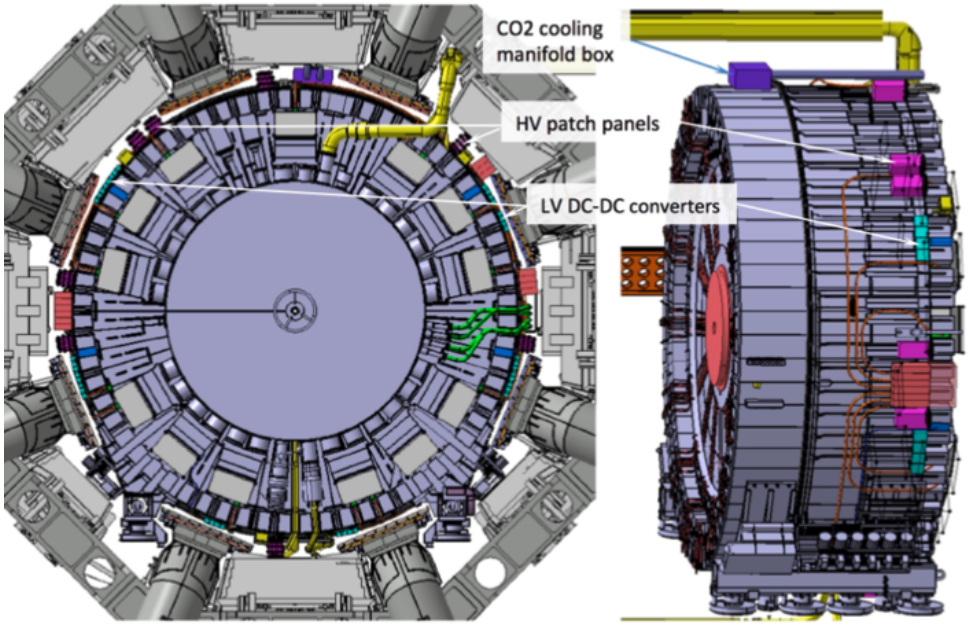

Figure 2.1: The preliminary design of the HGTD patch panels (PP-EC) located on the end-cap calorimeter surface. The PP-EC components have been placed in various locations around the end-cap surface of the calorimeter, as indicated by arrows.[5]

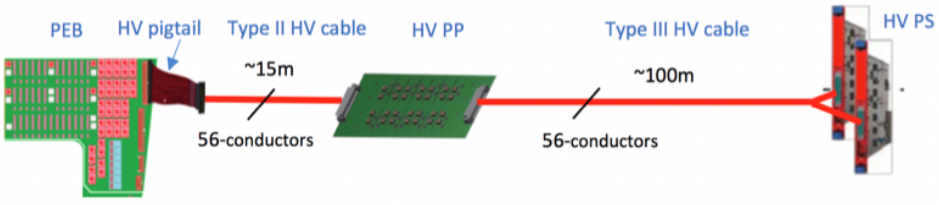

Figure 2.2: The HGTD HV layout. The HV units are in the service cavern (USA15) protected from radiation while de HV-PP are in the PP-EC area closer to the detector with a shorter connection to the PEB's via 15 m shielded Type II cables.[6]

2.1 Design

Due to the maximum number of high voltage channels for a single PEB being 56, and given the limited space available for connectors on the outer ring of the HGTD vessel, it has been determined that two 56-pin connectors per PEB will be utilized, each matching 28 pair cables. This configuration results in a preferred modularity of 14 or 28 channels per HV supply module. In a similar manner, the filter units should also be designed to accommodate 28 high voltage channels.

A modular design is proposed for the filter units located in the PP-EC area. The design includes filter boards with 14 RC-RC low pass filters, as well as capacitors for CM noise rejection, as there is limited space for CM filters near or within the detector vessel. CM noise affects the common-mode voltage, causing it to deviate from its expected value. This can result in errors in the transmitted or processed signal, as well as reduced signal-to-noise ratio. Each filter module comprises two filter boards, housed in an aluminum box, which provides mechanical support and isolates each pair of boards within a Faraday cage. Ten filter modules are supported by an aluminum support structure to create a filter unit. Aluminum was selected as the preferred material due to its non-magnetic properties and resistance to radiation effects. A total of sixteen filter units will be installed in the PP-EC area on each TileCal endcap surface.

2.2 Grounding

Most particle detectors work with very low signal levels and for them to operate successfully close attention must be paid to the grounding, shielding, and power distribution of each subdetector system. This is a particularly important issue for the ATLAS experiment given the large cost required to redo any system. For this reason the LHC has established guidelines that must be adhered to by each subdetector group during the design stage of their detector. Some LHC experiments have their own documentation on grounding and shielding which is the case for the ATLAS experiment [24].

ATLAS guidelines tell us that High Voltage Power Supplies should be floating, this means that the supply is not connected to earth ground and so its reference voltage is "floating" relative to ground and isolated from it. As illustrated in Figure 2.4, the high voltage power supplies in the USA15 service cavern will be floating and housed within a Faraday cage connected to the local earth in the USA15. Each HV channel is individually floating.

Ground loops occur when two points in a circuit are intended to share a common ground reference, but in reality there exists a potential difference between the points, leading to an

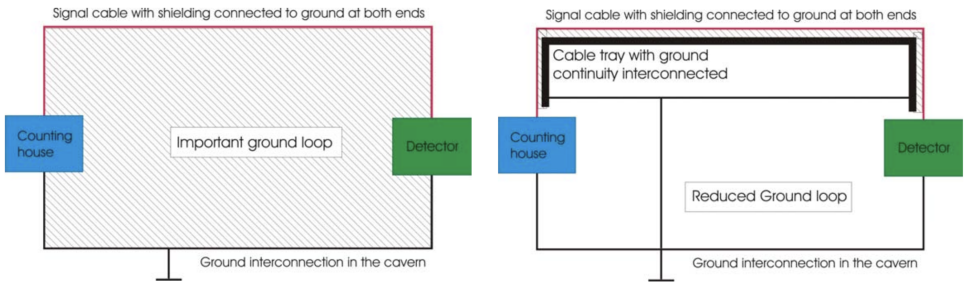

Figure 2.3: Total area of a ground loop greatly reduced by a grounded cable shield[7]

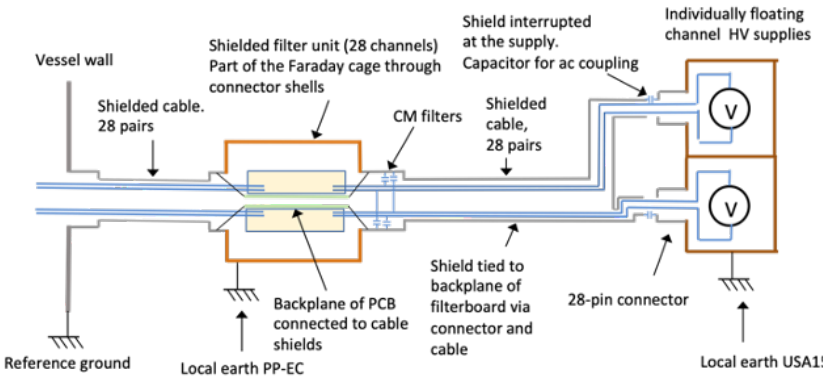

Figure 2.4: Schematic of the current Grounding and Shielding Solution of the HV supply system [8]

unwanted flow of current between them and resulting in interference and noise in the signals. The greater the surface area of a ground loop, the more substantial the ground loop currents collected and thus the more significant the noise and interference. When high voltage is utilized and distribution is made via shielded cables it is likely for the shield of the cable to be connected to earth. This is done in order to reduce the effective surface area of the ground loop seen by a signal transmitted over long distance (Fig. 2.3). An alternative approach predicted by the ATLAS guidelines is to distribute the HV power and HV power return via two conductor cables sharing an outer shield.

The cables connecting the supply modules to the filter modules will be grounded. To prevent ground loops between the high voltage supplies and the vessel Faraday cage, the supply cable shield is interrupted at the supply. The vessel's Faraday cage is then linked to the vessel's reference ground. The shield of the filter unit serves as an extension of the vessel's Faraday cage and is connected with the cable shields. Additionally, the filter unit's shield is connected to the PP-EC's local ground, and the filter board's backplane will be connected to the cable shields. As mentioned before, due to limited space for CM filters within or near the vessel, the common mode rejection capacitors will be integrated into the filter boards.

In order to bias the LGAD sensors high voltage passes through flex tail cables from the

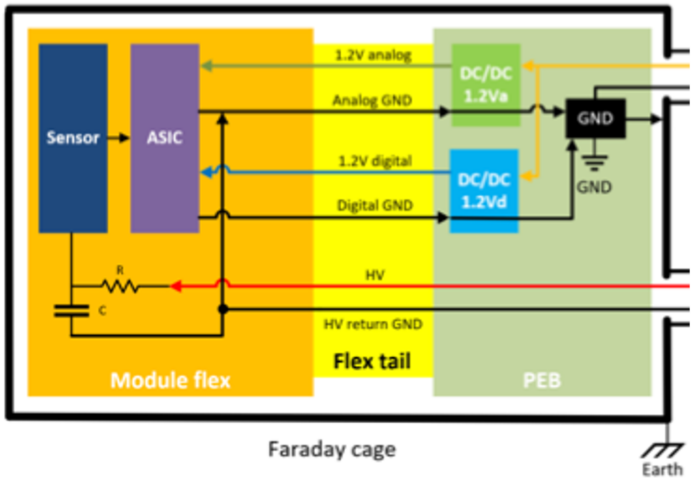

Figure 2.5: Grounding schematic of the HGTD modules[9]

PEB's to the individual modules. The HV return ground (GND) is referenced to ground by connection to the analog power ground of the PEB which is then referenced to the experiment ground via the low voltage power ground at the PEB. The extra low-pass filter on the module flex cables near the sensor is also indicated (Fig. 2.5). Since there is a voltage drop along the flex cables, the potential of the HV return line may vary from module to module by a few mV, depending on flex tail length.

2.3 Requirements

Due to where they are located (PP-EC) each filter unit should be resistant to magnetic fields of up to 0.5 T and a total ionizing dose (TID) of 15.0 Gy and 1 MeV neq fluence $1.0 \times 10^{12} cm^2$ To ensure a comfortable safety margin with regards to the anticipated bias voltage at the end of the HGTD life, the connections and filter must be able to withstand a voltage of up to 900 volts without significant leakage. Currents of up to 3 mA per channel are expected . Additionally, mechanical stability and ease of access during maintenance must be considered. The overall dimensions of the filter units should be 360 x 195 x 104 millimeters, in order to be compatible with the available space on the TileCal surface. Determining the need and optimal parameters for such a filter unit, as well as its parameters, is challenging as it is difficult to conduct tests in the final noise environment.

In conclusion the requirements for this filter can be summarized by:

- Functional requirements
  - AC noise filtering

- Non functional requirements
  - Voltages up to 900V with no significative DC current leaks
  - 3mA currents per channel
  - Capable of withstanding magnetic field (up to $0,5\ T$) and radiation hard (up to 15,0 Gy and dose by 1 MeV neq (neutron-equivalent) fluence $1.0 \times 10^{12}\ cm^{-2}$
  - Mechanical stability and ease of access
  - Dimensions: $360 \times 195 \times 104\ mm^3$

2.4 Filter Board Background

A preliminary design of the filter board is available Appendix (B). As it was proposed, each filter board is composed of 14 RC-RC low pass filters as well as capacitors for CM rejection (Fig. 2.8). Each filter module has 2 filter boards housed in an aluminum box that acts as a Faraday cage and provides both mechanical support and insulation (Fig. 2.7). Aluminium is the material of choice due to its radiation hardness (weak activation by neutrons), and its resistance to magnetic fields since it is paramagnetic.

Certain filter components, specifically the capacitors and resistors for the RC filters, have been selected. The chosen values, 47 nF for capacitors and 10 $k\Omega$ for resistors, will lead to a cutoff frequency of approximately 126.4 Hz. The rationale behind these selected values is to achieve a sufficiently low cutoff frequency while maintaining moderate capacitance and avoiding excessive voltage drop across the resistors. Again it is important to remind that determining the necessary and optimal parameters for such a filter unit is a complex task due to challenges in conducting tests in the final noise environment.

Towards the end of the sensor's lifetime, a bias voltage of up to 900 V will be applied to the sensors. Considering this voltage, there will be a voltage drop of 30 V across the resistors, resulting in a power dissipation of 90 mW per resistor per channel.

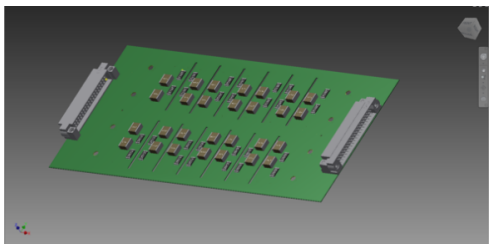

Figure 2.6: Filter module containing two filter boards and connectors. [9]

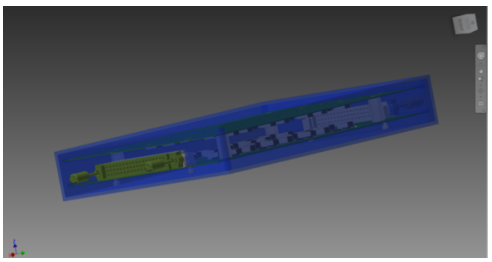

Figure 2.7: Individual filter board with 14 2nd order low-pass filters [9]

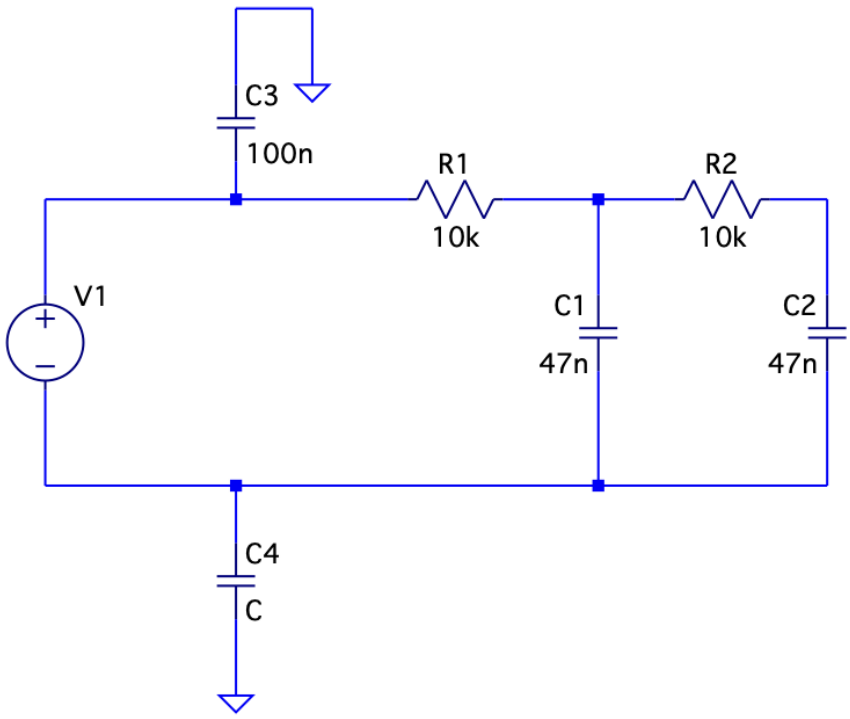

Figure 2.8: The diagram illustrates the components comprising the 2nd-order filter, including resistances R1 and R2, capacitors C1 and C2. Additionally, decoupling capacitors C3 and C4 are included to serve as effective noise filters for CM noise

The purpose of this thesis is to evaluate and assess the performance of the filter, examining its behavior and integration within the HV system. Through the characterization and comprehension of the filter's operation, a deeper understanding will be achieved, facilitating appropriate planning for the HV system. This will lead to insights into expected outcomes, areas for improvement, and potential modifications to be made.

3 Experimental Work

To characterize the filter, a series of tests were devised that involved the use of support electronics, signal injection into the filter, and measurement using a programmable oscilloscope and function generator. The testing pipeline encompasses the measurement of the transfer function, cutoff frequency, shielding, the effects of the DC component, ripple, cross-talk, common mode noise, and leakage currents. In order to elucidate the outcomes obtained from these diverse tests, we developed a model and conducted simulations.

The following sections delineate the procedures employed for conducting the tests, present their results, and provide a discussion of them. Ultimately, models and corresponding simulations are presented to facilitate the comprehension of the obtained results.

3.1 Component Values

Prior to the commencement of this study, the capacitance and resistance values for the filter had already been selected. However, determining the appropriate value for the decoupling capacitors remained necessary. To address this, a simulation was done with the objective of assessing the capacitors' influence on dampening common mode noise, as well as their overall impact on the filter's performance. The simulation's goal was to identify an appropriate value for the decoupling capacitors.

Common mode noise refers to unwanted electrical interference or disturbances that affect multiple signal conductors or components in an electrical circuit or system in the same way or at the same relative voltage level. Unlike differential mode noise, which appears as a voltage difference between two signal conductors, common mode noise manifests as voltage fluctuations or disturbances that are simultaneously present on all the signal conductors with respect to a common reference, such as ground.

Two schematics were created to compare how the filter performs under the same conditions of common mode noise. One diagram displays only the filter, while the other incorporates both the filter and the decoupling capacitors. These diagrams can be observed in Figure 3.1 and

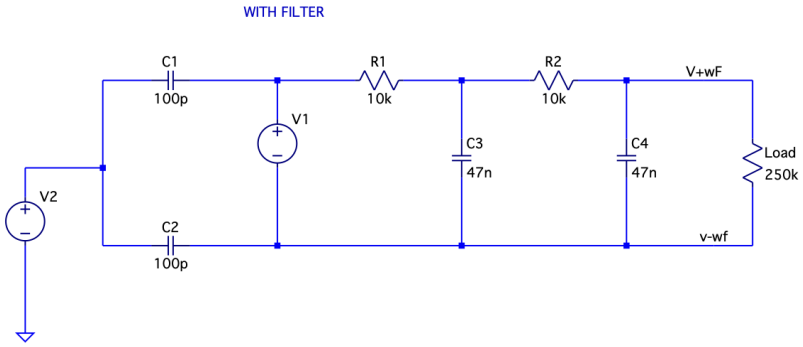

Figure 3.1: Schematic for simulating common mode noise, depicting only the filter without any decoupling capacitors for common mode noise attenuation

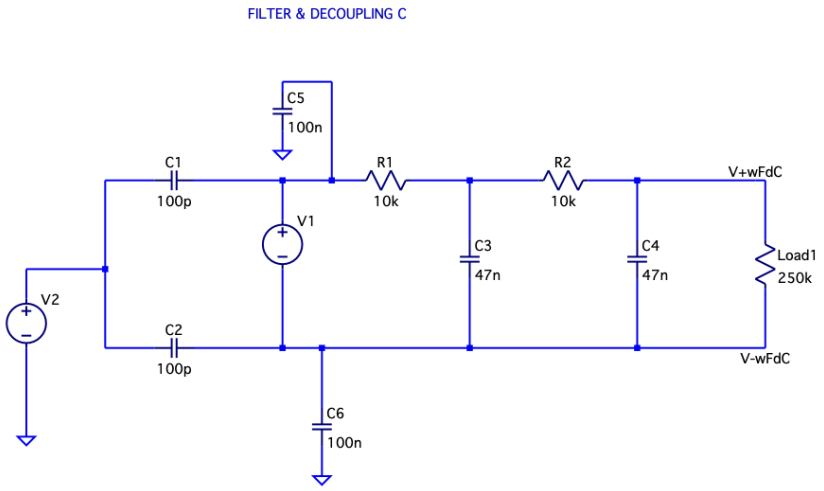

Figure 3.2: Schematic for simulating common mode noise, depicting only the filter and decoupling capacitors for common mode noise attenuation

Figure 3.2. Various schematics and simulation methods were tested to replicate common mode noise, but only the ones corresponding to the final and chosen approach are shown.

In Figure 3.1, V1 represents the primary power supply, while V2, decoupled from V1 using capacitors C1 and C2, serves as the supply responsible for introducing common mode noise into the system. The RCRC filter composed of R1, R2, C3, and C4, positioned between the main power supply and the load is also present. A resistor load was selected to approximate a current of 3mA, which corresponds to the maximum expected value in this setup.

Lastly, in Figure 3.2, similar to Figure 3.1, the same components are present, but additional decoupling capacitors are placed at the input, represented by C5 and C6, these form the common mode noise filter.

Examining the Bode plot of the filter's frequency response to common mode noise (fig. 3.3),

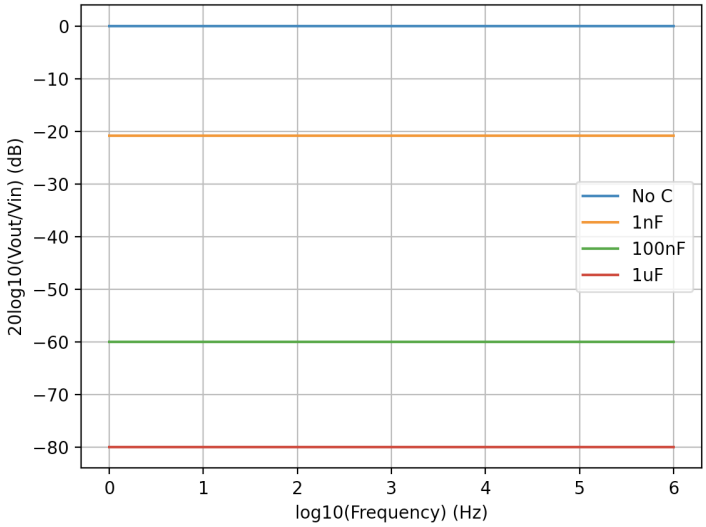

Figure 3.3: Bode plot of the filter's frequency response to common mode noise

where the output at the load is analyzed in relation to the varying voltage frequency of V2, which injects the common mode noise, it becomes evident that the response remains flat. This indicates that the attenuation of common mode noise is independent of its frequency. Furthermore, it is observed that larger decoupling capacitors lead to higher attenuation.

The transfer curve for differential noise was also examined under various conditions, including tests without decoupling capacitors and with decoupling capacitors of different values. The results indicated that the presence and size of the decoupling capacitors had no impact on the transfer curve of the filter for differential noise.

In conclusion, this simulation experiment indicates that larger decoupling capacitors result in improved common mode noise filtering without affecting the transfer curve of the filter. Based on these findings, the decision was made to utilize decoupling capacitors with a capacitance of 100nF.

3.2 Tranfer Curve

When figuring out how to test and understand the low-pass filter board's performance, the transfer function emerged as a crucial measure. It helps us compare the actual behavior of the filter at different frequencies with what we expect from theory or simulations. By doing this, we can check if the filter is working as intended and detect any issues or deviations from what we predicted. So, the transfer function is an important tool for evaluating and ensuring the proper functioning of the low-pass filter board.

It is important to acknowledge that the analysis conducted in this study was performed

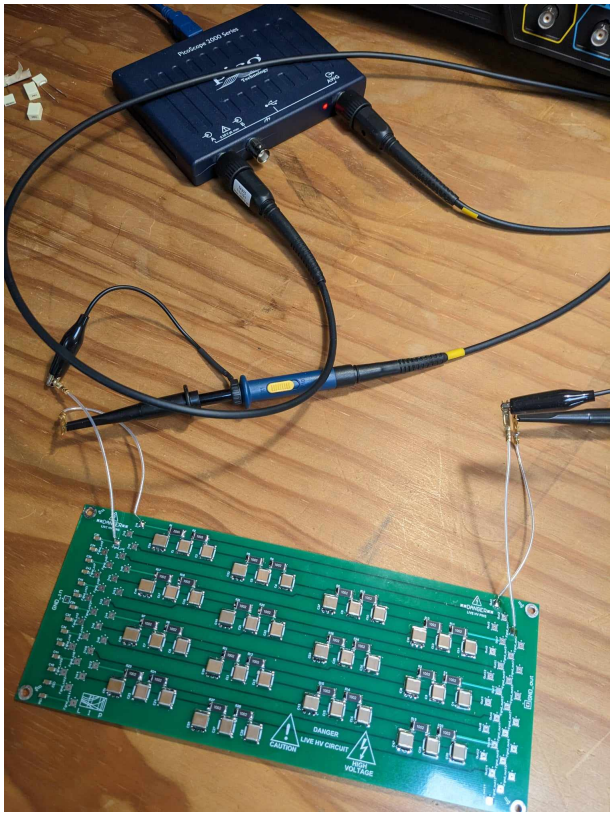

Figure 3.4: Transfer curve measuring setup using PicoScope.

with the future perspective of filter testing automation in mind. Considering that the HGTD is expected to utilize a substantial number of 574 filter boards, efficient and timely testing of these filters becomes critical. This context of large-scale testing and automation may offer insights into the reasoning behind certain decision-making.

3.2.1 Experimental Setup

To address this challenge, the available material was a PicoScope 2208B [25], a programmable USB oscilloscope with an incorporated signal generator. This choice allowed for programmable and automated measurements, enabling more efficient and precise data collection, better control over measurement parameters, and seamless integration into potential future automation processes.

Using the PicoScope SDK and the respective Python wrappers [26], a program was developed to measure the filter transfer curve. The program's functionality is illustrated in the diagram shown in Figure 3.5. The results obtained for one of the filter boards channel are presented in Figure 3.6. The transfer curve shown in the graph was generated using three measurements per frequency point. Notably, the error is depicted on the graph, and it is observed to be quite small. The setup can be seen in figure 3.4.

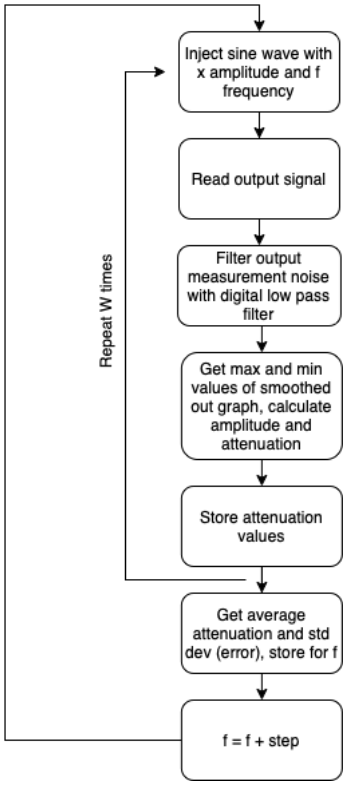

Figure 3.5: Schematic depicting program's pseudocode, illustrating its fundamental operational principles.

The measurement process was performed for all channels to ensure comprehensive data collection. However, for the sake of simplicity and redundancy, only one channel's results are presented here. It is worth noting that the behavior of the other channels was found to be very similar, indicating consistent performance across all channels (Fig. A.3).

The measurement of the filter's transfer curve was limited by the PicoScope's voltage amplitude range of 2V, restricting measurements to approximately 10kHz. This limitation arises from the fact that, at an attenuation of -70 dB, the output signal's amplitude falls below 1mV, which makes accurate measurement challenging, given the PicoScope's minimum reading range of $\pm$20mV and that at this point, measurement noise has higher amplitude than the signal itself, leading to a poor signal-to-noise ratio, making further measurements unreliable and difficult to interpret. Consequently, precise analysis beyond this frequency range becomes impractical.

3.2.2 Deviation from theory

With the gathered information, it is possible to compare the observed behavior of the transfer curve with the theoretic correct transfer curve. The theoretical transfer curve can be determined through simulation and analytical calculations, as outlined in Appendix A. This theoretical

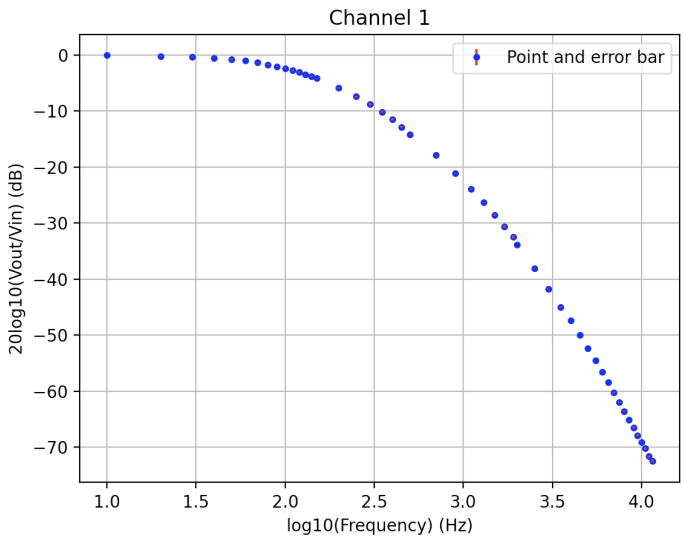

Figure 3.6: Transfer function of the filter board's first channel as determined through measurements employing a PicoScope.

curve is then plotted alongside the retrieved data, allowing for a visual comparison, as depicted in Figure 3.7.

The comparison between the observed data and the theoretical transfer curve reveals an unexpected visible deviation that emerges around 2kHz. Despite the deviation seemingly leading to improved filtering beyond what was initially anticipated, it remains crucial to comprehend the underlying cause of this discrepancy. Understanding the origin of this deviation is of importance to gain insights into the filter's behavior and to validate the theoretical model.

While investigating the potential causes behind the observed deviation, two main hypotheses emerged as possible explanations.

One hypothesis was based on the observation that the amplitude of the PicoScope's wave generator appeared to vary with frequency. Specifically, when setting a fixed amplitude of 2V, the PicoScope seemed unable to maintain this value as the frequency increased, leading to a slight decrease in amplitude. This effect was noticed when measuring the PicoScope's AWG with both its own oscilloscope and a separate oscilloscope (Rigol MSO5204). However, this effect was not observed when using a tabletop wave generator and measuring with both the oscilloscope and PicoScope. As a result, it was inferred that the PicoScope's AWG might be the source of this discrepancy. The variation of the amplitude of a sinusoidal wave, which was intended to have a fixed amplitude of 2V, is depicted in Figure 3.9. The plot illustrates how the amplitude changes as a function of the wave's frequency. This suggests that the sinusoidal wave generated by the PicoScope's AWG and injected into the filter might have a lower amplitude than expected, which could explain the observed deviation from the theoretical prediction.

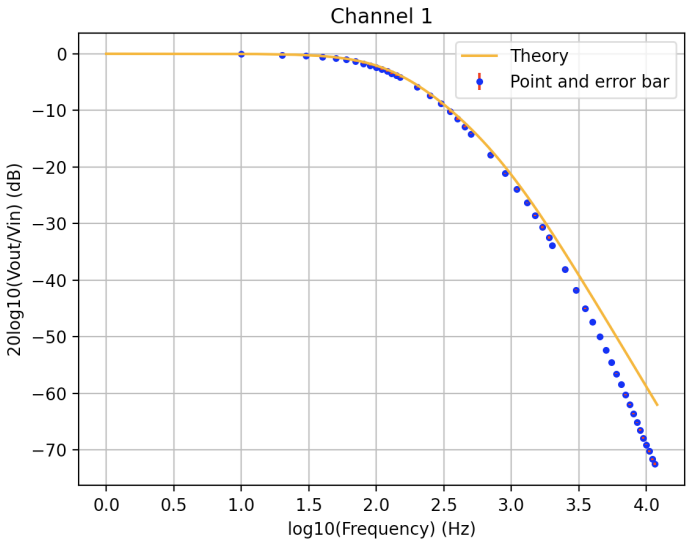

Figure 3.7: Transfer function of the filter board's first channel as determined through measurements employing a PicoScope compared to initial theory

This explanation initially suggested a malfunction in the PicoScope's AWG, but upon conducting a more thorough investigation, a plausible reason emerged for the observed behavior of the wave generator. This new insight presents a potential explanation that effectively rules out malfunctioning as the sole cause of the decrease in amplitude with frequency.

The observed effect may be explained by the combination of two overlooked factors: the oscilloscope's input capacitance and the wave generator's output resistance. Oscilloscopes generally exhibit a small input capacitance, which is an inherent characteristic of their input circuitry. This capacitance can be represented as a parallel capacitor connected to the input. Manufacturers typically specify this input capacitance in the instrument's datasheet. It is important to consider this input capacitance, especially when conducting measurements at higher frequencies.

The output resistance represents the equivalent resistance of the signal generator at its output terminals. When combined with the input capacitance, these two components form a low-pass filter, leading to an inaccurate measurement of the signal's amplitude by the oscilloscope. Despite the signal having the expected amplitude, the oscilloscope perceives it differently, which could explain the apparent dependence of amplitude on frequency.

The PicoScope's datasheet [25] indicates an output resistance of 600 Ω , but it does not provide information regarding its input capacitance. In contrast, the datasheet of the oscilloscope used [27] specifies an input capacitance of 17 pF.

These represent the two known variables in the circuit. Other factors to consider include the probe's tip capacitance, the resistance of the probe itself, as well as the resistance and capacitance of the probe's compensation. These variables can be incorporated as shown in the schematic of

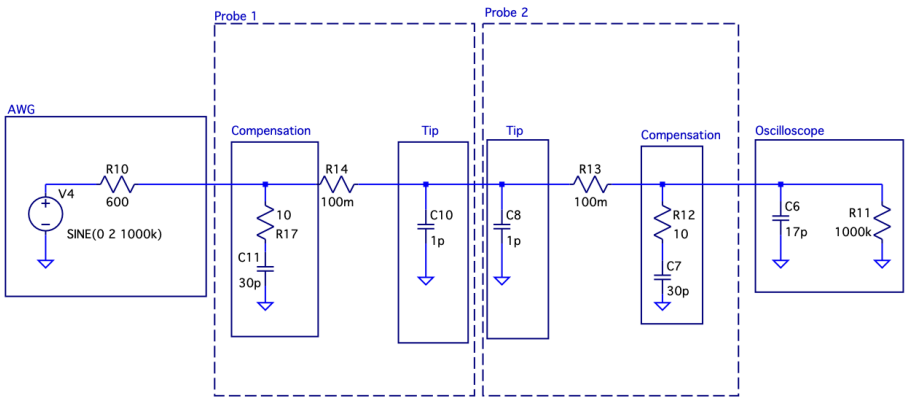

Figure 3.8: Circuit schematic simulation utilized to discern whether the reduction in amplitude observed across varying frequencies is attributable to a malfunction in the AWG) or is influenced by the component values associated with the measuring instruments.

Figure 3.8. The assigned values for these components are reasonable and plausible, and they were appropriately adjusted to align the theoretical model with the observed measurements in reality.

By simulating the circuit as shown in the schematic of Figure 3.8, we can obtain the transfer curve and examine how the perceived amplitude changes with frequency. This schematic accounts for the utilization of two probes in the measurement process. Subsequently, we can compare this curve with the experimental results obtained by measuring the PicoScope's output wave at 2 V for different frequencies using the oscilloscope, as depicted in Figure 3.9.

Upon examining the plot and comparing the experimental results to the constructed model, it is reasonable to assert that the model effectively describes the observed phenomenon. The reason why this phenomenon is not observable with the tabletop generator is due to its significantly lower output resistance. As depicted in Figure 3.9, the curve for a 50 Ω output resistance exhibits a less pronounced decline, indicating that the filter's impact is not as significant.

The developed model can be integrated with the filter to assess whether it influences the transfer curve in a manner that aligns with the observed behavior. The schematic representation of this integration can be observed in Figure 3.10. By plotting the new transfer curve alongside the previous one and the measured results (fig. 3.11), it becomes evident that this integration alone is insufficient to account for the observed deviation. As a result, the cause of the deviation remains an unresolved question.

As mentioned earlier, two primary hypotheses emerged as potential explanations for the observed deviation. The second hypothesis suggests that the combination of the previously overlooked output resistance and the 100 nF decoupling capacitor forms a filter, which might

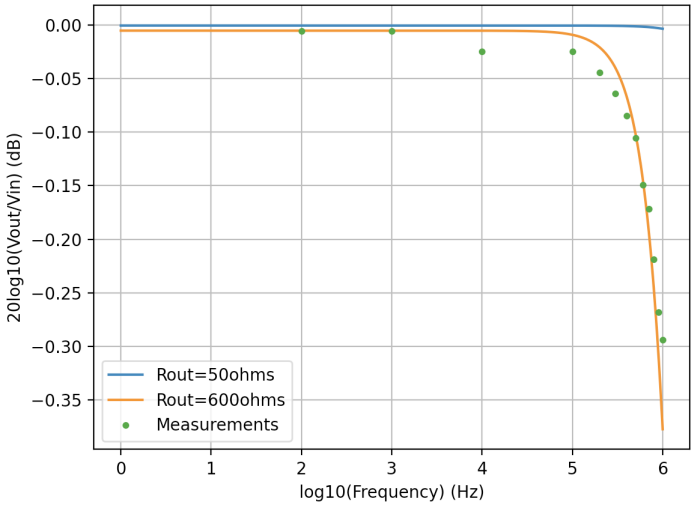

Figure 3.9: Experimental outcomes obtained from the aforementioned schematic juxtaposed with the simulation results of the same schematic, considering two distinct output resistances

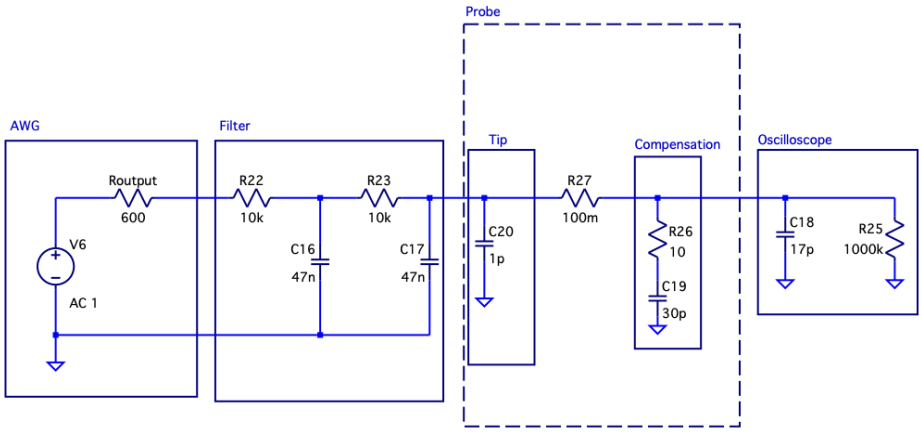

Figure 3.10: Schematic for measuring the transfer curve with integrated models for probes and PicoScope.

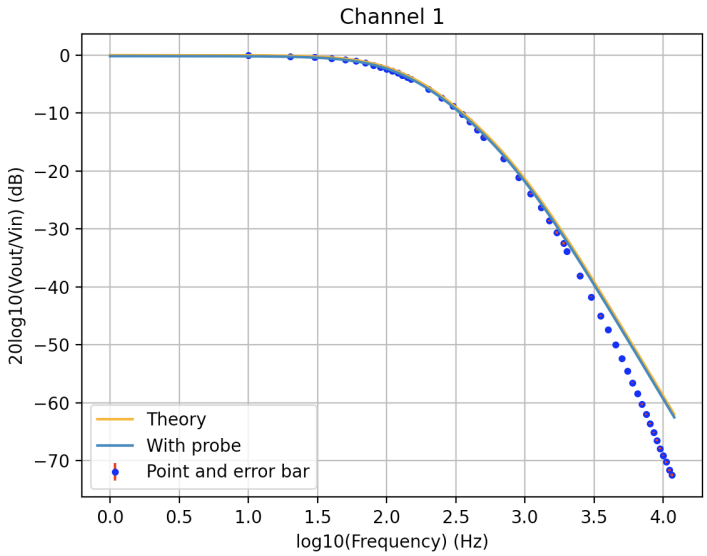

Figure 3.11: Transfer function of the filter board's first channel as determined through measurements employing a PicoScope compared with the initial theoretical prediction and the simulated schematic illustrated in Figure 3.10

account for the downward deviation of the transfer curve.

This hypothesis can be readily tested by utilizing the schematic shown in Figure 3.12 to derive the transfer curve through either simulation or analytical methods(Appendix 3.13). The resulting transfer curve from this new model can then be plotted alongside the experimental transfer curve, allowing a direct comparison between the two. Based on the comparison, it is reasonable to conclude that this hypothesis accurately models the observed behavior.

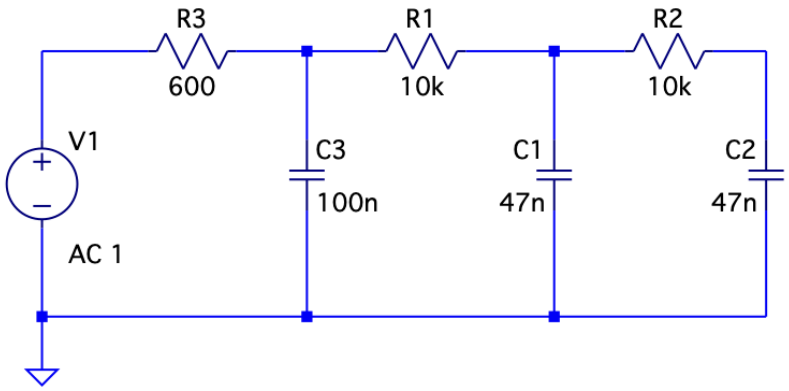

Figure 3.12: Filter schematic representation that incorporates the output resistance of the AWG (R3) and the decoupling capacitor (C3) for the filter.

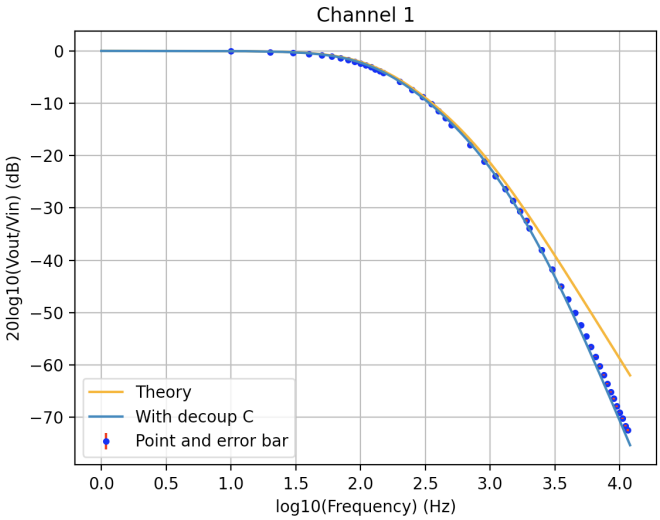

Figure 3.13: Transfer function of the filter board's first channel as determined through measurements employing a PicoScope compared with the initial theoretical prediction and the simulated schematic illustrated in Figure 3.12

3.3 Cutoff Frequency

From a perspective of future automation, the notion arose that using a performance metric for the filter, which did not entail scrutinizing graphs for deviations from theory, might prove advantageous in terms of efficiency. This idea aimed to simplify the assessment process by quantifying the filter's performance. Moreover, the acquisition of transfer curves can be time-consuming, depending on factors such as the number of data points and the number measurements done at each point. For instance, the graphs presented in the previous section each required approximately five minutes to compile. Therefore, in consideration of future endeavors, expediting this process could be beneficial.

To address these concerns, an experiment was conducted where the cutoff point served as a performance metric. This approach avoided the necessity of measuring the entire curve; instead, the focus was directed to the initial segment where the expected cutoff point lays. Additionally, the advantage of this metric lays in its numeric nature; if the cutoff point diverged significantly from the anticipated value, it would signal a potential issue with the filter that could be investigated further. In essence, this concept aimed at a swifter and more pragmatic method compared to the previous practice of scrutinizing a complete curve.

Utilizing the same PicoScope and SDK mentioned previously, a dedicated program was developed, as depicted in the functional schematic in Figure 3.14. Essentially, its purpose was to focus on measuring the initial segment of the curve. By fitting the theoretical curve to these specific data points, the intention was to identify the frequency corresponding to the cutoff point or the -3dB point. This process was iterated multiple times until a substantial dataset was acquired, allowing for a comprehensive assessment of the filter's cutoff point.

The fitting procedure entailed employing Equation A.1, with the fitting parameter being RC. The initial outcomes indicated that, to achieve a substantial dataset resembling a normal distribution, the program would need to gather approximately 100 measurements. However, this collection process was considerably more time-consuming compared to conducting the complete transfer curve measurements 3-5 times. Hence, this filter testing method was invalidated as it is less time-efficient than acquiring the entire transfer curve with also less information. The histogram in Figure 3.15 portrays the distribution of measurements for a specific channel, involving 100 data points for the histogram.

Figure 3.16 displays a histogram representing 100 measurements of cutoff frequencies conducted across various channels. This approach was employed in an attempt to investigate the variability between different channels using the specified method

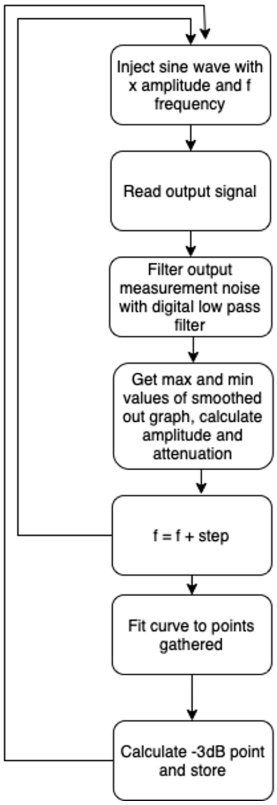

Figure 3.14: Schematic depicting program's pseudocode, illustrating its fundamental operational principles.

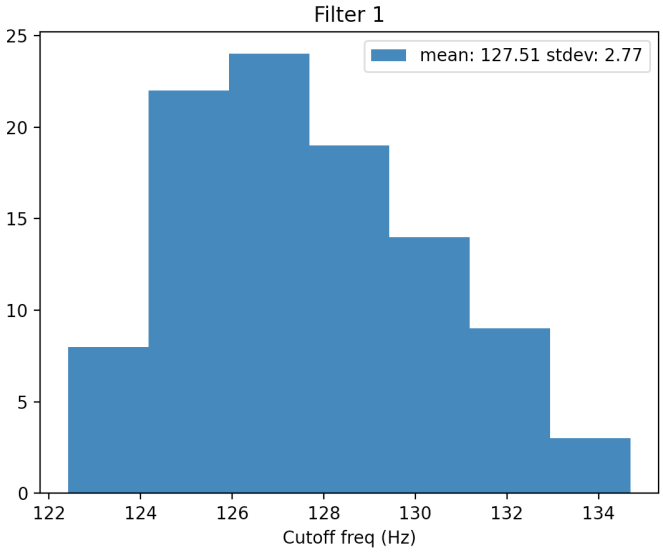

Figure 3.15: Histogram of the results of measuring 100 cutoff frequencies for channel 1

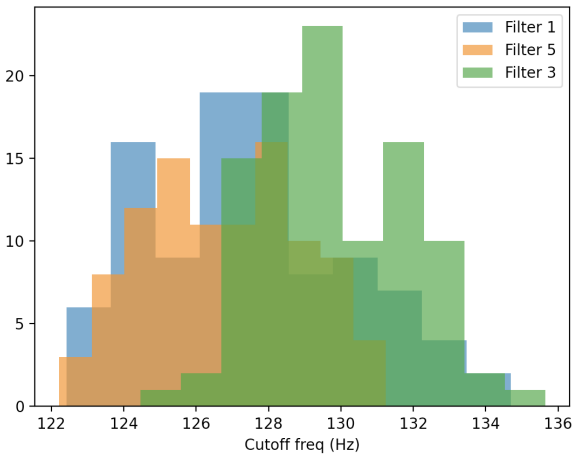

Figure 3.16: Histograms of the measurements obtained for 100 cutoff frequencies are depicted for channel 1, channel 2, and channel 3, presented in a stacked format.

3.4 Shielding effect

In the final environment as explained in section 2.1 the each filter module comprises two filter boards, housed in an aluminum box, which provides mechanical support and isolates each pair of boards within a Faraday cage.

The objective here was to examine the impact of this shield and determine how it influenced the filter's behavior. The goal was to assess whether it introduced any new factors that might affect the transfer curve. Additionally, the investigation aimed to determine whether it reduced reading noise, potentially simplifying the measurement of the transfer curve with the PicoScope across higher frequencies.

To investigate this, a comparison was made between the transfer curves of channels with the board alone and those with the board equipped with the shield (Fig. 3.17). Figure 3.18 illustrates the transfer curves for both scenarios. Notably, there is no discernible difference between the two transfer curves. The noise level with the shield remains approximately the same and does not appear to enable improved high-frequency readings.

These tests do not provide conclusive evidence regarding noise level attenuation, primarily because the test environment was not characterized by high levels of noise. Furthermore, the frequency range studied may not encompass the frequencies most susceptible to external noise, as they are relatively low. However, the results do indicate that the introduction of a shield does not appear to substantially disrupt the transfer function. While the test environment may not have been conducive to observing the beneficial effects of the shield, it also did not reveal any adverse effects.

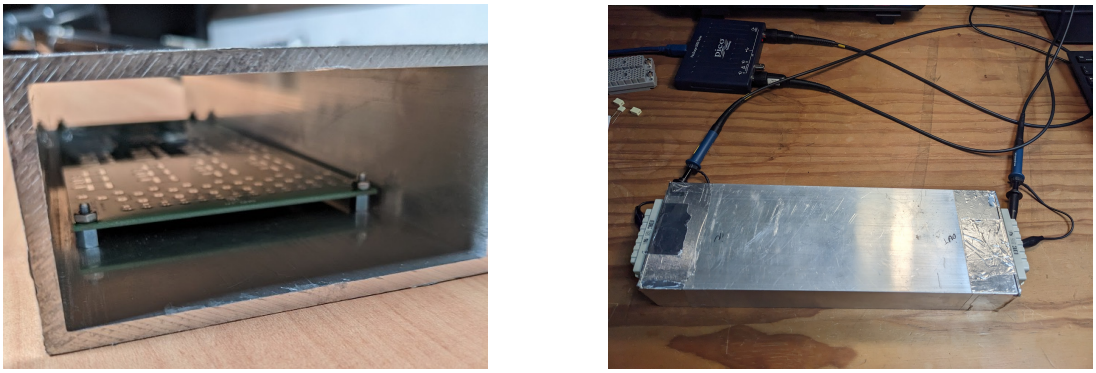

(a) (b)

Figure 3.17: Shielded filter board

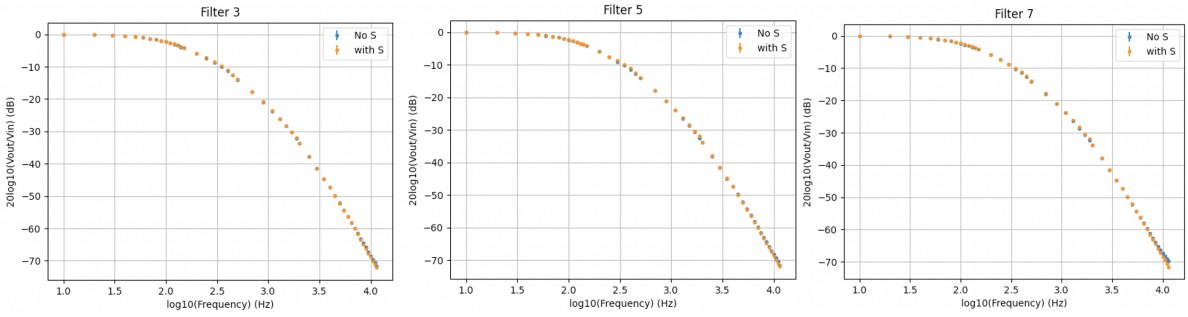

Figure 3.18: Transfer characteristics of filters 3, 5, and 7 compared between configurations with the filter board unshielded and with the filter board shielded

3.5 High Voltage Transfer Curve

To comprehensively evaluate the filter's performance under realistic conditions, it is essential to conduct studies that closely mimic the actual operational scenario. Up until now, the studies, specifically the transfer curve analysis, have been conducted using low voltage, where the only signal passing through the filters was the noise waveform itself. Although theoretically, DC voltage through the filter should not significantly impact the transfer curve or the filter's performance, it remains crucial to investigate the transfer characteristics under high DC voltage conditions, closely approximating its future operational state. For this purpose, the power supply utilized during the study matches the one that will be employed in the final operational environment with the filter.

This study requires a different approach compared to the low voltage measurements. To inject the noise wave together with the DC voltage and perform measurements, it is necessary to decouple systems. The PicoScope is not designed to withstand high voltages. Consequently, the PicoScope needs to be decoupled from the high voltage source. To achieve this, the schematic presented in Figure 3.19 was developed and implemented.

In the provided schematic, we can observe the filter with its CM noise capacitors, a power supply V2 representing the PicoScope's AWG, a floating power supply V1 operating in differential mode, and the PicoScope decoupled from them using capacitors C5 and C6. Capacitor C6 forms a high-pass filter with R3, the input resistance of the measuring device. To minimize interference with lower frequencies during measurements, we aim to have C6 with the highest possible capacitance value, as the cutoff frequency of such filters is inversely proportional to the RC time constant. A high RC value helps achieve the desired low cutoff frequency. Thus, with a large capacitance of $1\mu F$ for C6, the cutoff frequency of the high-pass filter is very low ($0,1592\ Hz$), ensuring minimal impact on the measured transfer curve within the frequency range of interest.

Similarly, for C5, it forms an unavoidable high-pass filter with the output resistance of the high-voltage power supply. The objective remains the same – to achieve a low cutoff frequency for this filter as well. To achieve this, R4 is added as described earlier, with the intention of keeping the RC value as high as possible.

This low cutoff frequency is desirable for both filters because, as mentioned earlier, the maximum voltage of the PicoScope's AWG is 2V. We want the output signal to be as high as possible to ensure reliable measurements. If the cutoff frequency were higher, these high-pass filters could attenuate and reduce the amplitude of waves with lower frequencies to a point that

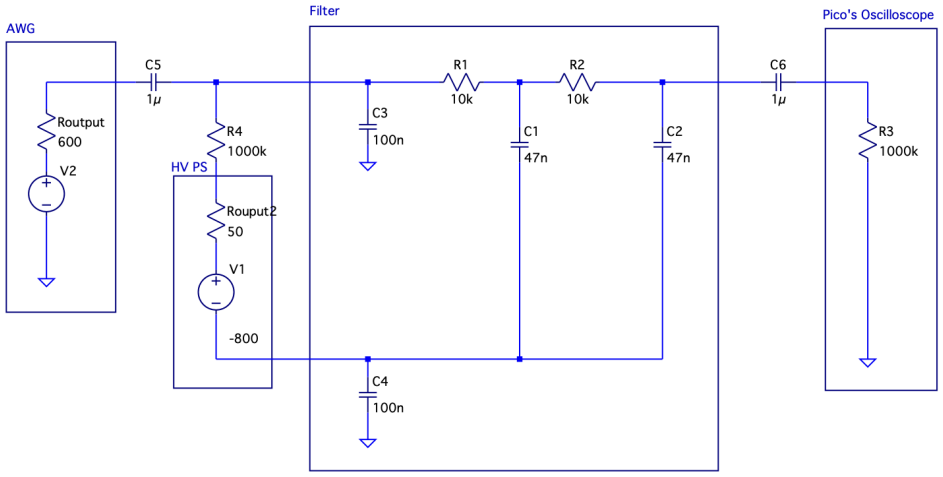

Figure 3.19: Schematic of the experimental setup used to investigate and obtain the transfer function of the filter under high DC voltage conditions

it would be difficult to read the signals accurately. Hence, we prefer the low cutoff frequency to preserve the signal amplitude as much as possible.

The values for C5 (1 μF), C6 (1 μF), and R4 (1 $M\Omega$) were chosen to be as high as possible for optimal performance. However, there is a point of diminishing returns where further increases would not significantly improve the results. Additionally, using larger capacitors capable of withstanding high voltages can be costly, so a practical balance was struck to ensure effective performance without excessive expenses. The selected values were considered sufficient for the circuit's purpose. It should be duly noted that in practical implementation, special attention must be given to the selection of components. As mentioned earlier, the chosen capacitors, C5 and C6, must be capable of withstanding high voltages, and resistor R4 should be capable of handling a power of approximately 1.5 W.

The software used to obtain the transfer curve in this study remains consistent with the one described in the diagram of Figure 3.5. The setup used to make the high voltage measurements is presented in figure 3.20. The transfer curve was determined for different voltage levels, and the results are depicted in Figure 3.21. Surprisingly, the transfer curve appears to vary with the applied voltage, and the filter's performance seems to deteriorate at higher voltage values. Furthermore, the error bars indicate that values below approximately -40 dB have significant uncertainty, suggesting caution in trusting the accuracy of measurements in this range. Additionally, the predicted curve obtained through simulation can be observed in the plot.

Upon encountering this surprising result, it became crucial to investigate and identify its source. To eliminate the power supply as a potential cause, the test was repeated using a

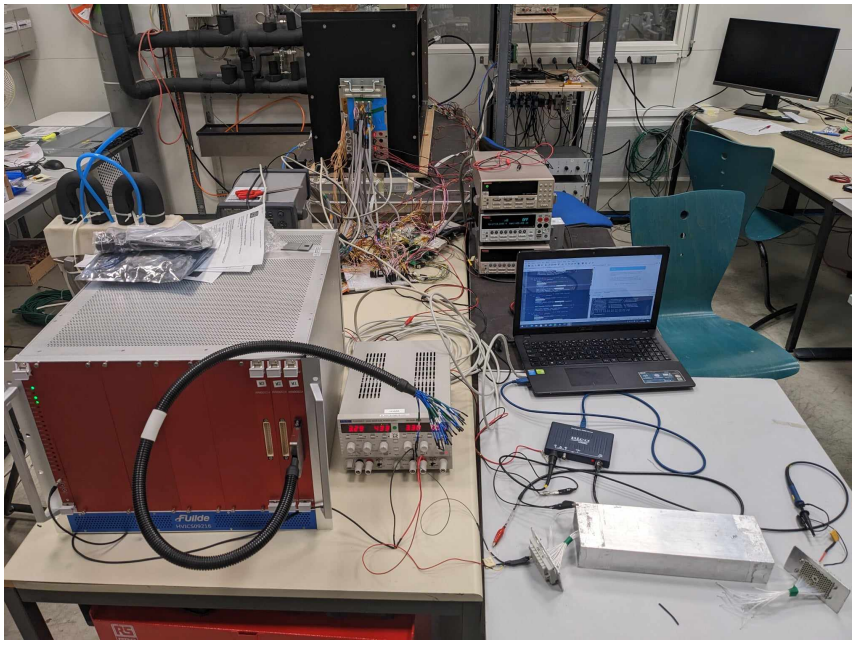

Figure 3.20: Setup used to make the high voltage measurements

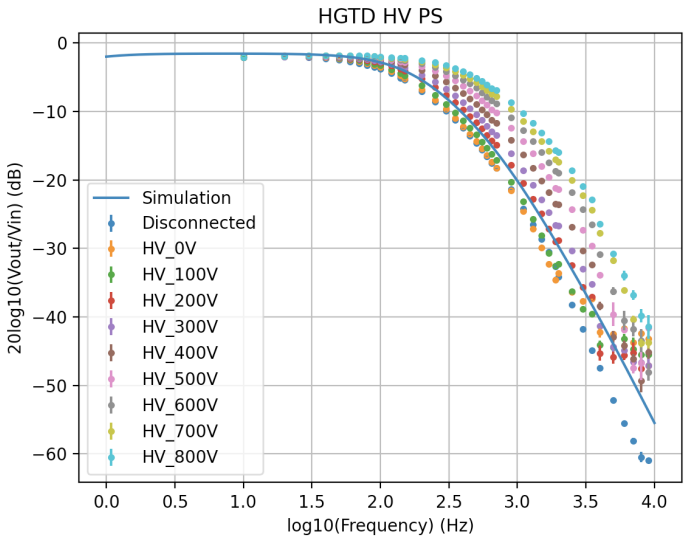

Figure 3.21: Results of transfer curve measurements conducted using the schematic depicted in Figure 3.19, with comparisons made between plots for various voltage levels and the simulation results obtained from the previously mentioned schematic.

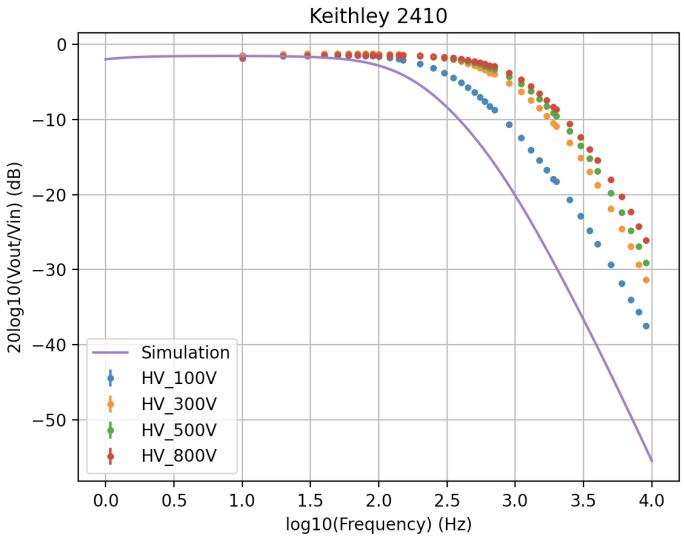

Figure 3.22: Outcomes of the transfer curve measurements carried out at different voltage levels utilizing the schematic illustrated in Figure 3.19, employing the Keythley 2410 High Voltage Power Supply for the experiments.

different power supply (Keithley 2410[28]), and the phenomenon persisted (fig. 3.22), although different curves were obtained for the same voltage levels (fig. 3.23) , which was unexpected.

To further investigate, the test was conducted with a grounded power supply, ruling out the possibility of the floating power supply being the cause (fig. 3.24).

To eliminate any potential issues with the channel or board used, further tests were conducted on different channels (fig.3.25) and boards, including an older board with no decoupling capacitors (fig. 3.26). However, the observed effect persisted across all these different setups.

In order to rule out the possibility that the observed phenomenon was influenced by the PicoScope, a similar experiment was conducted utilizing an oscilloscope (Tektronix TDS3032B [11]) and a function generator (TTi TG5011[12]). The procedure involved manually plotting a curve by traversing frequencies and recording the corresponding values. The outcomes are depicted in Figure 3.27, affirming the persistence of the observed phenomenon.

To investigate the hypothesis that component values might exhibit changes with varying applied voltage, an analysis was conducted on the components datasheet. Specifically, upon examining the capacitors' datasheet [29] [30], it became apparent that they do not follow a linear DC bias behavior. The datasheet revealed that the capacitor's value diminishes at higher voltages. Notably, the capacitance change with reference to +25 °C and 0 V is indicated as 15 percent, implying that the capacitors could experience a decrease of up to 15 percent at elevated voltages.

To test this hypothesis, a simulation was executed with the capacitors' values reduced by

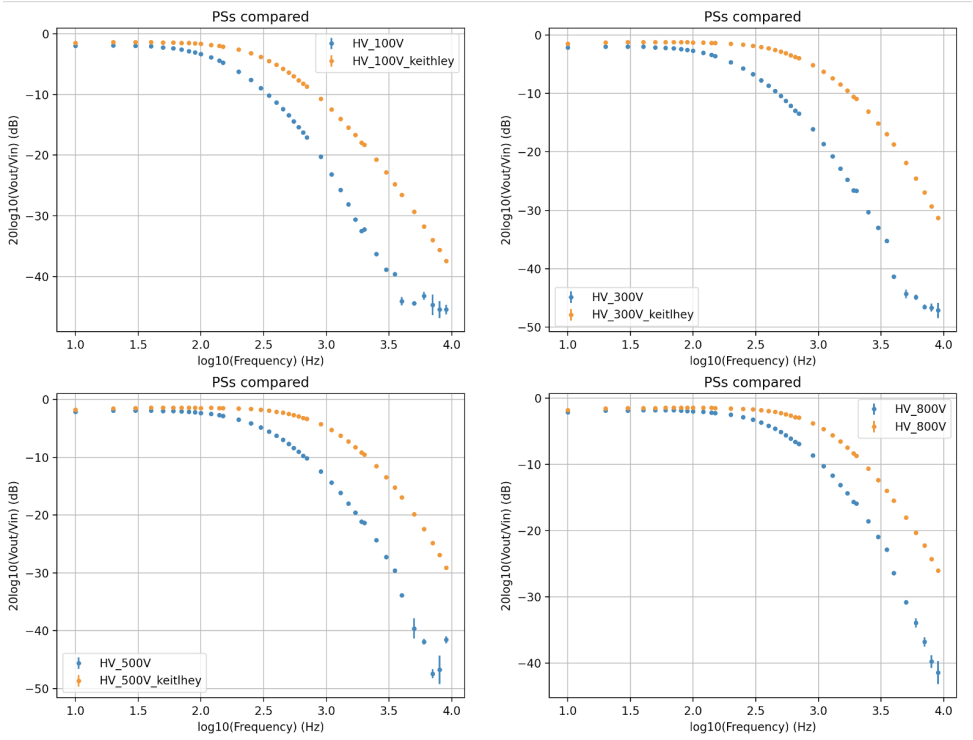

Figure 3.23: Transfer curves obtained with different Power Supplies compared at different voltage levels

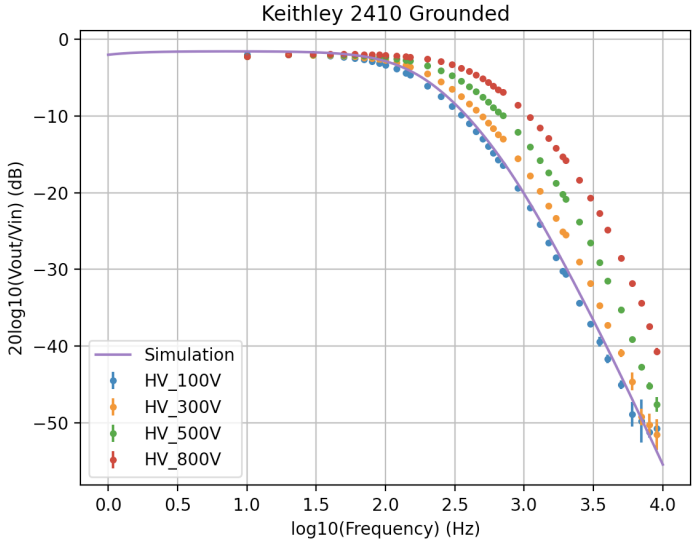

Figure 3.24: Transfer curves obtained at different voltage levels using the Keythley 2410 High Voltage Power Supply grounded

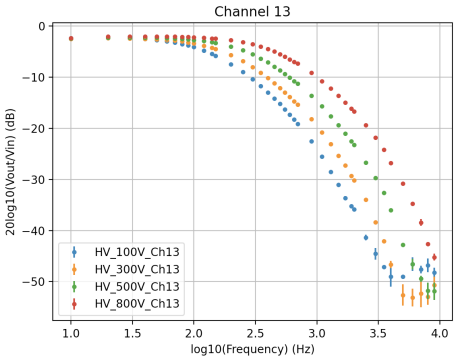

Figure 3.25: Transfer Function at different voltage levels using a different channel

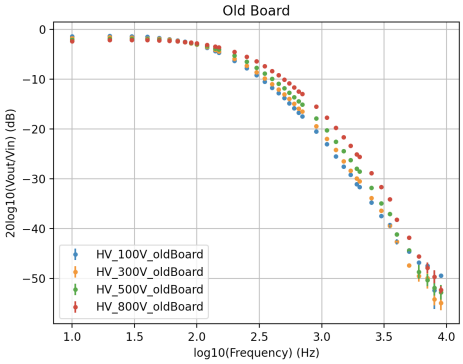

Figure 3.26: Transfer Function at different voltage levels using an older board with no decoupling capacitors

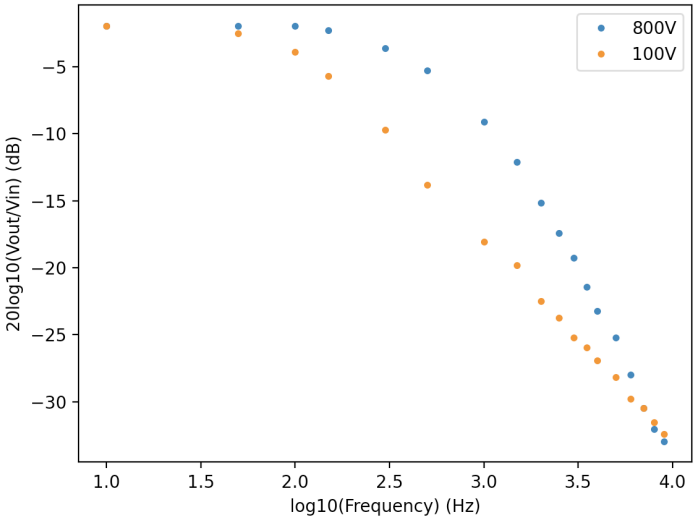

Figure 3.27: Transfer curves obtained at different voltage levels using the High Voltage Power Supply, osciloscope and function generator

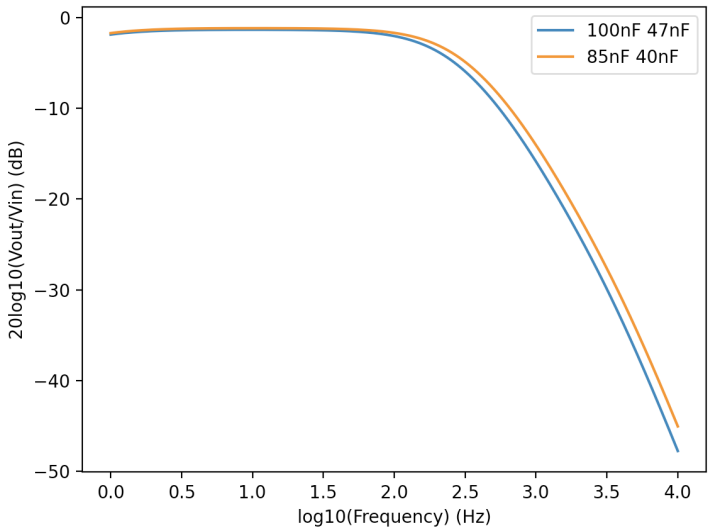

Figure 3.28: Transfer curves obtained through simulation using the schematic depicted in Figure 3.19 with the original capacitor values compared to those with the capacitor values reduced by 15%.

15 percent, and the resulting plots are displayed in Figure 3.28. Although this might partially account for the observed phenomenon, the impact does not appear to be as pronounced in simulation as it is in reality. Furthermore, it does not provide an explanation for the variations in transfer curves obtained from different power supplies despite the application of the same voltage. Another plausible explanation could involve variations in active components within the power supply, leading to fluctuations in the transfer curve. The complexity of the system and the interaction of multiple components might be introducing unanticipated influences on the measurements. Additional investigation and analysis are necessary to fully understand the underlying factors contributing to this unanticipated behavior.

3.6 Ripple attenuation measurement

Subsequently, despite the aforementioned results, the focus shifted towards examining the waveform generated by the power supply, which is intended for use in the final system. The objective was to assess the type and magnitude of ripple present in the supply and how the filter influenced it, if at all. Ripple constitutes a known noise source, making it crucial to understand its interaction with the filter. Hence, the voltage from the power supply was observed both with and without the filter, and the outcomes were compared.

It is crucial to emphasize that the PicoScope cannot withstand high voltages. Therefore, to obtain reliable results, it is necessary to decouple it from the high voltage source during measurements. This decoupling is achieved using the same 1uF capacitors as depicted in the

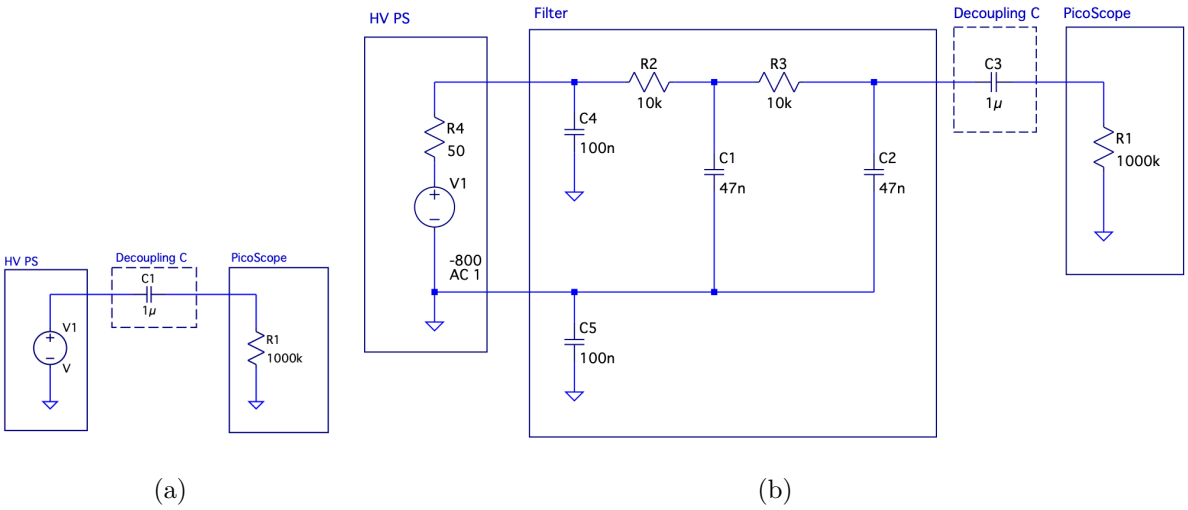

(a) (b)

Figure 3.29: Schematics representing the ripple measuring process without filter (a) and with filter (b)

schematics of Figures 3.29a and 3.29b.

The measurements conducted aimed to observe the high voltage waveform in the time domain and its FFT (Fast Fourier Transform) representation to analyze the ripple and understand the filter's impact on it. Measurements were performed with and without the filter, and with the power supply grounded, considering different power supply channels but for the same filter channel. All measurements were done at a voltage of 900V.

For instance, one power supply channel was examined, and the unfiltered voltage waveform with the grounded power supply displayed spikes corresponding to the ripple, with peak-to-peak amplitudes of approximately 160 mV (Fig. 3.30a). With the filter in place, the plots exhibited different behavior. The peak-to-peak amplitude of the large ripple peaks decreased to approximately 23 mV (Fig. 3.30b).

Analyzing the Fast Fourier Transform (FFT) of the signal around the ripple frequency range, as demonstrated in Figure 3.31, unveiled distinct peaks at approximately 300kHz, corresponding to the ripple frequency. Upon expanding the analysis to cover the entire frequency range (Fig. 3.32), rather than solely focusing on the ripple frequencies, multiple peaks at different frequencies, including higher ones, were observed. Remarkably, these peaks largely retained their characteristic shape despite the presence of the filter. However, upon closer scrutiny, it became apparent that the overall magnitudes of these peaks had all decreased uniformly. The FFT's general shape remained intact but exhibited a reduction in amplitude. This consistent attenuation of frequencies demonstrates the filter's effectiveness in reducing noise. This assertion is further substantiated by the noticeable decrease in amplitude of the previously mentioned ripple

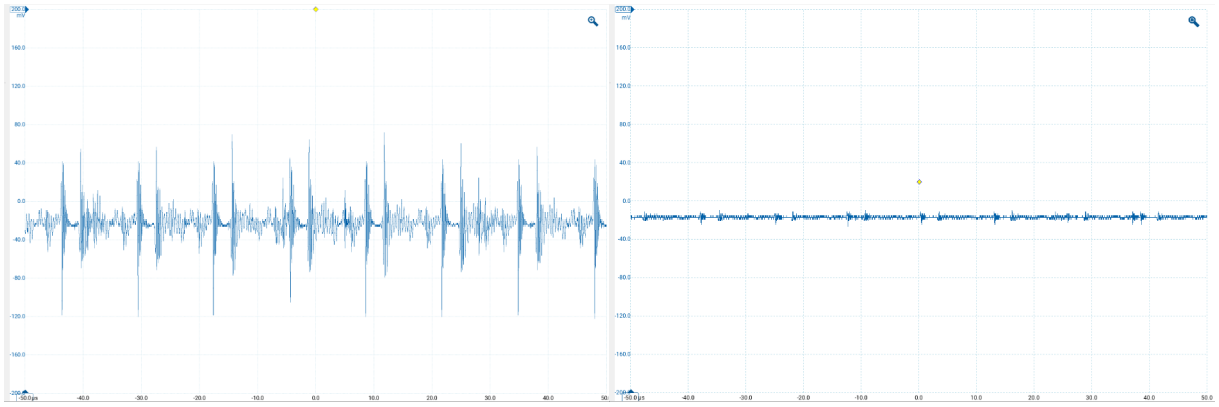

(a) (b)

Figure 3.30: Plots depicting the waveform of the high voltage power supply channel 1, measured both with (a) and without (b) the filter.

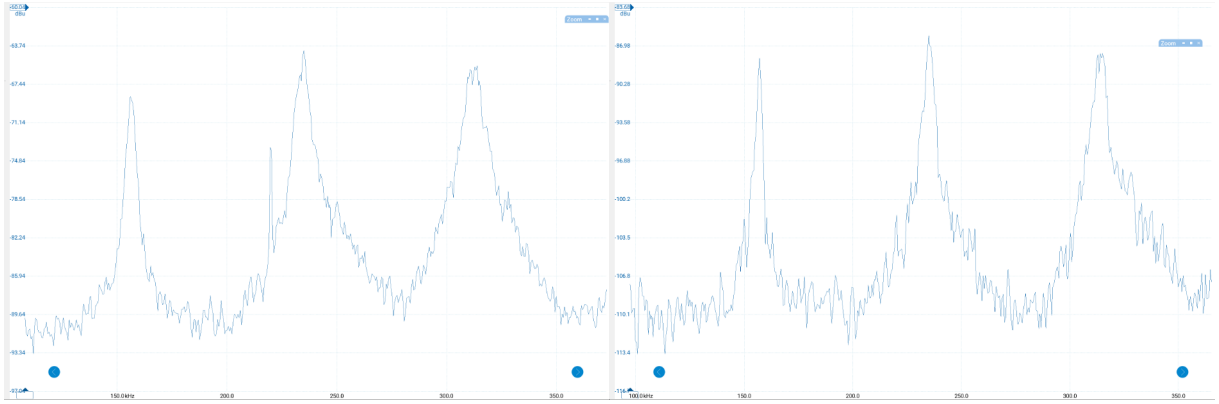

(a) (b)

Figure 3.31: FFT depiction of the waveforms from Figure 3.30, centered around the ripple frequency range. Figure (a) illustrates the scenario without the filter, while Figure (b) depicts the situation with the filter.

peaks, underscoring the filter's capacity to suppress noise across a spectrum of frequencies.

All available power supply channels were subjected to testing using the same channel 1 from the board. These tests provided data that was used to create a table, similar to Table 3.1, containing the values before and after the filter's attenuation. This table provided a better understanding of the level of attenuation achieved, and the level of ripple expected from the power supply. The complete table is available for reference in Appendix A (Table A.1).

From these values, we determined that with the power supply grounded, the average attenuation is approximately $-20\ dB$. Notably, $-20\ dB$ represents the attenuation at a frequency around 300kHz. When comparing these measured attenuations to the theoretical value of attenuation predicted by the current theoretical model, which is $-120\ dB$, a significant discrepancy is

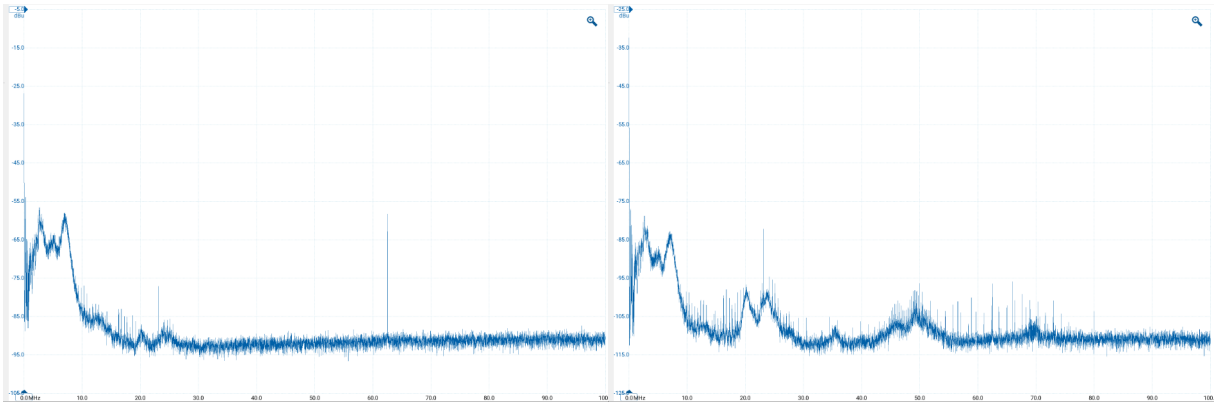

(a) (b)

Figure 3.32: FFT representation of the waveforms from Figure 3.30, covering the entire measurable frequency range. Figure (a) illustrates the scenario without the filter, while Figure (b) depicts the situation with the filter.

evident. The attenuation is much lower than the theoretical prediction, indicating a substantial deviation from the expected values.

		Max pkpk (mV)	Attenuation(dB)
Ch1	Without	∼160	-22,49877473
	With	∼12	
Ch2	Without	∼160	-22,49877473
	With	∼12	
Ch3	Without	∼190	-25,57507202
	With	∼170	
Ch4	Without	∼35	-13,72761754
	Depois	∼15	

Table 3.1: A table providing a summary of the outcomes derived from measuring the HV power supply output waveform both with and without the filter, displaying the attenuation levels. Please note that this table is a partial representation, as a total of two modules, each comprising 14 channels, were subjected to testing.

3.7 Cross Talk and higher frequency transfer curves

Examining cross talk was a significant aspect of the testing process, as noise induced in one channel by neighboring channels can severely compromise the filter's performance.

In order to assess cross talk, the method involved injecting a signal into one channel and then examining the output of an adjacent channel to detect any unintended signals. Given that the PicoScope's AWG is constrained to a maximum amplitude of 2 V, this procedure was conducted using both an oscilloscope and a tabletop function generator. The frequency range was traversed with a sine wave with an amplitude of 10 V to determine if neighboring channels output registered any signals.

The observations revealed that when a specific frequency was reached, the neighboring channel's output began to capture the injected signal, albeit with some attenuation. As the frequency continued to rise, the amplitude of the acquired signal also increased, eventually reaching a peak and subsequently diminishing until it became negligible once again. This pattern resembled the characteristics of a passband filter, manifesting itself around frequencies of approximately 300kHz and becoming more pronounced at approximately 25 MHz.

The process was repeated for channels located progressively farther away on the board, and the phenomenon persisted. Surprisingly, the strength of the induced signal in neighboring channels did not appear to correlate with their proximity to the input signal. This is unusual behavior for typical cross talk. Further investigation involved examining different sections of

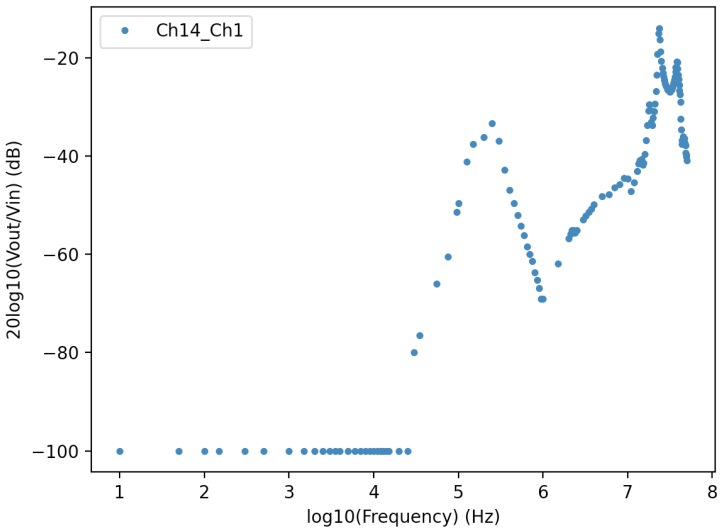

Figure 3.33: Transfer function determined by introducing a signal into channel 1 and monitoring the output from channel 14. It should be noted that for frequencies below a certain threshold (30 kHz), the signal amplitude was insufficient for reliable detection.

the board. It was discovered that the signal was actually propagating through the board's backplane, which serves as the grounding system. This suggests that the observed phenomenon deviates from the expected behavior of conventional cross talk. Rather than being a result of signal interference, it appears to involve direct signal propagation between channels.

To investigate this phenomenon, a similar approach was employed using an oscilloscope[11] and a function generator[12] as described in section 3.5. The process entailed manually plotting a curve by sweeping through frequencies and recording the corresponding measurements. However, in this case, the input signal was fed into the first channel while the output signal was measured on channel 14. The resulting transfer curve is depicted in figure 3.33.

This unexpected outcome prompted a more thorough examination of the transfer curve for higher frequencies. Hence, transfer curves were manually generated for both low and high voltage scenarios using the same point-to-point method as previously explained, thereby extending the measurement range up to 50 MHz. The outcomes are illustrated in figure 3.34a and figure 3.34b. Notably, both transfer curves exhibit unexpected peaks at higher frequencies. These peaks raise concerns, as they suggest that the filter might not effectively attenuate these frequencies as expected.

The transfer function for higher frequencies had not been tested yet due to the reasons outlined in subsection 3.2.1. To reiterate, the values obtained for frequencies arround 10 kHz were impractically small and difficult to interpret, and there was no logical basis to anticipate the presence of a pass band at higher frequencies.

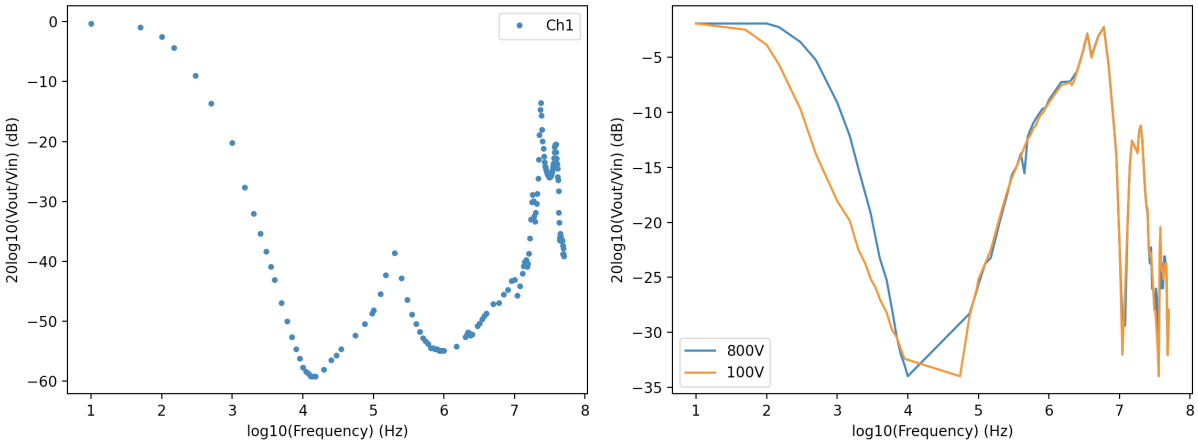

(a) (b)

Figure 3.34: Transfer function of channel 1 in the filter manually measured employing an oscilloscope and function generator for both low voltage (a) and high voltage (b) scenarios. Measurements extended up to higher frequencies, approximately 50 MHz.

3.8 Common mode (CM) noise

Taking into consideration these unforeseen outcomes at higher frequencies, the filter's ability to attenuate common mode noise was also examined at elevated frequency levels. Using the configuration depicted in Figure 3.2, the testing procedure was conducted employing the oscilloscope and function generator as previously described.The anticipated outcome was a relatively consistent line hovering around -60 dB across all frequencies. However, the obtained result, depicted in figure 3.35, revealed that the expected steady line persisted only until approximately 1 MHz, beyond which a discernible peak emerged. This peak resembles the patterns observed in our other high-frequency tests.An interesting observation is that, unlike the transfer function which was also tested with high voltage, the common mode noise transfer function appears to be unaffected by higher voltages.

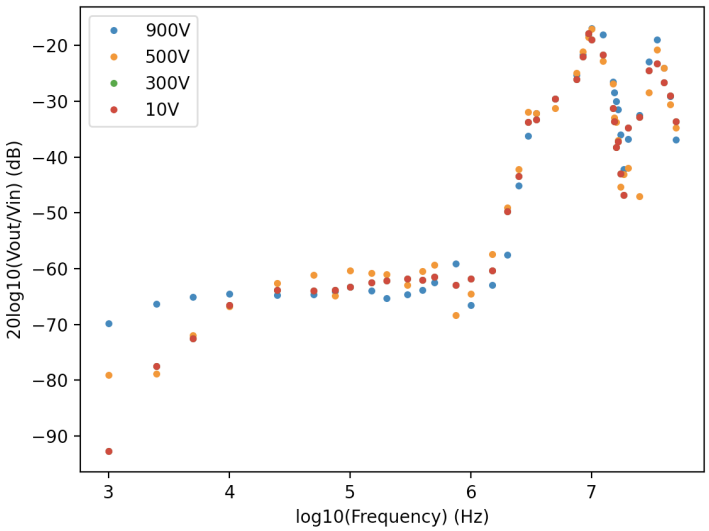

Figure 3.35: Common mode noise transfer function manually measured employing an oscilloscope and function generator for various voltage levels. Measurements extended up to 50 MHz.

3.9 Leakage Current

Leakage current refers to the small, unintended flow of electric current in a component or material that should ideally have no current passing through it. It occurs when there is a path for current to flow, even though the component or material is not supposed to conduct electricity under normal conditions. The assessment of leakage current is a requirement and factor that demands attention. To assess the board's leakage current, a test was formulated. In this setup, one of the channels was connected to a high-voltage supply, with all other channels, including the output ones, disconnected. Subsequently, the current supplied by the source was monitored and recorded.

During the initial testing phase, a keythley HV power supply [28] was employed, yielding results indicating a leakage current of approximately 0.5 μA per channel when under a voltage of -900 V. This value exceeded the anticipated level. In an attempt to mitigate the leakage current, the board underwent a cleaning process involving ultrasound treatment in methanol. Subsequently, a highly resistant, insulating conformal coating (Urethane) was applied to certain channels, while others were safeguarded with plastic strips for protection. This procedure aimed to assess the impact of the coating on performance compared to clean channels. In this instance, a CAEN 471A Power Supply [31] was utilized to measure the input current into the board.

The measurements were conducted following a standardized 25-minute duration to ensure uniform charging of capacitors across all channels. The observed results indicate a significant reduction in leakage current to approximately 30 nA for channels with the applied coating. Con-

	I(nA) (+-1nA)	
Ch	900V	500V
1	33	4
3	42	5
5	35	5
7	35	4
9	34	4
11	36	5
13	31	5
2	33	4
4	35	4
6	36	4
8	34	5
10	32	4
12	23	4
14	24	3

Table 3.2: Leakage current measurements conducted for all the channels on the filter board, both at 500V and 900V.

versely, channels lacking the coating exhibited a slightly lower leakage current of approximately 25 nA. Despite this difference, the decision to sacrifice roughly 5 nA of leakage current in favor of the coating was deemed justified, primarily because the coating plays a role in preventing subsequent board contamination. These measurements pertain to tests conducted under a 900 V voltage condition. Table 3.2 provides a summary of the measurements conducted for both 900 V and 500 V voltage settings:

3.10 Explanatory Model

The conducted cross-talk tests, transfer curve tests, and common mode tests collectively exhibited unexpected outcomes that were contrary to our initial expectations, particularly concerning the unexplained peaks observed at higher frequencies. These tests clearly demonstrated that the existing theoretical model was inadequate and failed to predict the observed outcomes accurately. It became apparent that an improved and upgraded model was required, one that could provide explanations and predictions for the observed results.

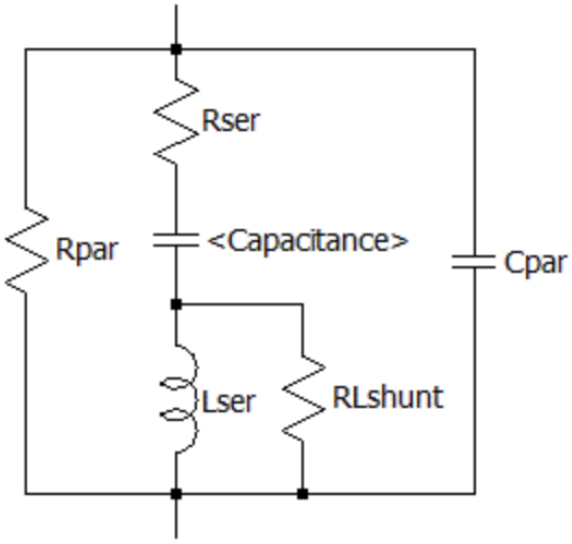

Figure 3.36: Capacitor parasitic model[10]

The primary objective of this model was to effectively provide a comprehensive explanation for the observed outcomes across the aforementioned tests. The existing disparity between the simulation model and the actual experimental results, particularly notable at higher frequencies, may potentially be associated with the influence of parasitic values. Thus, we initiated the process of integrating parasitic values into the current model to evaluate whether such adjustments could lead to a more accurate representation of our observed outcomes.

The model's incorporation of parasitic elements encompasses factors originating from various sources. Among these are inherent component parasitics, such as the capacitors integrated into the board. A more accurate representation of these capacitors can be achieved by employing a parasitic model, illustrated in Figure 3.36. Although specific parasitic values are absent from the capacitors' datasheets, their impedance characteristics predominantly depend on equivalent series resistance (ESR) and equivalent series inductance (ESL). In the absence of specific values, common values for ESR and ESL for these capacitor types (3 $m\Omega$ and 0.75 nF) were utilized.

Moreover, parasitics inherent to the board itself were integrated into the model. This encompassed parameters such as trace resistance, trace inductance, and capacitance between traces. It's important to note that we did not find it necessary to heavily consider the impact of capacitance between different layers of the circuit board, as this likely wouldn't be significant due to the existing connection through the decoupling capacitors. Similarly, we did not give significant attention to the impact of parasitic inductance in the vias, as this is already partly accounted for in the model of the capacitors. Given that the board comprises 14 channels, we needed to account for the interactions between them as a whole. Consequently, the simulation encompassed the entire board rather than individual channels.

One plausible explanation for signal propagation through the backplane involved the presence of resistance between the backplane and ground, collaborating with the decoupling capacitors to generate a high-pass filter effect. Consequently, the backplane ceased to function as an ideal ground. The emergence of a signal peak's behavior could be attributed to the presence of an inductance within the system, resembling the principles of an RLC circuit. This inductance could contribute to the observed bandpass-like attributes. Hence, the resistance and inductance of the wire connecting the ground and the board's backplane were also factored into the model.

An additional aspect that demands attention is the presence of inherent parasitics associated with the probing and measurement equipment. This encompasses elements such as the input capacitances of the oscilloscope, the inductances of the probes, the compensation mechanism of these probes, and the tip capacitance of the probes themselves. The same consideration extends to the grounding wire of these probes, including both the inductance and tip capacitance of the grounding component.

Furthermore, we also accounted for the output resistance of both the PicoScope and function generator, along with the output resistance of the high voltage power supply in cases where it was employed. In addition to these factors, the inductance and resistance of the voltage wires were also incorporated into our analysis.

The model is expected to provide accurate descriptions of the scenarios previously mentioned, including the high-voltage transfer curve, the low-voltage curve, and the common mode noise attenuation curve. Ensuring that the model effectively predicts outcomes in all three scenarios is crucial for its robustness.

To further enhance the model and assist in identifying parasitic values within the probes, an additional scenario was introduced. Following a similar procedure as outlined in section 3.2.2, a schematic resembling the one depicted in Figure 3.8 was employed to generate a corresponding plot, shown in Figure 3.37. This scenario introduces another constraint on the model, aiding in its refinement and development.

Through an iterative trial-and-error approach, adjustments to the model's parameters can be systematically made to progressively align it more closely with the observed real-world results. This approach results in a model that faces challenges when attempting to effectively account for all scenarios using consistent parasitic component values. However, the models can be adjusted to better match each scenario by modifying the probe's parasitic characteristics. This standpoint is plausible, given the possibility of differing measurement setups between these instances. An alteration in probe configuration, like adding an extra loop, could result in a significant variance in probe inductance. To verify whether the probe's inductance was indeed

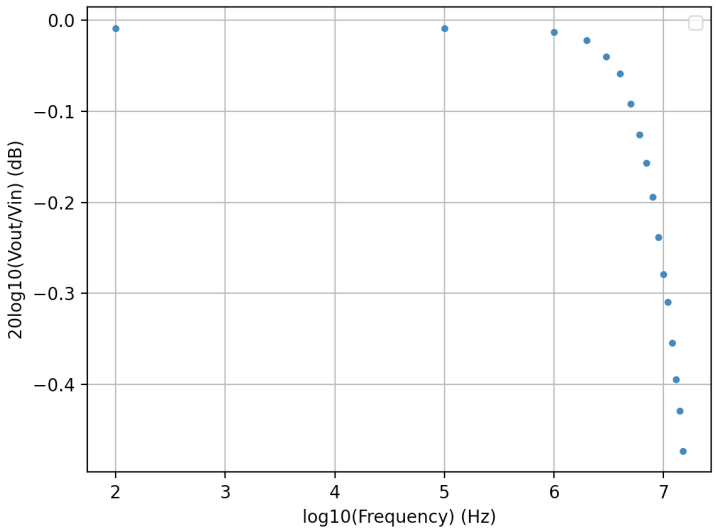

Figure 3.37: Results obtained using a setup similar to the one depicted in the schematic from Figure 3.8, utilizing diffent probes, oscilloscope [11], and function generators [12].

substantially influenced by its arrangement and whether it significantly affects the transfer curve, an experiment was devised. The transfer curve was measured using the PicoScope, first with the probe wires and ground wires kept as straight as possible (Fig. 3.39a), and then with them looped multiple times (Fig. 3.39b). This was done across the entire range of the PicoScope AWG, up to 1 MHz, to capture the first peak. The results revealed that different probe configurations do not notably affect the transfer curve (Fig. 3.38). Thus, the model should be capable of describing all scenarios without requiring changes in probe-related parasitic values.

Considering this constraint of maintaining constant scope parasitics across scenarios, an iterative process led to the development of a model. This model is a streamlined version of the one previously mentioned, with non-significant parasitics omitted. The retained parasitics are the major contributors to the observed outcomes. The model is depicted in Figures 3.40,3.41 and 3.42, the slightly varied schematics correspond to the different scenarios.

The parasitic values used in the model across all schematics are presented in table 3.3. I believe that most of these values fall within acceptable ranges, except for the tip capacitance of the probes. The values of 20 pF and 45 pF seem a bit higher than what is typically expected. Additionally, it's worth noting that there is a significant difference in the inductance values of the probes, with probe 2 having a relatively high inductance of approximately 420 nH. While the variation between probes could be attributed to the fact that they are different models, it is still unusual that probe 2 exhibits such a high inductance value.

The model's predictions for these varying schematics are represented in Figure 3.43.

The model's parameters were also assessed for their consistency with the data presented in

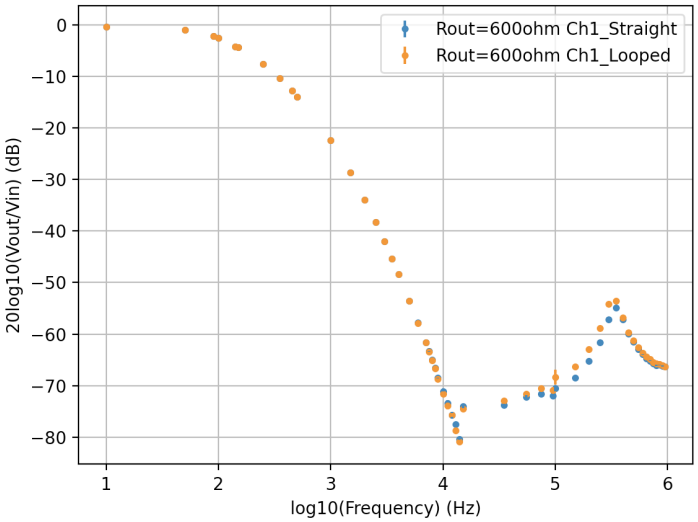

Figure 3.38: Comparison of transfer curves for a filter channel when probes and ground wires are either looped or straight.

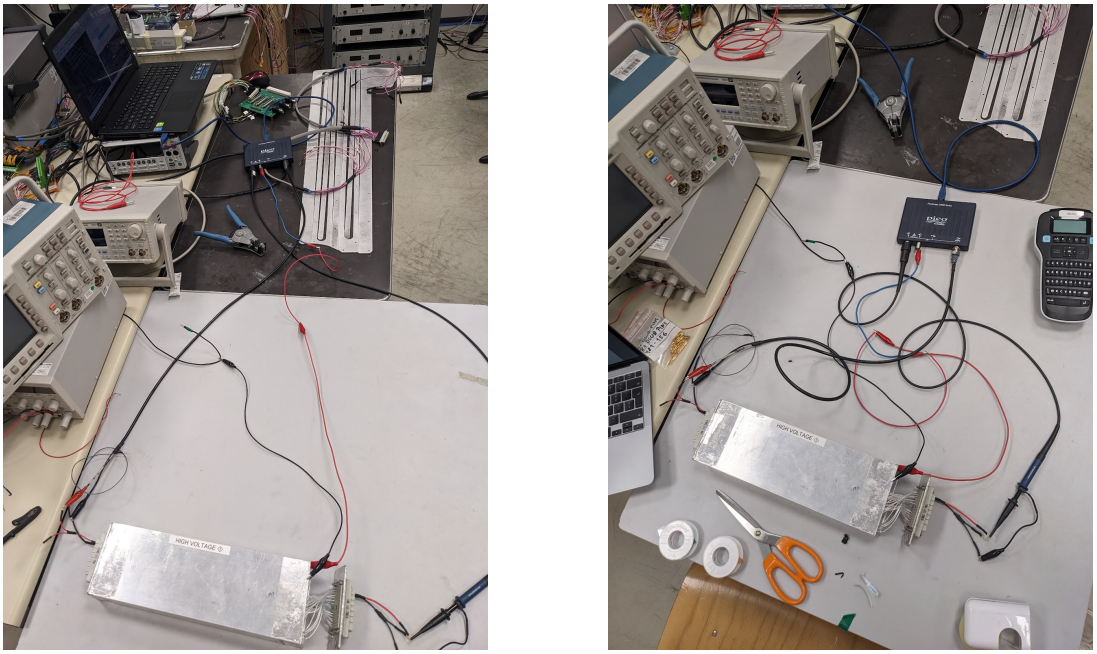

(a) (b)

Figure 3.39: Transfer curve measuring setup used for straight (a) and looped (b) probe results comparison

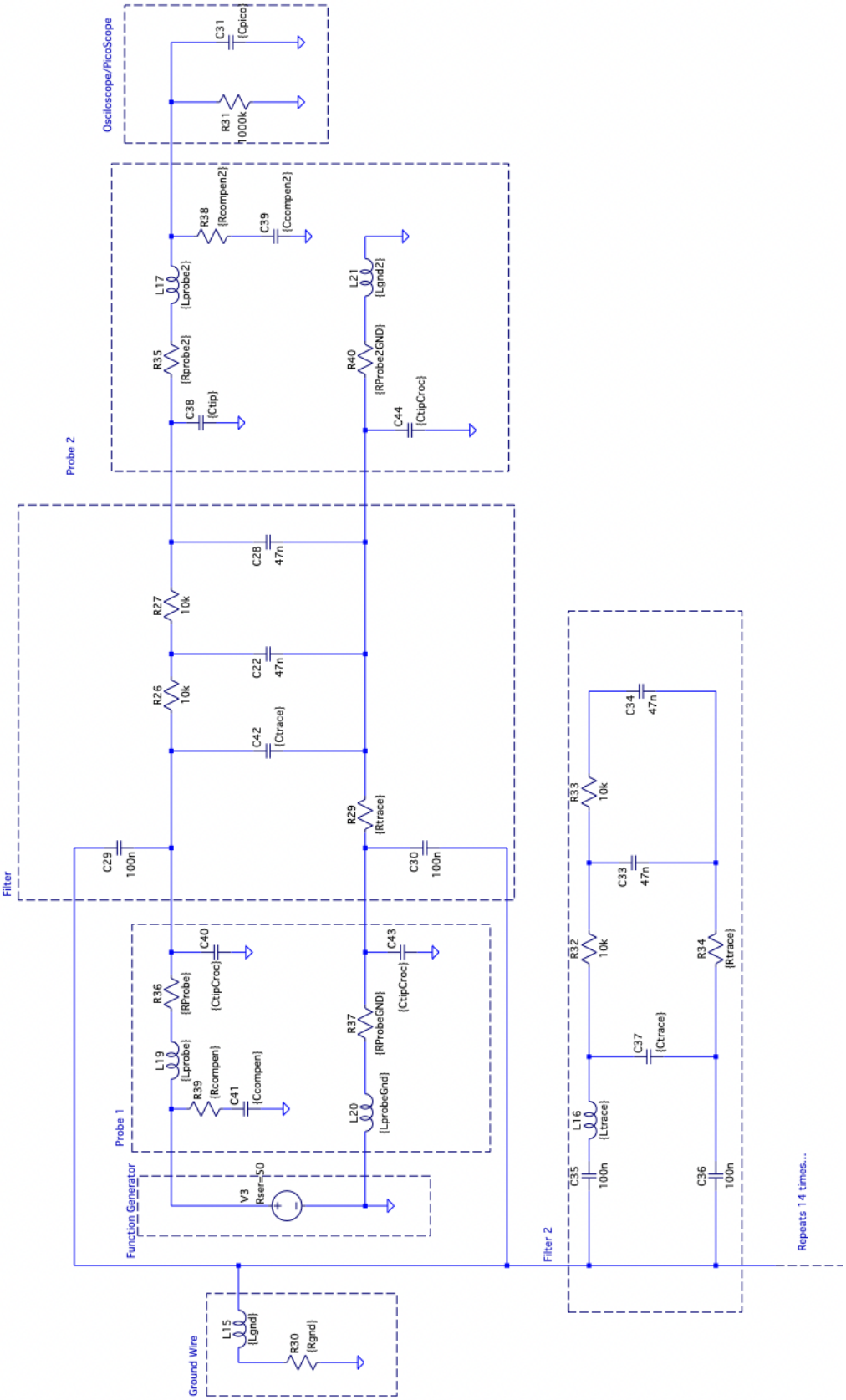

Figure 3.40: Full parasitic model of the low voltage transfer curve measuring schematic

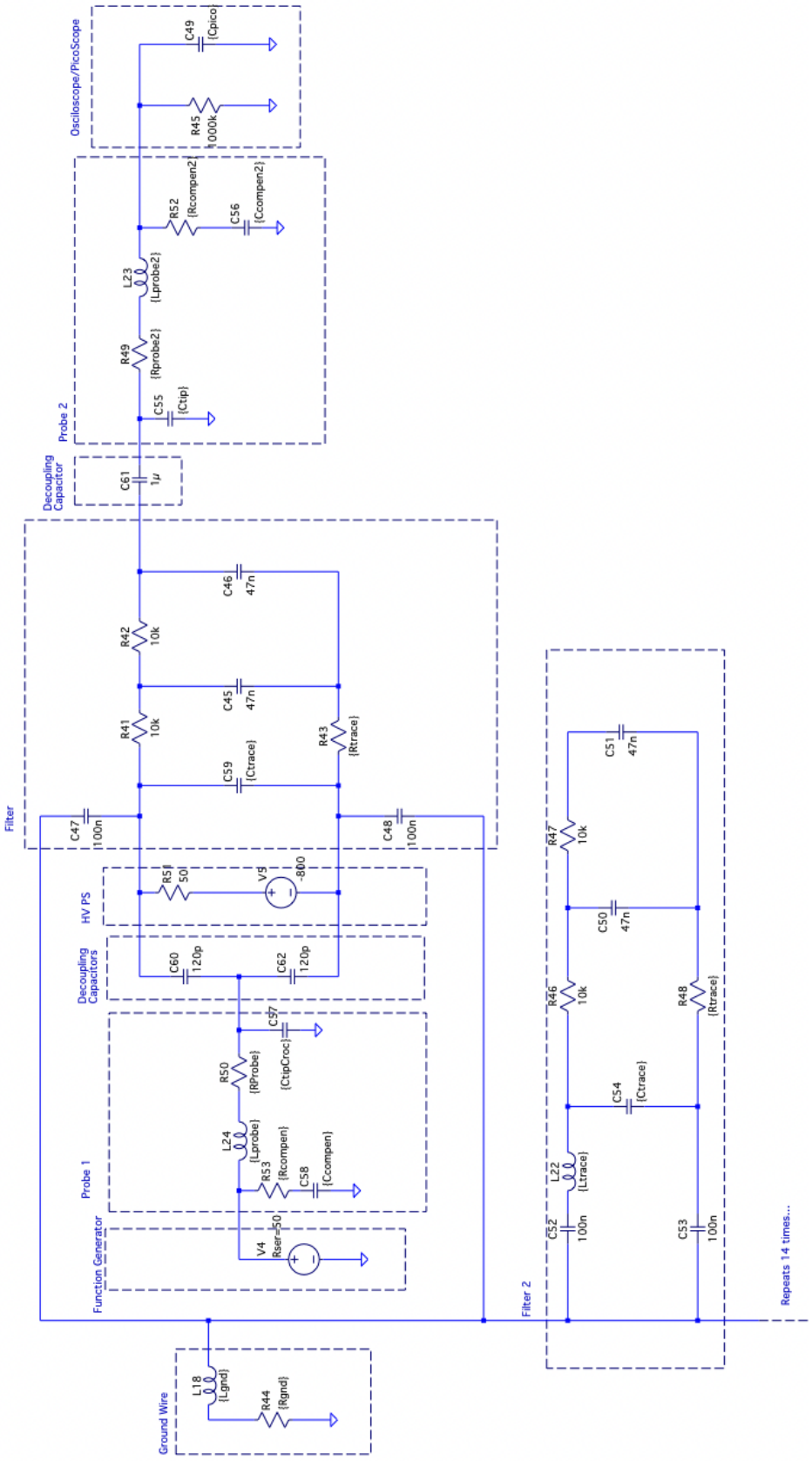

Figure 3.41: Full parasitic model of the common mode noise transfer curve measuring schematic

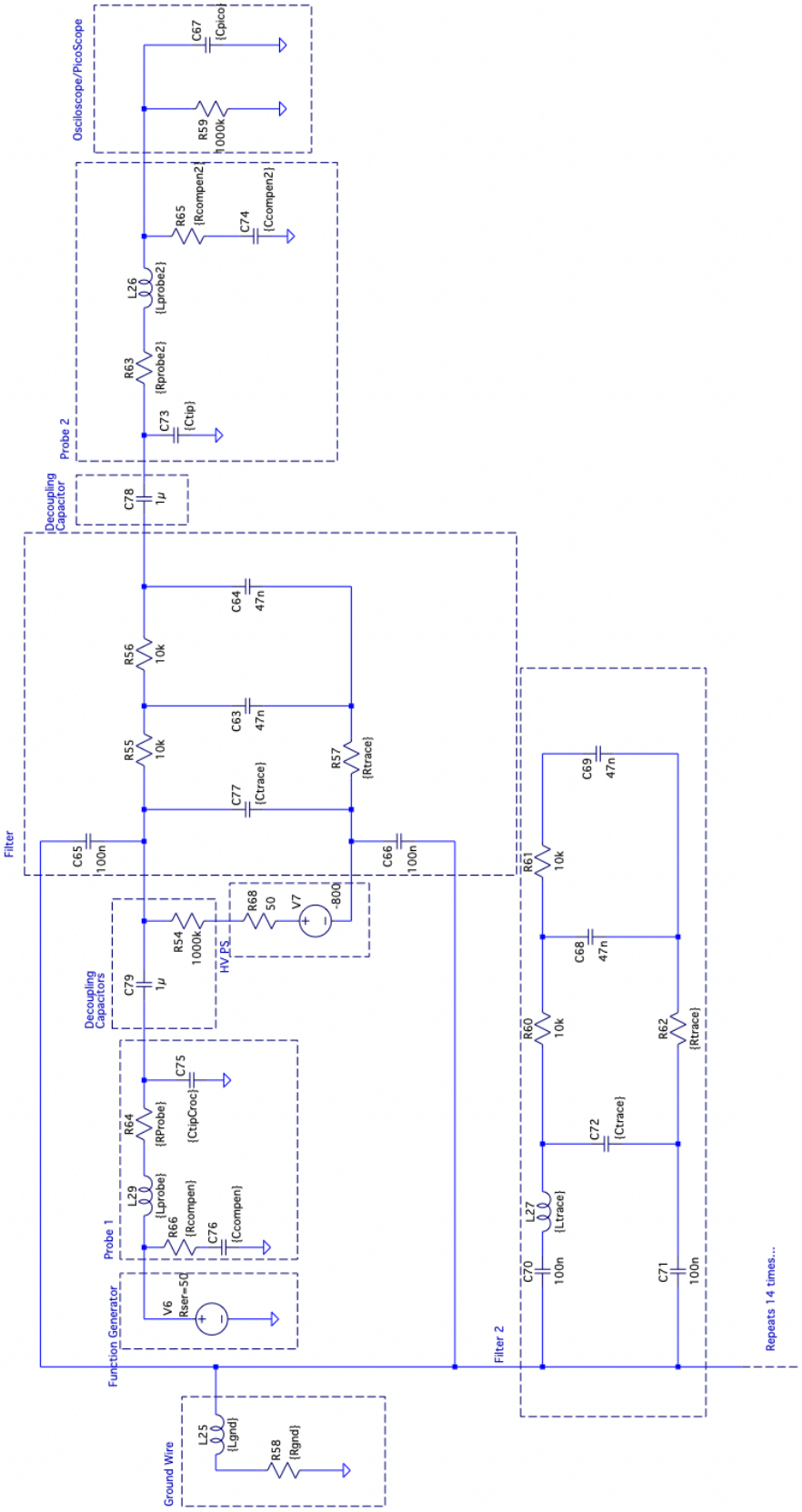

Figure 3.42: Full parasitic model of the high voltage transfer curve measuring schematic

Component	Value	Component	Value
Rgnd	800 $m\Omega$	Rtrace	400 $m\Omega$
Lgnd	1 μH	Ctrace	30 pF
Lprobe	5 nH	Lprobe2	420 nH
Rprobe	100 $m\Omega$	Rprobe2	15 Ω
Rcompen	1 Ω	Rcompen2	15 Ω
Ccompen	70 pF	Ccompen2	45 pF
CtipCroc	45 pF	LprobeGnd2	350 nH
LprobeGnd	30 nH	RProbeGND2	100 Ω
RProbeGND	100 $m\Omega$	Ctip	20 pF
CtipCroc	45 pF	Cpico	13 pF

Table 3.3: Table providing a summary of the values of parasitic components employed in the model

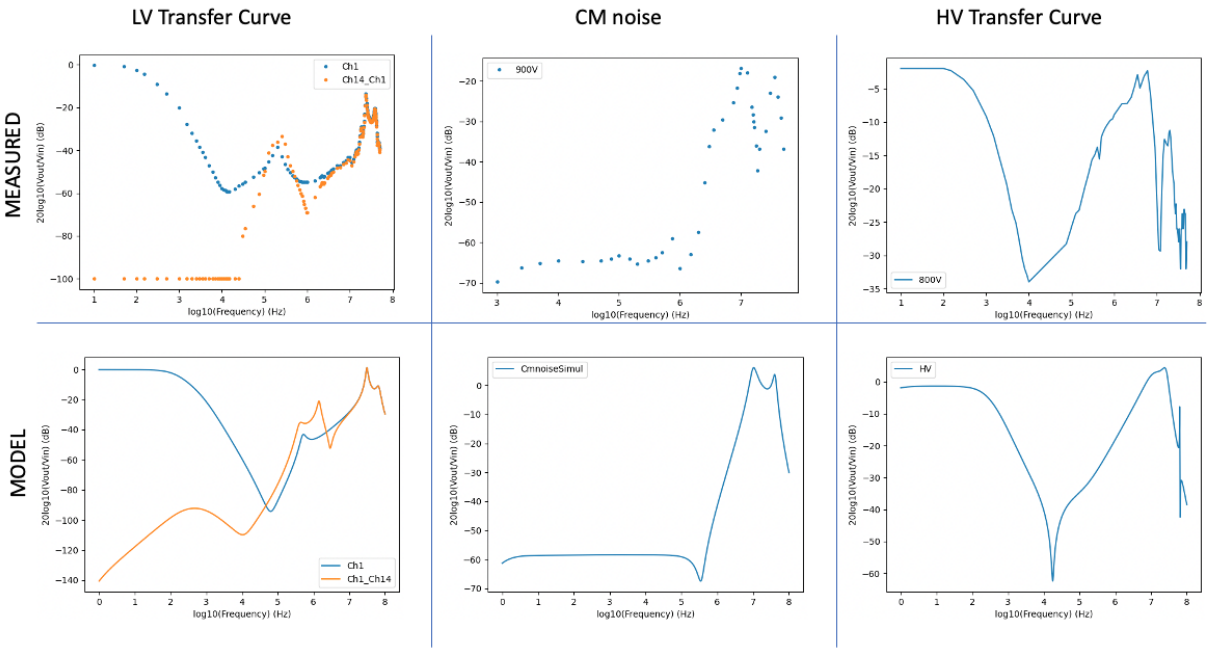

Figure 3.43: Model simulation results for the different scenarios

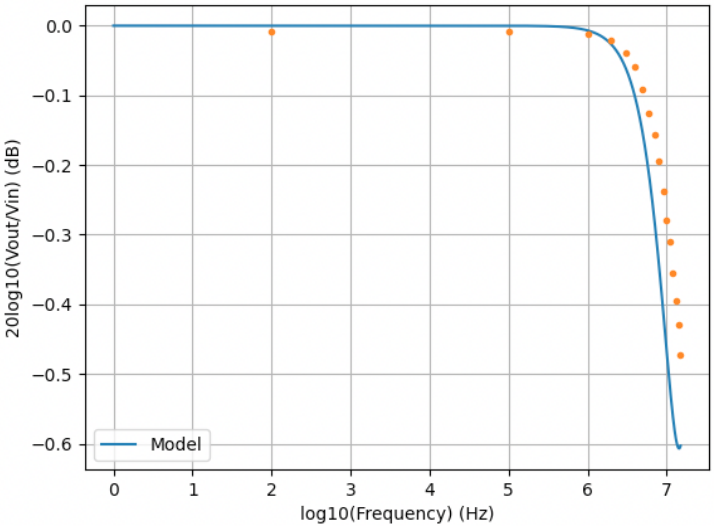

Figure 3.44: Model prediction of values presented in figure 3.37

Figure 3.37. Employing a schematic akin to that depicted in Figure 3.8, featuring the assigned parasitic values, we generated a plot that effectively aligns with the observations showcased (Figure 3.44).

The model's projected outcomes, juxtaposed with the recorded experimental data, are presented in Figure 3.43. A quick examination reveals that the general form of the transfer curves is reasonably retained from reality to simulation, albeit with some disparities. Upon closer scrutiny, it becomes evident that certain structures of the model's curves exhibit slight shifts in simulation, either vertically or horizontally, in relation to the real-world data. Nevertheless, the overall shape of the transfer curves is broadly preserved. In the process of constructing and refining this model, it became evident that the prominent peaks observed at higher frequencies in all scenarios are primarily associated with the parasitic characteristics of the probes and the grounding configuration.

It is evident looking at the model more carefully that it is not flawless, which is unsurprising given the complexities involved. While some of these deviations might potentially be reconciled through further parameter adjustments, achieving absolute congruence between the model and reality may not significantly enhance the insights gathered. The primary conclusion, namely that the prominent peaks observed at higher frequencies are likely attributable to the characteristics of the probes, remains robust. Therefore, the model effectively serves its purpose by identifying the sources of discrepancies and affirming that the anomalies are likely not solely rooted in the circuit board itself but rather arise from aspects related to the measuring equipment and grounding configuration.

Applying the model to the scenario of ripple measurements (Fig. 3.45) also provides an

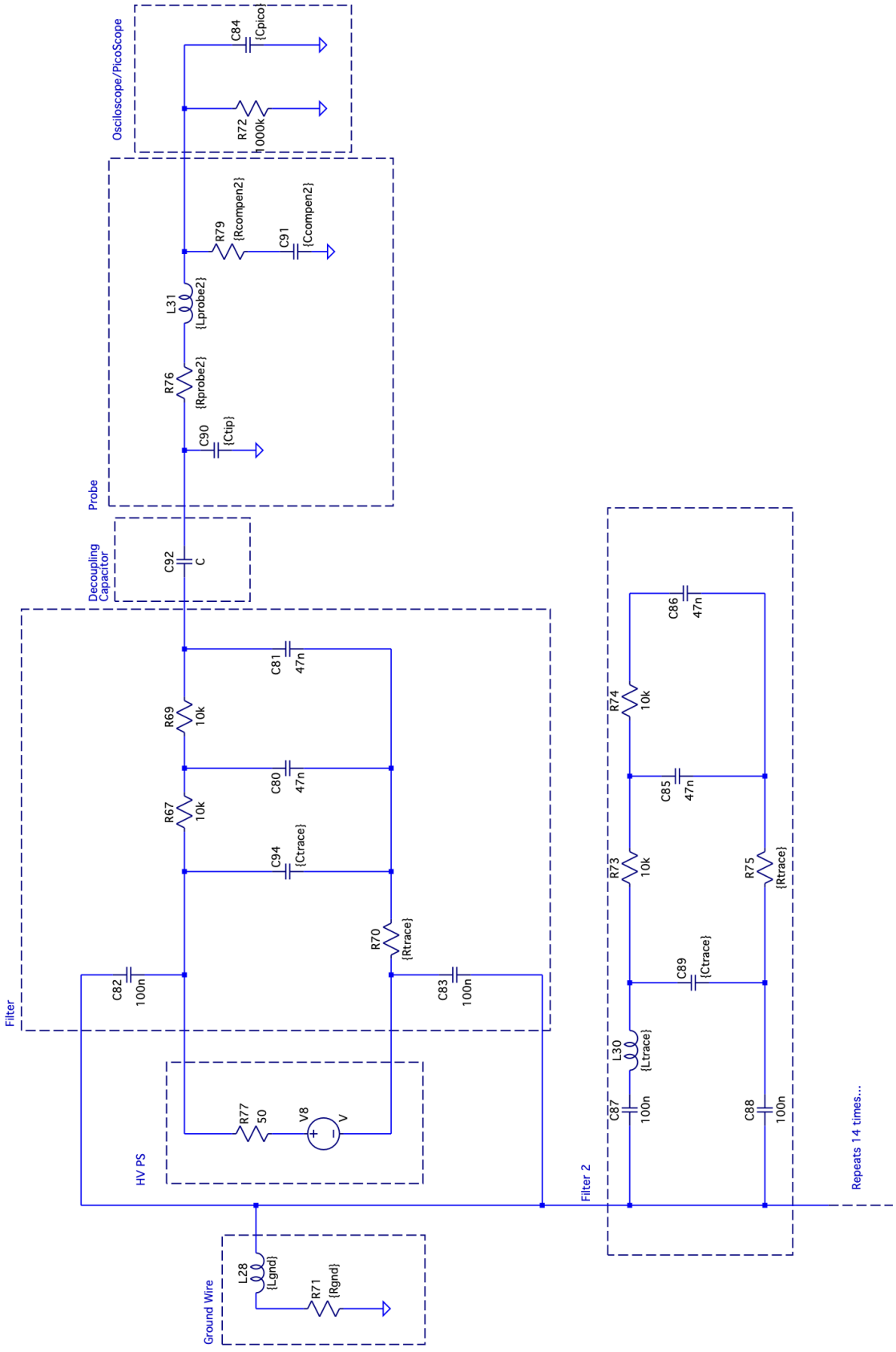

Figure 3.45: Full parasitic model of the ripple attenuation measuring schematic

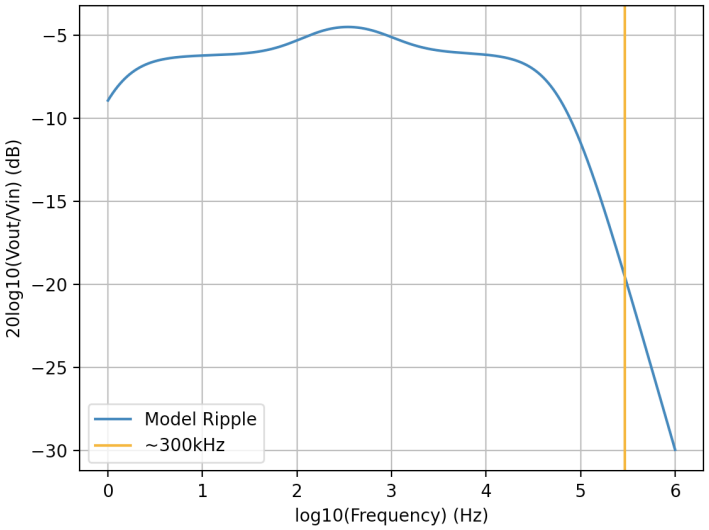

Figure 3.46: Model prediction of ripple attenuation, closely resembles the one measured (20 dB)

explanation for the observed ripple attenuation of about $-20\ dB$(Fig. 3.46). It's worth noting that in the HV scenario, we conducted tests by altering the values of series capacitance and inductance within the high-voltage power supply, with the aim of elucidating the observed phenomenon as changes in certain active components within the power supply. However, these adjustments resulted in no discernible changes in the plot.

3.11 Established model aplied to final environment

Understanding that the problematic high-frequency peaks are likely a consequence of probe parasitics is reassuring and brings clarity. However, it remains crucial to comprehend the filter's behavior in its intended operating environment. To gain a deeper insight into this aspect, a simulation was developed, as illustrated in the schematic presented in Figure 3.47.

The simulation comprises the board, including the previously determined parasitics. Additionally, it incorporates parasitics associated with the 100 m wire, 15 m connecting wires, and the connecting ground wire. Notably, the power supply in this simulation is set as floating. However, it's essential to highlight that the values assigned to the parasitics of the ground and connecting wires in this simulation are approximations. The primary aim here is to assess whether the high-frequency peaks are significantly mitigated and to identify any other noteworthy anomalies that might arise when varying the values of wire parasitics.

This simulation does not address a specific detail: in the final scenario, the high-voltage power supply (HV PS) will be referenced to ground by connecting it to the analog power ground of the PEB. This, in turn, is referenced to the experiment ground via the low-voltage power ground

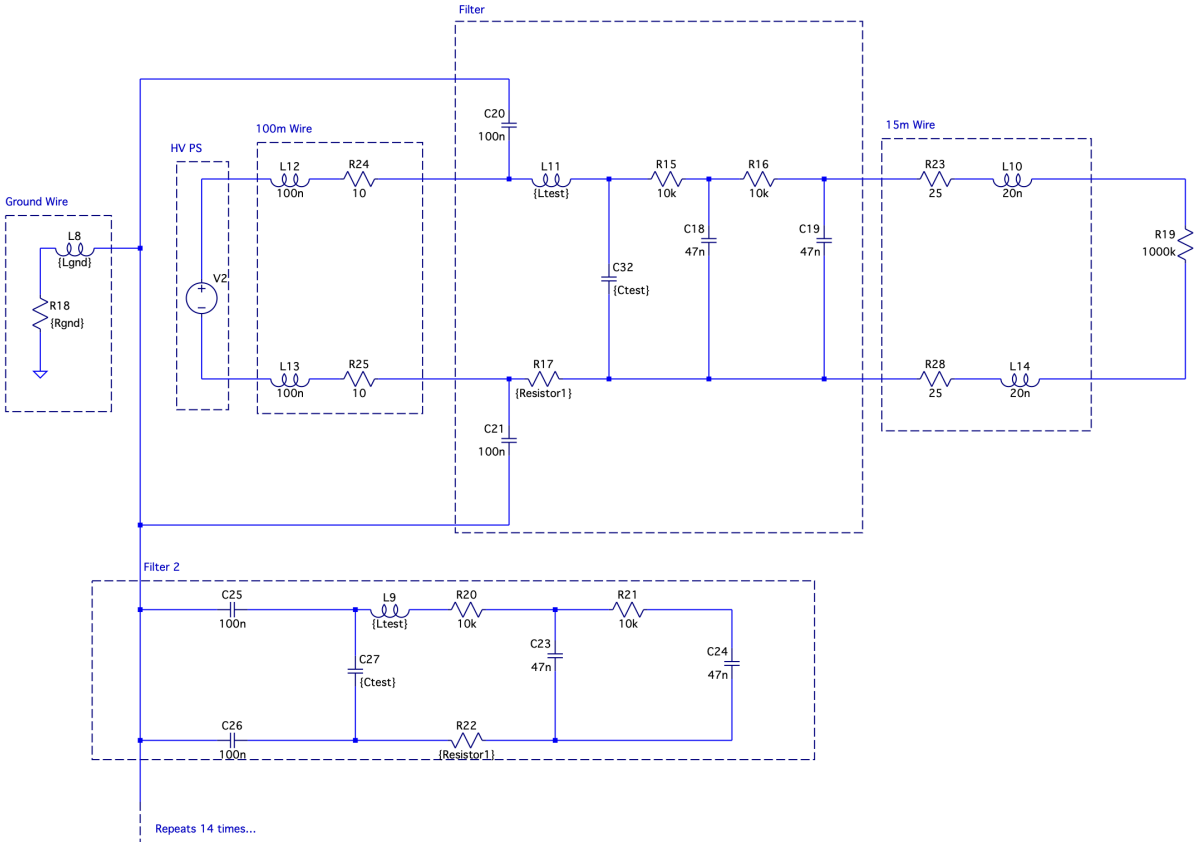

Figure 3.47: Full parasitic model of final envinronment

at the PEB, as explained in Section 2.2 and depicted in Figure 2.5. Notably, these grounds are quite distant from the ground to which the filters are connected, raising the possibility of variations between them.

This nuanced aspect is challenging to simulate, and a suitable approach to model it accurately as not yet been determined. Additionally, this complex system has its own parasitics and unique characteristics that need consideration. It's important to clarify that this simulation does not attempt to precisely predict the exact behavior of the filter. Rather, its purpose is to identify any glaring issues based on the findings related to the board's parasitics.

The obtained transfer curve, utilizing the parasitic values as outlined in the schematic, is presented in Figure 3.48, alongside the previous theoretical transfer curve that did not account for parasitic effects. An initial observation indicates the absence of peaks at higher frequencies in the transfer curve generated by this schematic. Upon comparing these two curves, it becomes evident that the filter's transfer function, within the context of the final environment schematic, exhibits a less steep response and initiates its decline at higher frequencies compared to the theoretical curve. The level of steepness depends on the magnitude of the parasitic effects within the wires, but it consistently results in a substantially less steep curve than the theoretical

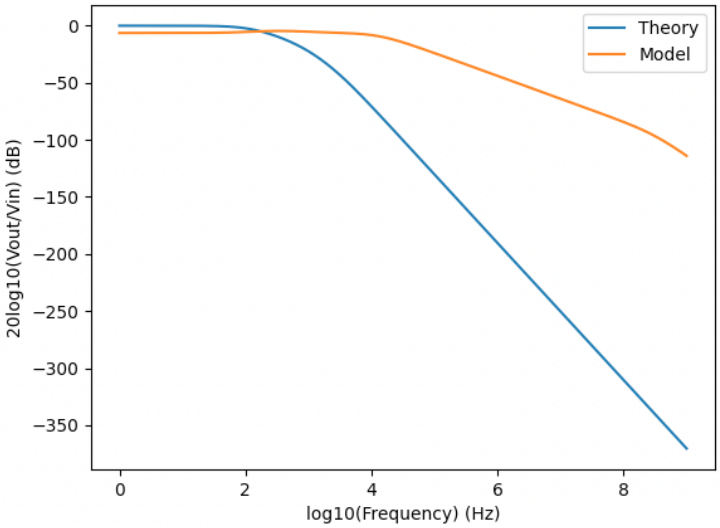

Figure 3.48: Simulation of the transfer curve for the model in the final environment compared to the ideal theoretical curve. In this simulation, the values of Lgnd and Rgnd were set at 10 $m\Omega$ and 50 nH, respectively.

counterpart. Importantly, this discrepancy in steepness does not necessarily invalidate the filter board as a noise attenuation solution. Conducting tests to evaluate signal propagation between channels under these conditions reveals minimal signal propagatian (-270dB). When examining the transfer curve, it appears that the inductance and resistance of the grounding wire have a relatively minor impact on it.

Turning our attention to the study of common mode noise in this scenario, a high-frequency peak manifests, primarily attributable to the inductance and resistance of the grounding wire. This significant reduction in common mode noise attenuation is an inherent characteristic but can predominantly be regulated through manipulation of the grounding wire's inductance and resistance. While complete elimination is unattainable, strategic adjustments can delay its onset as much as possible. Figures 3.49a and 3.49b illustrate how this phenomenon responds to alterations in these parameters. The key consideration here is to establish a threshold frequency beyond which attenuation is not critical and ensure that the decline in attenuation does not commence until that point.

In consideration of the possibility that the grounds are indeed identical, or at the very least, that any potential variances can be accurately modeled as inconsequential, a simulation was conducted with the power supply grounded.

In this scenario, keeping the parameters identical to the previous configuration, the transfer curve of a filter is depicted in Figure 3.50. It is notable that the observed curve is primarily influenced by the resistance values associated with the 100m and 15m wire connections. The

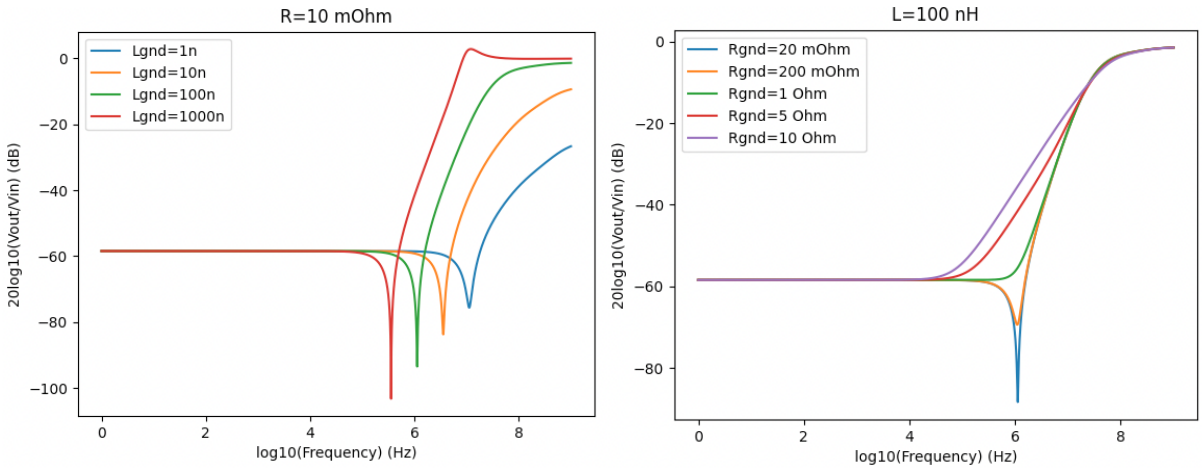

(a) (b)

Figure 3.49: Simulation of the transfer curve for the model in the final environment comparing the effect of grounding inductance (a) and grounding resistance (b)

filter's performance appears to improve as the resistance of the 100 m wire increases and as the resistance of the 15 m wire decreases.

Regarding the signal propagation through the board, the simulation results for the transfer curve of a channel that is adjacent to the one receiving the input signal, are displayed in Figure 3.51. The parameter values remain consistent with the previous configuration. Signal propagation, while more pronounced than in the previous scenario with a floating power supply, remains at a low level. The transfer curve appears to be primarily influenced by the inductance and resistance of the ground wire, with lower values of these parameters resulting in improved curve performance.

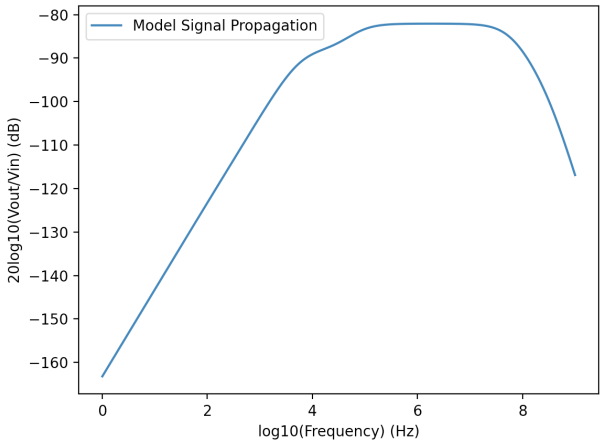

Figure 3.51: Simulation of the transfer curve of an adjacent channel for the model in the final environment with the PS grounded. In this simulation, the values of Lgnd and Rgnd remain at 10 $m\Omega$ and 50 nH, respectively.

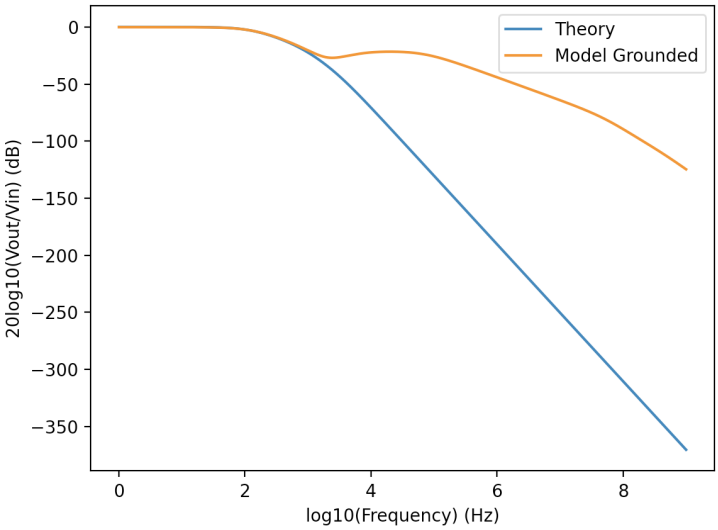

Figure 3.50: Simulation of the transfer curve for the model in the final environment compared to the ideal theoretical curve with the PS grounded. In this simulation, the values of Lgnd and Rgnd were set at 10 $m\Omega$ and 50 nH, respectively.

Lastly, when examining common mode noise in this scenario, a situation very similar to the one with the floating power supply arises. There is a decrease in attenuation at higher frequencies, primarily governed by the inductance and resistance of the ground connection.

It's worth noting that these results may differ as the final environment schematic continues to evolve, accommodating additional parasitic elements and addressing the intricacies related to ground reference details. Nevertheless, it appears reasonable to conclude that establishing a low-resistance, low-inductance connection to the ground would greatly benefit the performance of the filter boards.

4 Discussion and Conclusions

4.1 Discussion

The goal of this thesis was to evaluate and assess the performance of the filter, examining its behavior and integration within the HV system. It was hoped that through the filter characterization and comprehension of the filter's operation, a deeper understanding would be achieved, facilitating appropriate planning for the HV system. This would lead to insights into expected outcomes, areas for improvement, and potential modifications to be made.

To accomplish the research objectives, a series of tests were conducted to ascertain the filter's transfer function across various voltage levels. Surprisingly, the results indicated poor attenuation at higher frequencies, which was an unexpected finding. Furthermore, common mode noise attenuation was evaluated, revealing a similar unexpected outcome at higher frequencies.

A more detailed model of the testing schematic environment was developed to investigate this behavior observed at higher frequencies. The likely cause was attributed to the measuring equipment being employed in the experiments. It is worth noting that this issue is not expected to manifest in the final environment.

Additionally, cross-talk between channels was thoroughly examined. The analysis uncovered that the signal did not remain confined to its designated channel but instead propagated throughout the entire board via the ground plane. However, it was found that this might not be a problem in the final scenario, as demonstrated in simulations. Leakage current was another critical parameter subjected to testing, and it reached acceptable values following the cleaning and coating of the board.

The conclusion drawn is that the filter board functions adequately, although it may not perform as flawlessly as initially anticipated or predicted. However, it is also not as poor as initial test results might have initially suggested.

It has become evident that the actual performance of the filter within the final environment is subject to a more complex interplay of factors than initially anticipated. However, based on the outcomes of the simulation conducted for the final environment, it is reasonable to presume

that establishing a low-resistance, low-inductance connection to the ground would yield favorable results. Nevertheless, it remains crucial to delve deeper into the intricacies of integrating the filter into the high-voltage system to gain a more comprehensive understanding of its performance and to explore avenues for further optimization.

It is also worth noting that the code developed for the PicoScope could potentially serve as a foundation for automating filter testing in the future.

4.2 Limitations

The findings of this thesis are characterized by a degree of uncertainty, with some questions remaining unanswered and the conclusions lacking the robustness typically desired.

Regarding the shielding effect, while testing was conducted, the results did not yield conclusive evidence beyond the observation that the shield did not seem to significantly impact the filter within the specified frequency range.

Furthermore, the behavior of the HV transfer curve at lower frequencies (below 10kHz) remains unexplained, and its potential implications for the filter's performance in the final environment remain uncertain.

In the context of noise sources, the most anticipated source, ripple, appears to be attenuated by approximately -30 dB in the final environment simulation. However, this still leaves ripple at a level of around 6.3 mV, raising questions about its potential impact on the system's functionality.

The model, aimed at elucidating the obtained results and identifying the primary factors contributing to the high-frequency peaks, does not provide a perfect match with these peaks. While this alignment is not imperative for drawing the desired conclusions, coupled with the presence of certain questionable parameter values, it raises doubts about the model's overall validity and its suitability for extrapolation to the final environment.

Regarding the final environment, it's important to note that the current state of the schematic developed for it is still in its preliminary stages. One significant limitation of this simulation is that it assumes the power supply to be completely floating or completely grounded, whereas in reality, it will be referenced to the analog ground of the PEB. It's essential to consider that these ground references are likely to be slightly different, given their considerable separation. This specific detail is not addressed by the simulation but may have implications for the conclusions drawn from it.

4.3 Implications

This thesis does not really offer conclusive absolute values of filter performance but it does shine a light on some important aspects to keep in mind in order to maximize filter performance in the final environment namely the minimization of resistance and inductance of the ground connection to the filter board. However, it does provide a clear conclusion that the cleaning and coating of filter boards are essential steps for minimizing leakage current.

4.4 Future Work

Looking ahead to future work related to this thesis, as mentioned in the limitations section, it would be beneficial to improve the final environmental simulation. Additionally, as suggested in that section, setting up tests for the filter board's power supply and sensors could help determine if ripple attenuation is adequate. Moreover, considering the filter requirements, it's important to conduct tests regarding susceptibility to magnetic fields and resistance to radiation.

Bibliography

[1] J. Haffner, "The CERN accelerator complex. Complexe des accélérateurs du CERN," 2013. General Photo.

[2] The ATLAS Collaboration, "The atlas experiment at the cern large hadron collider," *Journal of Instrumentation*, vol. 3, p. S08003, aug 2008.

[3] A. Artamonov, D. Bailey, G. Belanger, M. Cadabeschi, T. Y. Chen, V. Epshteyn, P. Gorbounov, K. K. Joo, M. Khakzad, V. Khovanskiy, P. Krieger, P. Loch, J. Mayer, E. Neuheimer, F. G. Oakham, M. O'Neill, R. S. Orr, M. Qi, J. Rutherfoord, A. Savine, M. Schram, P. Shatalov, L. Shaver, M. Shupe, G. Stairs, V. Strickland, D. Tompkins, I. Tsukerman, and K. Vincent, "The atlas forward calorimeter," *Journal of Instrumentation*, vol. 3, p. P02010, feb 2008.

[4] The ATLAS Collaboration, "Technical Design Report for the ATLAS Inner Tracker Pixel Detector," tech. rep., CERN, Geneva, 2017.

[5] The ATLAS Collaboration, "Technical Design Report: A High-Granularity Timing Detector for the ATLAS Phase-II Upgrade," tech. rep., CERN, Geneva, 2020.

[6] Unpublished/Private Communication - Lei Fan and Ricardo Gonçalo and Bengt Lund-Jensen, "HGTD Eletronics: Specifications of the High Voltage System.".

[7] V. Bobillier, J. Christiansen, and R. Frei, "Grounding, Shielding and Power Distribution in LHCb," tech. rep., CERN, Geneva, 2004.

[8] Unpublished/Private Communication - Bengt Lund-Jensen and Ricardo Gonçalo, "HGTD High Voltage Status (PP).".

[9] Unpublished/Private Communication - Lei Fan and Ricardo Gonçalo and Bengt Lund-Jensen, "Specification of the High Voltage System.".

[10] Analog Devices, "Ltspice documentation."

[11] Tektronix, "Tektronix TDS3000B User Manual." https://download.tek.com/manual/071095704.pdf.

[12] TTI, "TTI TG5011 & TG2511." https://www.farnell.com/datasheets/1734336.pdf.

[13] M. Benedikt, P. Collier, V. Mertens, J. Poole, and K. Schindl, *LHC Design Report*. CERN Yellow Reports: Monographs, Geneva: CERN, 2004.

[14] The CMS Collaboration, *CMS Physics: Technical Design Report Volume 1: Detector Performance and Software*. Technical design report. CMS, Geneva: CERN, 2006.

[15] P. Cortese, *ALICE transition-radiation detector: Technical Design Report*. Technical design report. ALICE, Geneva: CERN, 2001.

[16] M. Capeans, G. Darbo, K. Einsweiller, M. Elsing, T. Flick, M. Garcia-Sciveres, C. Gemme, H. Pernegger, O. Rohne, and R. Vuillermet, "ATLAS Insertable B-Layer Technical Design Report," tech. rep., 2010.

[17] J. Jackson, "The atlas semiconductor tracker (sct)," *Nuclear Instruments and Methods in Physics Research Section A: Accelerators, Spectrometers, Detectors and Associated Equipment*, vol. 541, no. 1, pp. 89–95, 2005. Development and Application of Semiconductor Tracking Detectors.

[18] A. Vogel, "Atlas transition radiation tracker (trt): Straw tube gaseous detectors at high rates," *Nuclear Instruments and Methods in Physics Research Section A: Accelerators, Spectrometers, Detectors and Associated Equipment*, vol. 732, pp. 277–280, 2013. Vienna Conference on Instrumentation 2013.

[19] M. C. Aleksa, W. P. Cleland, Y. T. Enari, M. V. Fincke-Keeler, L. C. Hervas, F. B. Lanni, S. O. Majewski, C. V. Marino, and I. L. Wingerter-Seez, "ATLAS Liquid Argon Calorimeter Phase-I Upgrade: Technical Design Report," tech. rep., 2013. Final version presented to December 2013 LHCC.

[20] *ATLAS tile calorimeter: Technical Design Report*. Technical design report. ATLAS, Geneva: CERN, 1996.

[21] *ATLAS muon spectrometer: Technical Design Report*. Technical design report. ATLAS, Geneva: CERN, 1997.

[22] V. Izzo, "ATLAS Upgrades," tech. rep., CERN, Geneva, 2021.

[23] Unpublished/Private Communication - Sergei Malyukov, "HGTD Cables and Connectors SPR.".

[24] H. Williams, "ATLAS policy on grounding and power distribution," tech. rep., CERN, Geneva, 1999.

[25] Picotech, "Picoscope 2000 series Datasheet." https://www.picotech.com/download/datasheets/picoscope-2000-series-data-sheet-en.pdf.

[26] Picotech, "Picotech/picosdk-python-wrappers: A set of python bindings and examples for picoscope® oscilloscope and picolog® data logger products.." https://github.com/picotech/picosdk-python-wrappers.

[27] RigolTech, "MSO5000 Datasheet." https://beyondmeasure.rigoltech.com/acton/attachment/1579/f-0907/1/-/-/-/-/MSO5000_datasheet.pdf.

[28] Tektronix, "Model 2410 1100V sourcemeter." https://download.tek.com/manual/2410_902_01B.pdf.

[29] Kemet, "Surface mount multilayer ceramic chip capacitors." https://content.kemet.com/datasheets/KEM_C1076_X7R_HV_AUTO_SMD.pdf.

[30] Kemet, "C0805C153J5GACTU - kemet." https://connect.kemet.com:7667/gateway/IntelliData-ComponentDocumentation/1.0/download/specsheet/C0805C153J5GACTU.

[31] CAEN, "Technical Information Manual - CAEN471A." https://data2.manualslib.com/pdf7/230/22936/2293599-caen/n471a.pdf?1b9418a8eeaa8b99bea503eab67546a7.

Appendix A

Appendix

A.1 Transfer Curve 1

The transfer of the following filter schematic can be determined by Kirchhoff's Current Law that state that the sum of all currents flowing into a node equals the sum of currents flowing out of the node.

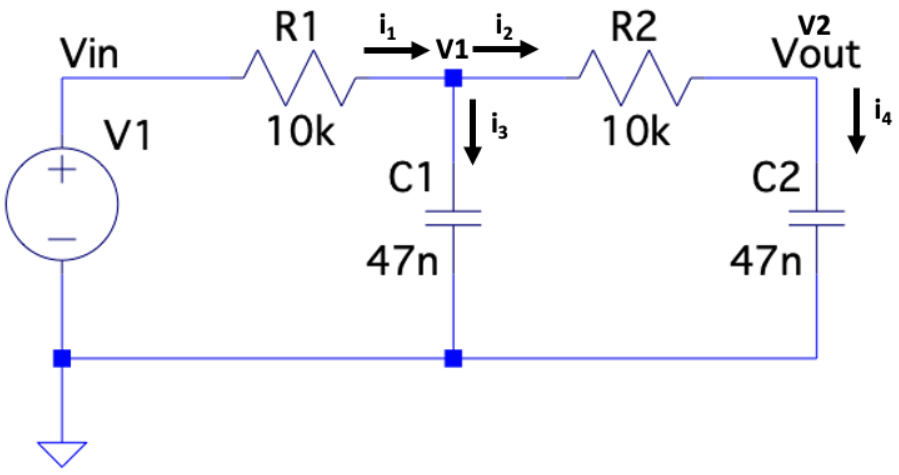

Figure A.1: Filter schematic

$$\begin{cases} i_1 = i_2 + i_3 \\ i_2 = i_4 \end{cases} \Rightarrow \begin{cases} \frac{V_1 - V_{in}}{R1} = \frac{V_{out} - V_1}{R2} + \frac{0 - V_1}{1/jwC_1} \\ \frac{Vout - V_1}{R2} = \frac{0 - Vout}{1/jwC_2} \end{cases} \Rightarrow \begin{cases} - \\ Vout - V_1 = -VoutjwC_2R_2 \end{cases}$$

$$\begin{cases} - \\ Vout + VoutjwC_2R_2 = V_1 \end{cases} \Rightarrow \begin{cases} - \\ V_{out}(1 + jwC_2R_2) = V_1 \end{cases} \Rightarrow$$

$$\begin{cases} \frac{V_{out}(1+jwC_2R_2)}{R1} - \frac{V_{in}}{R_1} = \frac{V_{out} - V_{out}(1+jwC_2R_2)}{R2} - \frac{V_{out}(1+jwC_2R_2)}{1/jwC_1} \\ - \end{cases} \Rightarrow$$

(considering only the top equation now)

$$-\frac{V_{in}}{R_1} = V_{out}(1 - 1 - jwC_2) - V_{out}(1 + jwC_2R_2)jwC_1 - \frac{V_{out}(1 + jwC_2R_2)}{R1} \Rightarrow$$

$$-\frac{V_{in}}{R_1} = -V_{out}jwC_2 - V_{out}(1 + jwC_2R_2)jwC_1 - \frac{V_{out}(1 + jwC_2R_2)}{R1} \Rightarrow$$

$$-\frac{V_{in}}{V_{out}} = -R_1jwC_2 - R_1(1 + jwC_2R_2)jwC_1 - (1 + jwC_2R_2) \Rightarrow$$

$$-\frac{V_{in}}{V_{out}} = -R_1jwC_2 - R_1jwC_1 - R_1j^2w^2C_2R_2C_1 - 1 - jwC_2R_2 \Rightarrow$$

$$\frac{V_{out}}{V_{in}} = \frac{1}{1 + R_1jwC_2 + R_1jwC_1 + jwC_2R_2 + R_1j^2w^2C_2R_2C_1} \Rightarrow$$

$$\frac{V_{out}}{V_{in}} = \frac{1}{1 + jw(C_2R_1 + C_1R_1 + C_2R_2) + j^2w^2R_1R_2C_1C_2}$$

Since the resistances and capacitances in this filter circuit the same we can consider $R_1 = R_2$ and $C1 = C2$ obtaining the following transfer curve equation:

$$\frac{V_{out}}{V_{in}} = \frac{1}{1 + jw3RC + j^2w^2R^2C^2} \tag{A.1}$$

A.2 Transfer Curve 2

The transfer of the following filter schematic can be determined by Kirchhoff's Current Law that state that the sum of all currents flowing into a node equals the sum of currents flowing out of the node.

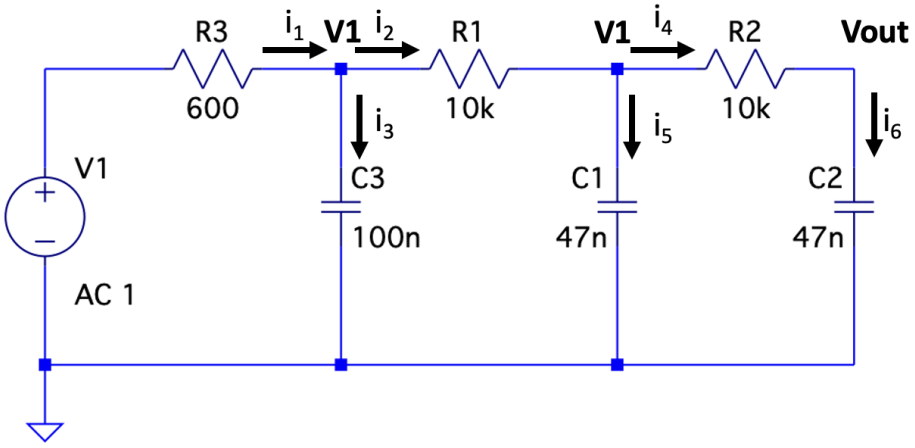

Figure A.2: Filter schematic

$$\begin{cases} i_1 = i_2 + i_3 \\ i_2 = i_4 + i_5 \Rightarrow ... \\ i_4 = i_6 \end{cases}$$

$$\Rightarrow \begin{cases} V_1 = V_{out}\left[(1 + jwC_2R_2)(1 + R_1jwC_1) + R_1jwC_2\right] \\ V_2 = V_{out}(1 + jwR_2C_2) \\ \frac{V_{out}}{V_{in}} = \frac{1}{R_3jwC_3[V_1] - \frac{R_3}{R_1}[V_2 - V_1] + V_1} \end{cases} \Rightarrow ...$$

$$\Rightarrow \frac{V_{out}}{V_{in}} = \Big(R_3JWC_3\left[(1 + jwC_2R_2)(1 + R_1jwC_1) + R_1jwC_2\right]... - \frac{R_3}{R_1}\left[(1 + jwR_2C_2) - \left[(1 + jwC_2R_2)(1 + R_1jwC_1) + R_1jwC_2\right]\right]... + \left[(1 + jwC_2R_2)(1 + R_1jwC_1) + R_1jwC_2\right]\Big)^{-1} \quad \text{(A.2)}$$

A.3 Low Voltage Transfer Curve for All Channels

The transfer curve of all the filters of the board were tested and compared using the PicoScope.

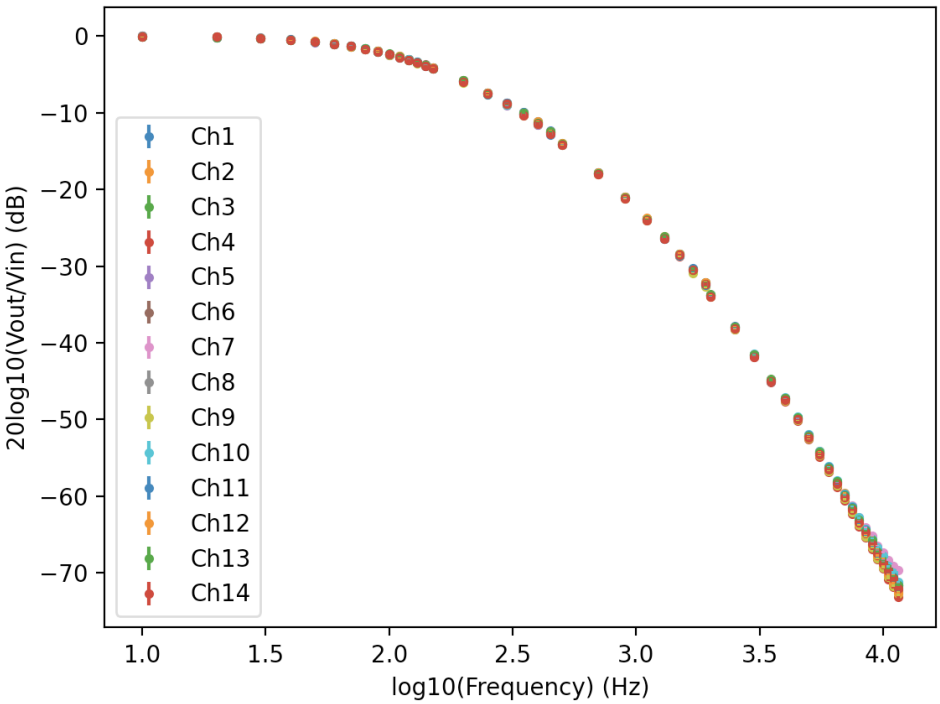

Figure A.3: Transfer function of the filter board's channels as determined through measurements employing a PicoScope

A.4 Ripple Attenuation

			Pkpk V (mV)	Attenuation (dB)				Pkpk V (mV)	Attenuation (dB)
Mod 1	Ch1	Before	160	-22,50	Mod 2	Ch1	Before	120	-23,52
		After	12				After	8	
	Ch2	Before	160	-22,50		Ch2	Before	160	-26,02
		After	12				After	8	
	Ch3	Before	190	-25,58		Ch3	Before	170	-24,61
		After	10				After	10	
	Ch4	Before	170	-13,73		Ch4	Before	120	-23,52
		After	35				After	8	
	Ch5	Before	170	-13,73		Ch5	Before	170	-26,55
		After	35				After	8	
	Ch6	Before	180	-14,22		Ch6	Before	140	-24,86
		After	35				After	8	
	Ch7	Before	180	-14,22		Ch7	Before	155	-25,74
		After	35				After	8	
	Ch8	Before	195	-14,92		Ch8	Before	150	-24,44
		After	35				After	9	
	Ch9	Before	175	-13,98		Ch9	Before	110	-22,77
		After	35				After	8	
	Ch10	Before	180	-14,22		Ch10	Before	140	-23,84
		After	35				After	9	
	Ch11	Before	180	-14,22		Ch11	Before	120	-15,56
		After	35				After	20	
	Ch12	Before	170	-13,73		Ch12	Before	130	-24,22
		After	35				After	8	
	Ch13	Before	170	-13,73		Ch13	Before	140	-23,84
		After	35				After	9	
	Ch14	Before	160	-13,20		Ch14	Before	135	-24,54
		After	35				After	8	

Table A.1: Full table of the outcomes derived from measuring the HV power supply output waveform both with and without the filter, displaying the attenuation levels.

Appendix B

Appendix

Filter board's PCB schematic


GND_in
C56
C52
C48
C44
C40
C36
C32
C54
C50
C46
C42
C38
C34
C30
Fgnd_in10
Fgnd_in6
Fgnd_in2
Fgnd_in11
Fgnd_in7
Fgnd_in3
Fgnd_in12
Fgnd_in8
Fgnd_in4
Fgnd_in13
Fgnd_in9
Fgnd_in5
Fgnd_in14
Fgnd_in1
In14
In10
In6
In2
In11
In7
In3
In12
In8
In4
In13
In9
In5
In1
C51
C35
C45
C29
R23
R7
R17
R1
C23
C7
C17
C1
R24
R8
R18
R2
C24
C8
C18
C2
C55
C39
C49
C33
R27
R11
R21
R5
C27
C11
C21
C5
R28
R12
R22
R6
C28
C12
C22
C6
C43
C53
C37
R15
R25
R9
C15
C25
C9
R16
R26
R10
C16
C26
C10
C47
C31
C41
R19
R3
R13
C19
C3
C13
R20
R4
R14
C20
C4
C14
Out12
Out8
Out4
Out13
Out9
Out5
Out1
Fgnd_out14
Out14
Out10
Out6
Out2
Out11
Out7
Out3
Fgnd_out12
Fgnd_out8
Fgnd_out4
Fgnd_out13
Fgnd_out9
Fgnd_out5
Fgnd_out1
Fgnd_out10
Fgnd_out6
Fgnd_out2
Fgnd_out11
Fgnd_out7
Fgnd_out3
GND_out